HELIUM ION IMPLANTATION IN ZIRCONIUM: BUBBLE FORMATION & GROWTH

A Dissertation

by

AARON ROBERT TOTEMEIER

Submitted to the Office of Graduate and Professional Studies of
Texas A&M University
in partial fulfillment of the requirements for the degree of

DOCTOR OF PHILOSOPHY

Chair of Committee,	Sean M. McDeavitt
Committee Members,	Lin Shao
	Hong Liang
	Karen Vierow
Head of Department,	Yassin Hassan

December 2015

Major Subject: Nuclear Engineering

ABSTRACT

To evaluate the behavior of inert helium gas bubbles in zirconium three variants of the metal were implanted with 140 keV helium ions to a total fluence of 3×10^{17} cm^{-2} and characterized in cross-section TEM in their as-implanted state as well as during annealing at different temperatures. The three zirconium alloys included high-purity crystal bar material, Zircaloy-4, and a powder-metallurgically extruded material with high carbon and oxygen concentrations.

At a sample depth consistent with a helium concentration of approximately 5 atomic percent, a change in the structure of the zirconium was observed a high density region of small (4nm diameter) bubbles formed at concentrations above 10 atom percent.

Initial bubble formation and growth was observed to occurred at a temperature between 400-450 °C and these initial bubbles had a unique planar geometry prior to migration and coalescence into more three-dimensional bubbles. These planar bubbles appear to be aligned with major axes parallel to the TEM specimen surface and their formation and growth is possibly due to an increase in the thermal vacancy flux within the zirconium.

The observations of bubble response to high temperature annealing suggest that in zirconium, as in other metals, maximum bubble size is weakly dependent on annealing time, whereas the bubble size distribution is strongly dependent on time. Specimens that underwent a prolonged room temperature aging developed a multimodal bubble size distribution within the high density region of small bubbles, concentrated near the highest helium concentration depth.

This work is dedicated to my family for their unending support. To my parents, Debbie and John, the hard work you both gave so that I could have this opportunity can never be properly repaid. To my wife Natasha, I could not have done this without your indefatigable encouragement and love. Thank you all.

In memory of John F. Totemeier.

ACKNOWLEDGMENTS

I would like to thank my committee for their support throughout the course of this research. Thanks to Julie Borgmeyer for her numerous efforts in support of this work, and the rest of the members of the Fuel Cycle & Materials Laboratory for their contributions. I would also like to thank Mike Martin & Michael Myers from the Ion Beam Laboratory for their assistance with ion implantation and teaching me the ways of TEM sample preparation by hand. I also thank Kinga Unocic, Dorothy Coffey, and the rest of the ORNL SHaRE team for their expertise and the use of their facilities to prepare and characterize the samples.

A special thank you to Sean McDeavitt for his support and guidance throughout this work and for allowing me the freedom to pursue my own questions.

TABLE OF CONTENTS

Page

LIST OF TABLES

LIST OF FIGURES

FIGURE Page

FIGURE Page

FIGURE Page

1. INTRODUCTION

This work is an experimental investigation of the formation and growth of helium gas bubbles in zirconium alloys. Although zirconium has been studied at length in scientific literature due to its prevalence in the field of nuclear energy, a question arose during a previous investigation [1] that could not be sufficiently answered by the existing knowledge. The goal of this work is to further understand the helium-zirconium system and characterize the behavior of inert gas bubbles as they form and evolve in the metal. The results obtained herein may be useful to the development of advanced nuclear fuels and waste forms that may utilize zirconium in applications beyond its current light water reactor experience.

The noted previous work investigated the fabrication and performance of a cermet form for the long-term storage of actinide elements following a hypothetical reprocessing scheme and the potential for direct re-burn in a fast reactor after storage [1, 2, 3, 4]. The cermet was to be formed with metallic zirconium and oxidized transuranic microspheres recovered from the reprocessing of used nuclear fuel. The goal of the cermet was to safely store the transuranic material for sufficient time such that a fast reactor economy could be utilized to recover fission energy from the transuranics, thereby reducing the long-term storage burden of civilian nuclear power and increasing carbon-free electricity generation.

A second design criteria of the cermet required its use as a final storage form for possible geologic disposal of the transuranics. This required the cermet to maintain its integrity (e.g. thermal conductivity) for potentially thousands of years. As many of the transuranic isotopes decay via α-particle emission, a non-trivial amount of helium gas will build up in the cermet depending on the amount of time the material was stored. Consideration of the behavior of this inert gas revealed a gap in the scientific literature which precluded the formation of an informed hypothesis. Development activities related to the cermet storage form have since been completed;

this work was carried at as a follow-on study in an effort to elucidate the behavior of this basic system.

Extensive investigations into the behavior of zirconium during irradiation were carried out in the 1970's and 1980's and a survey of the relevant literature is provided in Section 2. The emphasis of this work was to comprehend the behavior or zirconium and zirconium alloys in both nuclear fission and fusion systems as it has low neutron interaction cross sections and high corrosion resistance [5]. The low susceptibility of the metal to void formation contributes to its stability in a radiation environment [6,7]. It is this latter characteristic that is of interest here. As will be discussed further in Section 2, zirconium is resistant to the formation of irradiation-induced voids in a neutron field up to very high fluence as voids tend to collapse into dislocation loops. Significant efforts to understand this unique behavior led to the determination that the presence of inert gas atoms could stabilize the voids against this collapse and may be a requirement to forming voids in zirconium at lower fluence [8]. This discovery appears to have been made near the end of the research carried out on gas behavior in zirconium and little to no information was found in the subsequent literature that detailed further investigations of helium's behavior in zirconium.

This work comprises an investigation into the behavior of helium gas in zirconium metal. To that end, three different zirconium metals were implanted with a high dose of energetic helium ions at room temperature. The metals were observed in cross-section transmission electron microscopy (XTEM) in their as-implanted state as well as during *in situ* annealing. High purity crystal bar zirconium, powder-metallurgically extruded zirconium rods, and Zircaloy-4 were the materials chosen for this investigation, in an effort to identify differences in material composition on the behavior of helium-filled bubbles. The materials were ion-beam implanted with 140 keV He^+ ions to a maximum dose of $\sim$ 23 weight percent helium at a sample depth of $\sim$ 0.5 µm.

Section 2 of this document includes background information on inert gas behavior in metals, the formation and growth of gas bubbles and TEM characterization of bubbles in thin specimens. Section 3 identifies the zirconium metals evaluated in this work, as well as, provides a description of the ion beam implantation process and XTEM sample preparation methods used.

The results of the work performed are presented in Section 4 and include simulation of the ion implantation and calculations of TEM beam heating and damage during sample characterization. The XTEM characterizations for each of the three zirconium metals are presented for their as-implanted state, followed by the observations made during annealing. Due to equipment failure and time limitations, a systematic comparison across the three samples under the same annealing conditions was not possible.

A discussion of the major results is provided in Section 5. This includes the as-implanted bubble structure in the metals which took the form of high density region of small bubbles in the regions of highest helium concentration, a comparison of the onset temperature for bubble growth in the samples characterized, which occured between 400-450 °C. These initial bubbles appear to have formed due to an increase in thermal vacancy flux at the elevated temperatures as this method accounts for the location of the bubbles, their unique planar geometry and consistent alignment within the samples, though further confirmation of this mechanism is required. A discussion of the bubble response to high temperature annealing is provided, however much of the data that would allow confirmatory analysis of the dominant bubble growth mechanism in the high temperature regime was lost. Finally, the unexpected appearance of a multimodal bubble size distribution within the high density region of small bubbles in samples that were aged in the bulk at room temperature for an additional 9 months is noted.

Section 6 contains a final summary of the work and a list of suggested areas for future investigation that could expand on the results found here.

2. BACKGROUND

Zirconium is widely used in nuclear reactors because of its low neutron interaction cross section and high corrosion resistance. It is used as a cladding material in commercial light water reactor fuels and has been used as an additive to various metallic nuclear fuel designs used in research reactors. As such, a significant body of knowledge exists about the metal and its alloys behavior and properties and how they change during irradiation. Although experimental evidence has proven some of the initial theories incorrect, Northwood provides an early, detailed description of irradiation damage in zirconium [6].

Early investigations of radiation damage in zirconium suggested the relatively slow irradiation growth of the metal, compared to other pure metals, saturated at a fast neutron fluence of approximately 1×10^{25} m^{-2}. Part of the reason for the slower irradiation-induced growth observed in zirconium was a resistance to the formation of voids in the metal during irradiation [9, 6]. This result was inconsistent compared to many other pure metals which exhibit a more severe degree of irradiation-induced swelling at lower fluence, especially the *bcc* metals. It was determined that the observed growth saturation was a temporary plateau prior to the initiation of breakaway swelling at higher neutron fluence [10]. Although breakaway swelling does occur in zirconium, it happens at much higher neutron fluence than other metals considered for use in nuclear reactors. Numerous studies were performed on the growth and stabilization of voids in zirconium, encompassing neutron and electron irradiation, a variety of temperatures, impurity concentrations, cold-working, and microstructures [11, 12, 13, 14, 15, 16, 17]. The relevant result from these efforts is that void stabilization in zirconium requires the presence of an insoluble gas, such as helium. No recent investigations into the behavior of helium bubbles in zirconium have been found in the literature.

In general, metals with a cubic crystal structure exhibit similar responses to irradiation damage. However, this does not prove to be true as a general rule for hexagonal crystal structures. The type of damage and its impact on material behavior varies for each *hcp* metal and often has differing dependencies on microsctructure, temperature, and impurity composition [7]. Therefore, care must be taken when comparing the impact of radiation damage in zirconium to other hcp metals such as titanium and magnesium.

Table 2 below lists several of the basic zirconium material properties relevant to this work.

Table 2.1

Selected zirconium properties.

Crystal Structure	α-phase (hcp)	a = 0.32311 nm
		c = 0.51477 nm
		c/a = 1.5931
	β-phase (bcc)	a = 0.36090 nm
Atomic Weight		91.22
Density	α-phase (low Hf)	6.505 g/cm^3
	α-phase (high Hf)	6.574 g/cm^3
Temperatures	Melting Point, T_m	1852 $\pm$ 2 °C
	$\alpha \rightarrow \beta$, T_{tr}	862 $\pm$ 5 °C

2.1 Inert Gases in Metals

Inert gases inserted into metal crystals present a unique situation since they do not form compounds with the metal, unlike hydrogen or oxygen. Their presence can result in a significant degradation of material properties depending on the con-

centration of the gas atoms, where they reside in the matrix of metal atoms, and the property in question. Helium behavior in metals has been extensively studied, primarily related to their presence in fusion reactor materials, and a large body of knowledge exists in literature on various topics [18]. There is some inconsistency in the literature (especially in the early work) in the terminology applied to cavities in metals; some authors use *voids*, some use *cavities*, and others use *bubbles* when referring to the same structure. This document uses *cavity* as a general term to refer to an accumulation of more than one vacancy; *bubble* is used to refer to a cavity that contains gas atoms; and *void* is used to refer to cavities that do not contain gas atoms.

Inert gases may be introduced into metals either through nuclear reactions (e.g. [n,α] or α-decay for helium) or by ion implantation. Both of these processes are accompanied by some amount of atomic displacement damage to the metal. Smaller gas atoms such as helium and neon generally reside as interstitial atoms in the metal matrix, whereas heavier gases occupy substitutional sites creating a self-interstitial [19]. Investigations of inert gas behavior in metals generally fall into one of two categories: 1) cold-implantation followed by annealing or 2) hot-implantation. Variations of these two primary categories have been utilized depending on the phenomena being evaluated [20, 21]. Several thorough reviews exist describing the effects of inert gases in metals [18, 22, 23, 24]. Many analytical techniques have been utilized to study He behavior in a wide variety of conditions. As the work presented here involved room temperature ion implantation followed by annealing, the following review will focus on the formation and growth of helium bubbles under such conditions, similar to work performed in molybdenum [25, 26, 27].

2.1.1 Helium Atom Mobility

As inert gases do not form compounds with the atoms of the matrix the atoms remain readily available for migration. Helium generally has a low solubility in metals

and is capable of relatively fast interstitial diffusion even at low temperatures [28]. The atomic mobility is influenced by temperature, alloy composition, impurity concentration, and crystal defects. Of note, helium migration in zirconium is relatively rapid compared to many other metals, even at low temperatures [29]. This is likely due to the comparatively spacious *hcp* crystal structure of zirconium resulting in the metal being referred to as *open* due to its large c/a ratio.

2.1.2 Bubble Formation

Helium implantation for laboratory analysis is usually performed by either ion implantation or doping the material with a material that undergoes (n,α) reactions and subsequently irradiating the material with neutrons [24, 28]. Utilizing natural α emitters requires a significant amount of time to develop a sufficient concentration of helium and is generally performed as an integrated effects investigation, for example, irradiation in a fast reactor to simulate a fusion environment. The choice of implantation method depends largely on the type of analysis to be performed and the different radiation damage profiles caused by neutron irradiation or ion implantation must be considered. It is generally not accurate to directly compare studies wherein different implantation methods were utilized without correcting the results for the intrinsic differences in the implantation methods, such as the type of matrix damage introduced. Ion beam implantation of energetic helium atoms allows for more rigorous control over the experimental conditions compared to neutron irradiation of α-doped materials. Control of implanted helium energy allows for precise implantation depths, helium concentrations, and displacement damage creation.

Inert gas bubble nucleation can occur either via thermal or athermal processes, the latter usually becoming dominant at temperatures below about $0.3T_m$. At these lower temperatures bubble nuclei are formed via clustering of helium atoms through the mechanism of helium self-trapping [30, 31]. As these clusters become larger ($\sim$5-7 atoms) they are energetically capable of forming Frenkel-pairs in the metal

by self-interstitial ejection, a process energetically favorable to helium interstitial emission [32]. The energetics of the various processes involved in bubble nucleation are described in literature; Wolfer provides a detailed review of bubble nucleation and van Veen provides a review of the various interactions that can occur between helium atoms and matrix defects during the nucleation process [33, 34].

At higher temperatures, T $\sim$ $0.5T_m$, increased vacancy mobility in the metal allows the formation and subsequent clustering of helium-vacancy (HeV) complexes. Further vacancy absorption in these clusters maintains the internal pressure of the bubble nucleus below what is required for athermal processes to occur. Vacancy supply can be maintained either through equilibrium concentrations due to elevated temperatures, with free surfaces and grain boundaries providing a vacancy source, or as the result of freely migrating defects from radiation damage events. An excellent review of the two extremes of bubble nucleation, 1) high helium production at low temperatures; and 2) low helium production at high temperatures is provided by Trinkaus [35].

After stable bubble nuclei have formed they may grow via several processes. Inert gases tend to remain in bubbles rather than resolve into the matrix. The pressures in small inert gas bubbles can become so high that the gas forms a solid phase [36, 37]. A review of three inert gas bubble growth mechanisms follows.

2.1.3 Bubble Growth

The growth of a population of bubbles is referred to as bubble coarsening. Three mechanisms for bubble growth are discussed here, including migration and coalescence, Ostwald ripening, and dislocation loop punching.

Migration & Coalescence

The process of migration and coalescence occurs when two bubbles (at least one of them mobile) come into contact with one another, forming a larger single bubble. This process was first observed in helium bubbles in copper in 1963 by Barnes and Mazey [38]. Bubble migration in a chemical potential gradient occurs as matrix atoms at one edge of the bubble relocate to another position on the bubble edge. This may occur by surface diffusion along the bubble-matrix interface, volume diffusion in the matrix surrounding the bubble, or vapor transport through the the bubble. Figure 2.1 shows a schematic representation of these processes. The bubble diffusion coefficient, D_B, under isothermal conditions depends on the mechanism of transport by [39]:

$$D_B^{\text{surface}} = \frac{3a^4}{2\pi R^4\sqrt{2}} D_S \tag{2.1}$$

$$D_B^{\text{volume}} = \frac{\Omega}{R^3\pi} D_V \tag{2.2}$$

$$D_B^{\text{vapor}} = f(h,T)\frac{1}{R^2}\exp^{-h/kT} \tag{2.3}$$

where a is the lattice parameter, R is the bubble radius, D_S is the surface diffusion coefficient, D_V is the volume diffusion coefficient, Ω is the atomic volume of the matrix atoms, and $f(h,T)$ is a function of the latent heat of vaporization and temperature of the gas atoms. Surface diffusion is generally assumed to occur at lower temperatures, $< 1/3\ \ T_m$, and the other mechanisms become favorable above $1/2\ \ T_m$ [35].

Bubbles in metals are not always spherical and may form as platelets, or faceted structures depending on the matrix metal. Such bubbles may also diffuse via the mechanism of ledge nucleation, whereby a portion of the faceted face extends into the matrix, followed by the opposite face. A detailed treatment of bubble diffusion via ledge nucleation is provided by Goodhew and Tyler [40] and Kaletta [41].

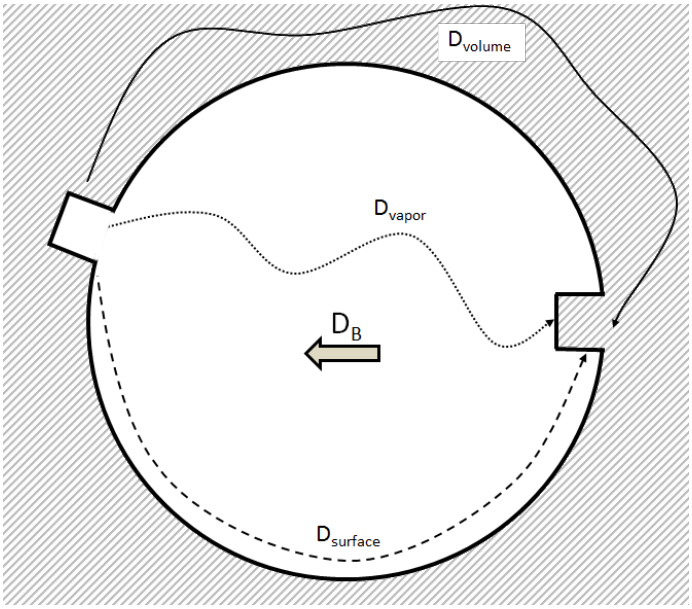

Fig. 2.1. Schematic representation of the matrix atom diffusion processes that can lead to bubble migration.

Many factors can influence the speed and direction of bubble migration within a material. The presence of chemical potential gradients such as gas atom concentration, temperature, pressure, and vacancy gradients within the matrix are typical driving factors for bubble motion. Bubble diffusion in a radiation environment has been shown to be as high as a factor of 10 greater for some metals [42].

Bubble coalescence occurs when two bubbles come into contact and combine. This can happen due to bubble migration or when stationary bubbles become large enough to contact one another. Coalescence can be described as a two-stage process: coalescence (Stage I) and volume adjustment (Stage II) [43]. Stage I is comparatively rapid and occurs predominately by surface diffusion, whereas Stage II relies on the slower volume diffusion process. For the remainder of this section, the term coalescence will be used to describe Stage I of the aforementioned processes; throughout

the remainder of the document coalescence is used in it's more general sense to refer to the combined process of bubble migration and coalescence.

To evaluate Stage I, several simplifying assumptions are made. First, it is assumed that two bubbles containing the same gas phase exist in a material with radii $r_1 < r_2$, and for simplicity it is assumed that the bubbles are at equilibrium and they are accurately defined by the ideal gas equation of state. Stage I is a volume conservative process such that $r_3^3 = r_2^3 + r_1^3$. The change in free energy during Stage I, ΔG_I, is defined by the free energy change of the gas, surface, and matrix strain of the system:

$$\Delta G_I = \Delta G^I_{gas} + \Delta G^I_{surface} + \Delta G^I_{strain} \tag{2.4}$$

Nichols provides a derivation of each of these terms for both stages of the coalescence process, the result of which is provided here [43]. Considering the coalescence stage, the free energy change of the gas, ΔG^I_{gas} is zero and the free energy change of the stage is dominated by the free energy change of the surface area, $\Delta G^I_{surface}$, as the strain energy change is less than 1% of the total energy change. For all such systems with a radius r_2 larger than $\approx 1{\times}10^{-8}$ cm, the coalescence process will occur, driven primarily by a reduction in bubble surface energy.

During the volume relaxation phase, Stage II, the coalesced bubble, r_3, undergoes volume adjustment to reach an equilibrium pressure, $p_4 = 2\gamma/r_4$. The matrix strain energy developed in Stage I is removed and the surface energy decrease from Stage I is regained, canceling each other out when comparing the total process. The gas in the bubble does work to increase the bubble volume such that the three energy terms are described as:

$$\Delta G^{II}_{surface} = -\Delta G^I_{surface} \tag{2.5}$$

$$\Delta G^{II}_{strain} = -\Delta G^I_{strain} \tag{2.6}$$

$$\Delta G^{II}_{gas} = -\int p_{gas} dV_{gas} = -(n_1 + n_2) kT \ln(V_4/V_3) \tag{2.7}$$

where n_1 and n_2 are the moles of gas in the initial two bubbles and V_3 and V_4 represent the coalesced bubble volume at the start and completion of the relaxation phase. From these definitions is is clear that the relaxation phase always results in a decrease in energy. The net change in free energy of the two stages is then equal to:

$$\Delta G_{total} = \Delta G_I + \Delta G_I I = \Delta G_{gas}^{II} < 0. \tag{2.8}$$

Therefore, two equilibrium bubbles in contact with one another will always combine into a bubble of radius $r_3 = (r_1^3 + r_2^3)^{1/3}$ and then increase in size to a final radius $r_4 = (r_1^2 + r_2^2)^{1/2}$. A summary representation of the coalescence process is provided in figure 2.2.

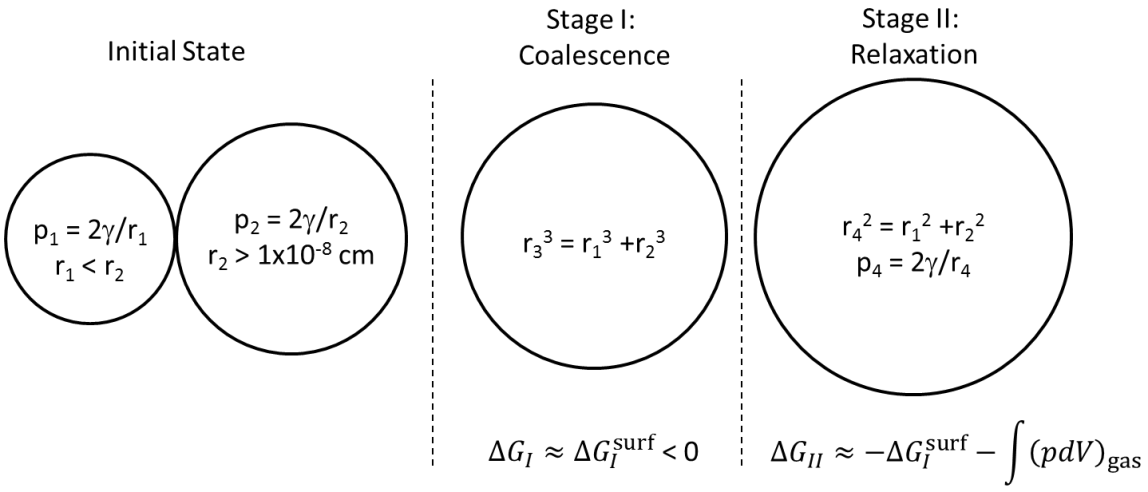

Fig. 2.2. Schematic representation of the coalescence and relaxation stages of bubble coalescence.

Ostwald Ripening

Ostwald ripening is the process wherein the interfacial energy of a two-phase mixture, composed of a dispersed phase and a continuous phase, undergoes a decrease

in interfacial energy by increasing the size of the dispersed phase. In terms relevant to the present work, gas bubbles in a metal matrix will grow in size via emission of gas atoms from small bubbles, atomic diffusion of the gas through the metal matrix, and eventually, absorption of the atom a larger bubble. The driving force for the ripening process can be described based on the curvature dependence of the chemical potential, μ, of an atom of the dispersed phase (bubble in this case) residing at the interface between the phases (bubble-metal interface here). Defining μ_0 as the chemical potential of a flat interface (i.e., no curvature), V_m as the molar volume of the atoms of the continuous phase (metal), γ as the interfacial surface energy, and κ as the mean curvature radius at the interface of the two phases, the curvature-corrected chemical potential can be written as [44]:

$$\mu = \mu_0 + V_m \gamma \kappa \tag{2.9}$$

From this equation it can be seen that a decrease in the chemical potential energy of the atoms of the dispersed phase occurs when the atoms reside at an interface with a lower curvature radius (i.e., a larger bubble). Figure 2.3 provides an illustration of the decrease in chemical potential that occurs during ripening due to a reduction in curvature radius. The reduction in curvature radius is a driving force for athermal bubble coarsening. However, its magnitude is relatively low compared to the chemical potential gradient of gas atom concentrations in bubbles at elevated temperatures, c_{He}. The process by which ripening occurs remains the same as shown in figure 2.3, however, it the chemical potential gradient would be represented by c_{He} instead of $\mu(r)$ for this situation.

The ripening process is highly dependent on the characteristics of the two phases and their state. It is also highly dependent on the local state of the individual bubbles. For example, a bubble near a grain boundary or vacancy source would be unlikely to acquire gas atoms from the matrix near those sources. Similarly, although an individual bubble may be large compared to the rest of the population, if it is

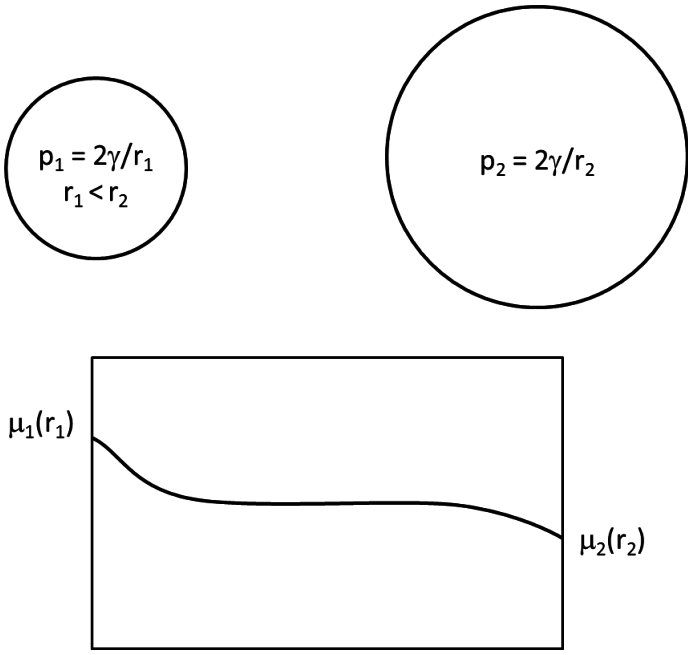

Fig. 2.3. Schematic illustration of the potential energy decrease from a gas atom moving from a bubble of small radius to a larger one.

near an even larger bubble, it may not receive a sufficient flux of incoming gas atoms to grow in size.

Diffusion is highly dependent on relatively (compared to atomic diameter) long-range forces determined by interactions between particles and atoms that may not be adjacent to one another. It is easy to see how matrix irregularities such as grain boundaries, point defects (such as impurities, vacancies and interstitials), and dislocation loops can interfere with the diffusion of gas atoms, inhibiting their re-absorption by larger bubbles. Consideration must also be given to the presence of free surfaces within the material as gas atoms near the free surface could be lost entirely from the system prior to being reabsorbed.

Loop Punching

At low temperatures, ($< 0.3T_M$), the thermal vacancy concentration in the metal may not be adequate for bubble growth. The athermal loop punching mechanism occurs when an over-pressurized bubble creates its own vacancies by ejecting a platelet of interstitial atoms, creating a dislocation loop. This mechanism was first suggested by Greenwood, Foreman, and Rimmer while analyzing fission gas bubble growth in uranium [45]. Evidence of this mechanism occurring in molybdenum has been confirmed [46], however some metals have not exhibited such growth under the conditions investigated [47]. For small bubbles the emission of a self-interstitial atom is energetically favorable. However, as bubbles increase in size, emission of a cluster of interstitials requires less energy, as the binding energy of the individual interstitials to the cluster is preserved [48]. An approximation of the pressure required for loop punching is given as [49, 50]:

$$P \geq \frac{\mu \bar{b}}{r} \tag{2.10}$$

where μ is the shear modulus and $\bar{b}$ is the Burger's vector of the dislocation loop.

2.1.4 Determination of Bubble Coarsening Mechanisms

Determination of the controlling coarsening mechanism, coalescence or ripening, has received a variety of theoretical treatments and experimental investigations. Historically, the approach has been to measure the mean bubble radius, $\overline{r}$, as a function of annealing time, t_a, and determine the value of n in equations 2.11 and 2.12 below. The rate of gas atoms arriving at a bubble surface varies for each mechanism [35] and subsequently the mean bubble radius as a function of annealing time can be described by [51]:

$$\overline{r} \propto (D_B c_{He} t_a)^{1/n} \qquad \text{(coalescence)} \tag{2.11}$$

$$\overline{r} \propto (D_{He} \hat{c}_{He} t_a)^{1/n} \qquad \text{(ripening)} \tag{2.12}$$

where D_B and D_{He} are the bubble and helium diffusion coefficients, respectively; c_{He} is the implanted helium concentration; and $\hat{c}_{He}$ is the concentration of helium dissolved in the matrix. A result of equations 2.11 and 2.12 is that coalescence depends on the helium dose whereas ripening does not. This leads to an interesting result in the analysis of experimental data used to determine the controlling mechanism.

If the mean bubble radius is plotted as a function of helium concentration for constant annealing times, t_a, the ripening process results in a constant bubble radius whereas coalescence results in an increasing radius. Conversely, if the mean radius is plotted as a function of the product of total helium and the annealing time, $c_{He} \cdot t_a$, coalescence results in constant bubble size while ripening results in a linearly decreasing bubble size. Schoeder et al. used the invariance of equations 2.11 and 2.12 to provide clarity in defining the conditions under which each mechanism is favorable [51]. Figure 2.4 provides a schematic representation of the invariance in bubble size for the two mechanisms. Plotting experimental data in this way can be used to identify whether coalescence, ripening, or both mechanisms are active.

For helium implanted austenitic steel it was found that for short annealing times (tens of hours) coalescence was dominant and ripening wasn't observed until much longer times (thousands of hours). With regard to helium concentration it was found that high helium implantation doses (above 20 appm) resulted in coarsening driven growth. Schroeder also found that plotting this data as $\overline{r}$ vs. t_a, as was historically performed, yielded inconclusive results in the value of n from equations 2.11 and 2.12.

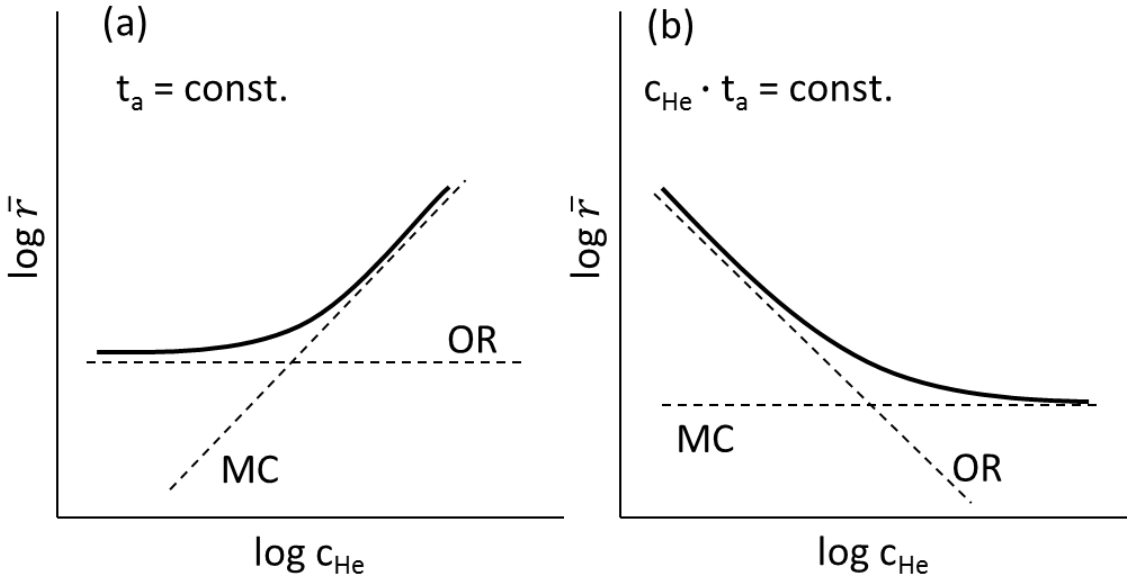

Fig. 2.4. Schematic representation of the invariance of the mean bubble radius, $\overline{r}$, for a) Ostwald ripening (OR) with constant t_a, and b) migration and coalescence (MC) with constant $c_{He} \cdot t_a$. Experimental data of mean bubble radius plotted in this way can identify which bubble growth mechanism is dominant.

2.1.5 Breakaway Bubble Growth

The mechanism of breakaway bubble growth has been suggested as a method for rapid gas loss from the bulk material and the formation of large pores on the surfaces of some post-implantation annealed metals [52]. Breakaway bubble growth is attributed to the rapid growth of a small number of bubbles to several orders of magnitude larger size than the average bubble population. Such large bubbles contain a significant portion of the implanted gas concentration and, if they become large enough to contact the specimen surface, can provide a rapid gas release pathway with some estimates of more than 80% of the gas concentration lost in this manner. The process occurs when high concentrations of inert gas are present in the material and swelling approaches 20%. Evans and van Veen have simulated the process and

shown that for 3% He concentrations the onset of breakaway growth can occur in as little as 50 seconds at 973 K in copper. Results for 2% and 1% increased to 400 and $3x10^4$ seconds, respectively, showing a rather significant impact on the speed of the phenomenon with gas concentration [53].

2.1.6 Helium Equation of State in Bubbles

It is common to assume the ideal gas law as the equation of state (EOS) for bubbles of a certain size, or to simplify theoretical treatments. However, the accuracy of ideal gas law diminishes as the bubble radius gets very small. Significant effort has gone into developing and testing various equations of state for helium and other inert gases [54, 55, 56]. In general, they take the basic form of the ideal gas law and introduce a *compressibility factor*, z. The two extremes of the stability of a spherical inert gas bubble arise from assuming either the mechanical stability limit of the matrix or the thermodynamic equlibrium of the gas. The mechanical stability limit represents the pressure in the bubble above which the matrix material would yield, where μ is the shear modulus of the matrix [49]:

$$p \leq 0.2\mu \tag{2.13}$$

while the condition for thermodynamic equilibrium is defined, for a spherical bubble, by the well-known equation:

$$p = 2\gamma/r \tag{2.14}$$

For this work, the Brearly and MacInnes hard-sphere equation of state (H-S EOS) is used due its excellent agreement with measurements [54]. Glam et. al. measured He atom density in bubbles in aluminum using electron energy loss spectroscopy (EELS) and found excellent aggreement between the EELS measurements of 5 nm

radius He bubbles and the predicted atom density from the H-S EOS [57]. The H-S EOS takes the following form:

$$\frac{PV}{NkT} = z = (1 + y + y^2)(1 - y)^{-3} \tag{2.15}$$

where P and V are the bubble pressure and volume, respectively; N is the gas atom density; k is Boltzman's constant; T is temperature; and z is the compressibility factor which is derived as a function of the bubble geometry factor, y, defined as:

$$y = \frac{\pi d^3 N}{6V} \tag{2.16}$$

where N is the number of gas atoms in the bubble.

2.2 Gas Bubble Ordering

Inert gas implantation into the basic bcc, fcc, and hcp structures have all shown the formation of a spatially-ordered bubble lattice, commonly ordered parallel to the close-packed plane. Such ordering is referred to as a bubble lattice and it can exist with either two- or three-dimensional (a so-called super-lattice) ordering within the material [58]. In two-dimensionally ordered lattices the bubbles align in parallel planes with a measurable lattice spacing parameter, a_l, but have no apparent order within the individual planes, unlike their three-dimensional counterpart. For bcc and fcc metals, the bubble lattices have been found after high-energy helium implantation, with helium doses above approximately 10 appm with implantation temperatures above 0.2 T_m. The bubbles in the lattice have a diameter in the range of 1 to 3 nm and typical lattice spacings are in the range of 6 to 8 nm [58]. The lattice spacing appears be negligibly influenced by the temperature of implantation above a threshold temperature, which for molybdenum has been found to be approximately 0.15 T_m [59]. Similarly, there appears to be a helium dose threshold below which a

lattice does not form and there is no evidence of an influence of the shear modulus of the matrix.

Bubbles within the superlattice are highly faceted and irregular in shape, although bright field TEM makes these features difficult to discern. The gas inside the bubbles is over-pressurized but the attainable pressure is limited by the host matrix shear modulus. Bubble concentrations within the lattice are calculated from the lattice spacing parameters for 3D lattices and, for 2D lattices, an assumption that the intraplanar bubble spacing is equivalent to the interplanar lattice spacing parameter can be made. Bubble concentrations in the cubic metals have been calculated as high as 3.6×10^{25} m^{-3} for vanadium [60], but are typically on the order of, or less than, 1×10^{25} m^{-3} [58].

Upon annealing, the bubble superlattice generally maintains a constant bubble size and spacing up to $\sim 0.4\ T_m$. Heating to higher temperatures results in a rapid process of bubble growth [61]. The bubble size in the annealed superlattice generally varies with larger bubbles forming near the middle of the lattice region, and smaller, more ordered bubbles near the edges [62].

The hcp metals observed to date have only shown evidence of two-dimensional bubble lattices, parallel to the basal plane of the metal with no apparent ordering within the individual planes. Mazey and Evans [37, 63] evaluated titanium samples implanted at room temperature with Kr and observed the formation of both a bubble superlattice and solid Kr precipitates. The two-dimensional superlattice was ordered in the basal plane of the Ti matrix and randomly ordered within the planes. The lattice parameter was observed to be 5.4-5.8 nm with a bubble concentration of 6.5×10^{24} m^{-3}. Helium implanted titanium samples were found to have a slightly increased lattice spacing of 6.5 nm. The solid Kr precipitates had an epitaxial hcp structure. The presence of solid phase bubbles appears to be common for the heavier inert gases, independent of the type of gas or host metal crystal structure. The bubble superlattice takes the form of the matrix lattice and solid precipitates, if

they exist, share the crystal structure of the host matrix [64, 27, 65]. Evidence of Kr bubble ordering in zirconium implanted at temperatures up to 400 °Chas been observed [66].

The formation of the bubble superlattice is thought to occur due to anisotropic, two-dimensional self-interstitial atom diffusion along close-packed planes. This theory is based on the evolution of void ordering observed in highly irradiated materials wherein initially randomly-oriented voids being to align parallel to the close-packed planes [65]. Cavities within the matrix align parallel to the plane of self-interstitial atom diffusion [66], which, for hcp structures, is the basal plane.

2.3 Zirconium Inert Gas Observations

Void formation during irradiation in metals is a well-known phenomenon. Voids form as irradiation-induced vacancies accumulate and form three-dimensional vacancy clusters. Zirconium has proven resistant to void formation up to very high electron and neutron fluence and the vacancy complexes tend to form two-dimensional loops rather than voids [67]. The formation of stable cavities in Zr requires a concentration of inert gas atoms to stabilize the collapse of vacancy structures [68, 9].

Pagano et al. investigated Kr bubble formation in Zr via ion implantation [69,70]. Their work evaluated thin film specimens which were implanted *in situ* in a TEM and bulk specimens which were implanted and then prepared for TEM, irradiated in the temperature range of 300-800 °C. The specimens were implanted with 100 keV Kr ions up to 2×10^{20} m^{-2}. Using the Transport Range of Ions in Matter (TRIM) code [71] to simulate ion range and damage distribution, with a zirconium atom displacement energy, E_d, of 25 eV, the peak Kr concentration corresponded to 9 at% and the peak damage was 45 dpa. The results of the implantation showed little difference in the bubble distribution in thinned and bulk specimens implanted at 300 °C. At higher temperatures much larger bubbles were observed in the bulk samples. This is attributed to mobile bubbles escaping from the free surface of

thinned samples in the TEM. Large, faceted bubbles were formed by coalescence at temperatures above 700 °C. The authors investigated several Zr alloys and found no difference in the bubble behavior between them. The authors comment that although this result is unexpected it may attributable to the use of thin specimens, wherein the effect of the high surface area to volume ratio overpowers the effect of alloying constituents [69].

2.4 TEM Imaging of Small Features & Bubbles

Viewing bubbles and other crystal defects in TEM is not a straightforward process. Depending on the nature of the defect, its size, and whether or not a strain field exists around it, the feature may not be visible as a contrast variation in a focused image. In general, this is more applicable to small features. Viewing small bubbles in TEM requires the use of out-of-focus imaging techniques wherein the image plane is some distance, ζ_i, from the exit plane of the sample. Rühle provides a detailed treatise on the phenomenon and provides an analytical discussion of the effect of imaging bubbles in the out-of-focus condition [72].

Figure 2.5 is a schematic representation of out-of-focus imaging in TEM, recreated from Rühle's description. To summarize, out-of-focus imaging causes contrast differences between the crystal structure of the sample and the cavity. The contrast may be either negative (darker) or positive (lighter) depending on the sample, defect type, and electron beam condition. The direction of the change in distance between the imaging plane and the sample exit surface, ζ_i, is generally referred to as *overfocus* ($\zeta_i > 0$) and *underfocus* ($\zeta_i < 0$). In the overfocus condition small bubble interiors appear darker and their perimeter is is bright. The opposite is true for the underfocus condition, (i.e. light bubble interior with a dark perimeter). These contrast differences are due to Fresnel fringes (diffractions in the electron beam wave) that develop due the interface between the bubble and the atomic structure of the

material. Larger bubbles always appear bright in the interior region as the Fresnel fringes become dominant near the bubble perimeter [72].

This phenomenon is important when imaging bubbles as the apparent size of the bubble viewed in the TEM can differ significantly from the true diameter. For bubbles with a diameter of 5 nm this difference can be ∼50%, increasing quickly as bubble size decreases. Larger bubbles are less affected and generally the radius of the imaged bubble is within 20% of the real bubble radius.

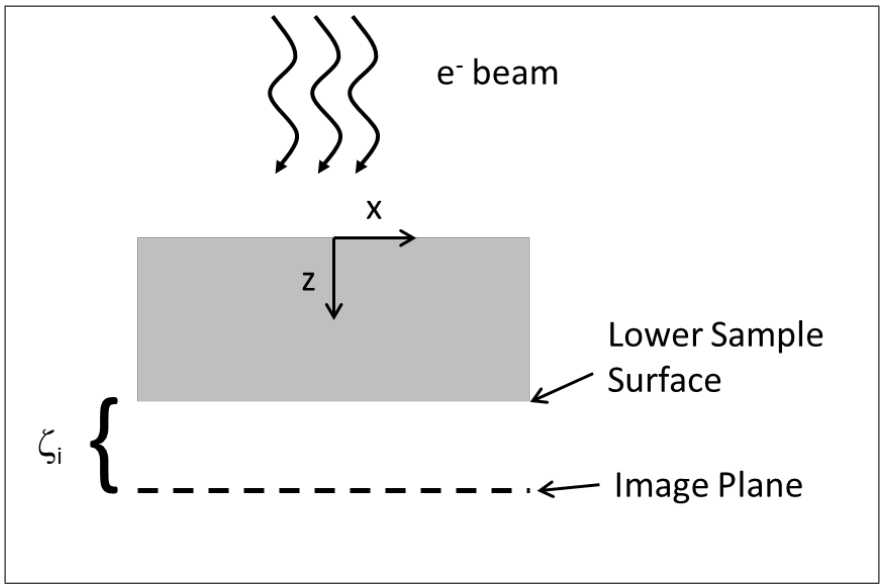

Fig. 2.5. Schematic of out-of-focus imaging in TEM.

2.4.1 Thin Sample Analysis

Another consideration for TEM investigations is the very thin sample thickness. In order to be transparent to electrons, metal specimens are thinned to approximately 100-150 nm. This results in an increase in surface area to volume ratio in the thinned region which can impact the source and sink strength for point defects in the sample. This has two main implications for the work described in this document,

i.e., annealing of thinned TEM samples implanted with insoluble gas, as the free surface acts as a source of vacancies which migrate into the specimen bulk. These vacancies can contribute to the growth of over-pressurized bubbles in the sample through a process termed spontaneous vacancy condensation [73]. This can lead to a form of bubble coarsening whereby individual bubbles grow and coalesce without the migration of nearby bubbles, though random walk processes still apply. Chernikov et al. evaluated the formation of helium bubbles in thin and bulk specimens of nickel and observed enhanced bubble coarsening for thinned specimens though the authors concluded that Ostwald ripening was the dominant coarsening mechanism, occurring after sufficient vacancies had been absorbed by over-pressurized bubbles to enable that mechanism, bubble growth by vacancy absorption was not considered an option in their work [74].

Bubble migration can also be impacted by vacancy gradient in the thin TEM sample as bubble motion up the concentration gradient occurs during vacancy absorption. This phenomenon was first confirmed in cross-section TEM investigations of He implanted nickel [75, 76, 77]. Although some investigators argued that a vacancy gradient alone was not enough to cause bubble motion, gas release models that simulate this phenomenon accurately simulate experimental observations of bubble morphology, swelling, and gas release [78, 79, 80].

The velocity of a bubble, relative to the specimen surface, in a vacancy concentration gradient is given by [77]:

$$V_b = -2D_v \frac{dC_v}{dx} \tag{2.17}$$

where, D_v is the vacancy diffusivity, C_v is the vacancy concentration, and x is the distance from the surface. The vacancy concentration gradient can be determined by C_{sv}/x where C_{sv} is the vacancy concentration at the surface [78].

At high temperatures, helium bubble shrinkage has been observed in TEM-thinned gold samples [66]. This phenomenon was attributed to helium resolution

into the matrix and subsequent capture by thermal-equilibrium vacancies. A significant population of bubbles underwent a reduction in size and even disappeared. Although the temperatures under which this was observed (0.9 T_m) are much higher than the temperatures used in this work, the high helium mobility in zirconium could lead to a loss of any resolved gas atoms, potentially at a lower temperature than observed for gold.

3. EXPERIMENTAL

To instigate bubble formation and growth in zirconium, three different zirconium metals were implanted with 140 keVHe^+ ions at room temperature to a fluence of 3×10^{17} cm^{-2}. Implanted specimens were prepared for cross-section transmission electron microscopy (XTEM) to observe bubble characteristics and morphology as a function of implantation depth. Several XTEM preparation methods were evaluated including mechanical polishing and focused ion beam (FIB) milling. Samples were implanted at room temperature and heated *in situ* in the TEM.

The following discussions provide details on the zirconium used in this study (3.1), the ion implantation equipment and procedures (section 3.2), and the methods used to prepare samples for XTEM (section 3.3).

3.1 Zirconium Metals Evaluated

The three zirconium materials chosen for this analysis were high-purity crystal bar zirconium (labeled: XTAL), Zircaloy-4 (labeled: Zr-4), and extruded zirconium formed from powdered metal (labeled: HX). The extruded material was formed via powder-metallurgical hot extrusion at ~750 °C as part of earlier work [1]. Table 3.1 presents the impurity concentration for each of the metals measured by inductively coupled plasma mass spectrometry (ICP-MS). The Zircaloy and crystal bar material were legacy products and their origin and fabrication methods are not documented. The Ni content in the Zircaloy confirms it is Zircaloy-4, as the typical range of Ni in Zircaloy-2 is 0.03 - 0.08 w/o. The hot extruded material began as -325 mesh powder, purchased from Wah Chang®, that was stored as purchased from the supplier. The high oxygen and nitrogen content of the material suggest that the powdered metal may have oxidized during storage or brief exposure to atmosphere. it may have been exposed to atmospheric air. This could be due to prolonged exposure to room temperature air during storage or high temperature air during the hot extrusion

process used for fabrication, the powders were stored in an inert atmosphere glovebox during handling and preparation of the extrusion samples [1].

The three materials were chosen based on their compositional differences such that any differences in the helium bubble characteristics and/or behavior between them could be identified. The high purity crystal bar material is a common choice, the Zircaloy-4 alloy is a standard alloy used in the nuclear power industry, and the extruded material was chosen for its high oxygen concentration.

Table 3.1
Impurity concentrations of the zirconium materials investigated; ppm by weight.

Material	Label	C	Cr	Fe	Hf	N	Ni	O	Sn
Zircaloy-4	Zr4	60	1150	2140	67	25	<35	720	15700
Extruded	HX	300	<50	135	175	770	<35	3500	<25
Crystal bar	XTAL	20	<50	<50	165	<20	<35	60	<25

3.2 Ion Implantation

Sections of the bulk material were segmented from each specimen using a Leco VC-50 diamond saw to nominal dimensions of 2 x 10 x 5 mm. A Buehler Minimet-1000 sample polisher was used to mechanically polish all samples prior to implantation. To ensure the faces of the sample were parallel, a planing jig was fashioned and the samples were ground with 600-grit SiC paper. Subsequently, the face to be implanted was polished with a final polish of 9 µm diamond paste. Samples were prepared to this stage and stored until the implantation. Within one hour prior to being mounted on the ion implanter stage, each sample was polished with 3 µm and 1 µm diamond paste for 15-20 minutes to remove the oxide layer as oxygen trapping of helium atoms has been observed in zirconium [81]. After this final polish, samples

were cleaned with ethanol and rinsed with deionized water. Further contact with any source of hydrocarbons was avoided.

Implantation was performed at the Ion Beam Laboratory (IBL) of Texas A&M University in the Nuclear Engineering Department in December 2009. The room temperature implantations were performed utilizing a 140 keV He^+ beam. The total fluence for each implanted sample was 3×10^{17} cm^{-2} and generally took 6-8 hours to complete. After the implantation, the samples were prepared for TEM observation.

3.3 Sample Preparation for TEM

Preparing a sample to examine a specific depth can be difficult using conventional planar TEM methods, wherein a single depth region is prepared for observation and material above and below that region is destroyed. Comparing different implantation depths using planar TEM would require multiple sample preparations and significantly increase the observation time. Cross-section TEM (XTEM) was chosen as it allows for comparatively easy evaluation of the sample depth profile. Sample preparation for XTEM can be more challenging than for conventional planar TEM and several mechanical polishing methods were evaluated during the course of this work. Although electropolishing has been proven effective with Zr alloys it generally requires the use of hydrofluoric or perchloric acids which were unavailable for this work. As such, mechanical thinning, polishing and dimpling was used to prepare the specimens for ion milling.

The *split-tube* technique used here (shown schematically in figure 3.1) involves placing the sample on its edge such that, after thinning, the "depth" of the implanted layer is radially outward from the center of the TEM specimen. The Zr samples were fitted into a slot at the end of a copper rod such that the implanted face was near the diameter of the rod. The rod-sample was then loaded into a 3 mm OD copper tube and the assembly was epoxied together. After curing, wafers of the sample were

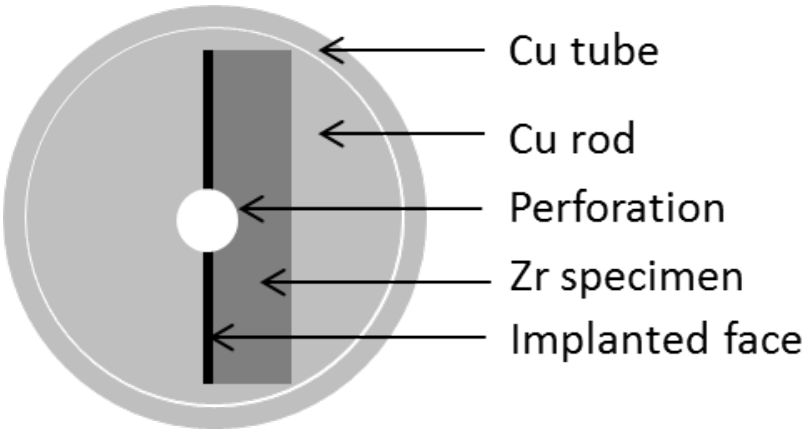

Fig. 3.1. Schematic representation of the split-tube technique for preparing TEM samples in cross-section. The implanted sample is fitted to a slot in the end of a solid rod such that the implanted face is on the diameter. The assembly is epoxied into a hollow tube for support and sectioned.

cut with a diamond saw and the copper tube formed the sample grid and holder for thinning and ion milling. This method produced very fragile samples which were often destroyed during dimple grinding. It was determined that the difference in hardness between the Zr and Cu led to preferential removal of the copper prior to thinning the Zr during polishing. Replacing the copper with a metal of similar hardness to Zr could have resolved this issue, however custom fabrication of the necessary materials was not available and this method was abandoned.

The second method developed for sample preparation involved sectioning the implanted sample into two pieces and adhering the implanted faces together (see schematic in figure 3.2). The sample was thinned with mechanical polishing to a thickness of $\sim$ 70 µm and mounted to a molybdenum TEM sample grid for ion milling. The adhesive used in this work was M-Bond-610®, a two component epoxy-phenolic resin insoluble in acetone. After adhering the sample faces together they were placed in a small vice and cured in an oven for no less than 24 hours and

allowed to cool in the oven. After curing, the samples were mechanically polished and mounted to a TEM grid.

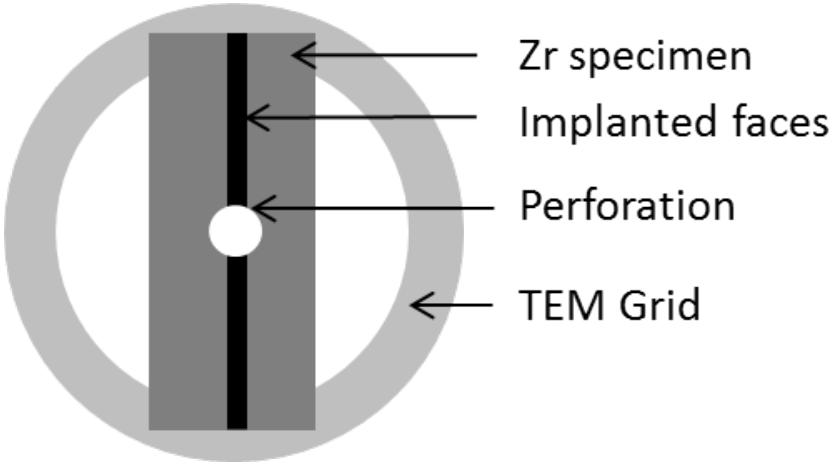

Fig. 3.2. Schematic representation of face-to-face sample preparation technique.

3.3.1 Mechanical Polishing

Final thinning and polishing of the specimens required precision and patience as removing too much material at one time, or uneven polishing resulted in destruction of the sample. The goal for this stage of sample preparation was to achieve a specimen with parallel faces, one polished to ∼1 µm and the other mechanically dimpled to yield a thickness of ∼15 µm. The required precision is unobtainable with general purpose sample polishing equipment as a difference in thickness of >1 µm across the 3 mm specimen would lead to poor image quality in the TEM. A Gatan Model 623 Disc Grinder was used for initial planing of the top and bottom surfaces and controlling the thickness of the specimen.

The specimens were mounted with Crystalbond to a Pyrex specimen mount designed to fit the sample preparation equipment. One edge of the specimen was planed

with a disc grinder with 400 or 600 grit SiC paper. The specimen was remounted, plane side down, and thinned. This thinning rate was performed with 600 grit SiC paper in 10-20 µm increments. The thinning rate was reduced as the sample became thinner, such that no more than 10 µm of material were removed after the sample was approximately 150 µm thick. When the specimen was 60-80 µm thick it was transferred to the dimple grinder. The specimen was dimpled with 6 µm diamond paste until the thickness at the bottom of the dimple was about 15 µm. Final polishing of the surface of the dimple was performed with 1 µm diamond paste. The specimen was then cleaned with acetone and rinsed with deionized water prior to mounting on a molybdenum TEM grid with M-bond-610®.

3.3.2 Ion Milling

Ion milling was performed at the Microscopy and Imaging Center (MIC) at Texas A&M University. Zirconium is highly susceptible to hydriding in the presence of hydrocarbons [82] and the formation of hydrides caused thinned samples to warp, destroying the samples. The ion milling chamber had to be baked out for > 15 hours prior to milling to minimize hydrocarbon contamination each time the ion milling was performed. Even with this step, several specimens were destroyed or severely warped during milling. It is possible that small amounts of hydrocarbon contamination from the diffusion pump oil were leaking into the sample chamber but no solution for this possibility was available. The initial milling step was performed for two hours and subsequent steps were performed as needed to perforate the specimen, typically the total active ion milling time was between 5 and 8 hours. The settings used for milling and polishing in the ion mill are shown in table 3.2.

Significant effort went into developing a successful, repeatable sample preparation technique. However, an administrative change at the MIC prohibited epoxied specimens from being used in their TEM at elevated temperatures. At this point

Table 3.2
Standard settings used in the ion mill for Zr specimens.

Parameter	Milling	Polishing
Top Gun Voltage (V)	5.5	3.5
Top Gun Current (mA)	5.0	3.5
Top Gun Angle (°)	12	3.0
Bottom Gun Voltage (V)	5.5	3.5
Bottom Gun Current (mA)	5.0	3.5
Bottom Gun Angle (°)	3.5	3.0
Stage rocking †	45	360

† From interface orthogonal.

the SHaRE facility at Oak Ridge National Laboratory (ORNL) was contacted and sample preparation and TEM imaging was performed at that facility.

3.3.3 Focused Ion Beam

The SHaRE facility is equipped with a Hitachi NB5000 focused ion beam (FIB) - scanning electron microscope (SEM). The FIB uses a 40 kV Ga ion beam to carve a TEM sample out of the bulk implanted sample. Sample preparation with the FIB is a multi-step process wherein the TEM sample is removed from the bulk implanted sample and attached to a grid. Figure 3.3 shows the primary steps in the process. First, carbon and tungsten are layered on top of the region of the bulk sample from where the TEM specimen will be taken. This coating protects the specimen below from Ga ion damage as the Ga beam is used both for imaging and cutting. Material is removed from the region of interest, leaving a small wafer of the sample that is attached to the tip of a needle via tungsten cold-welding. The needle is used to lift

the sample out of the bulk material and position it on a grid where the sample is thinned with the gallium cutting beam.

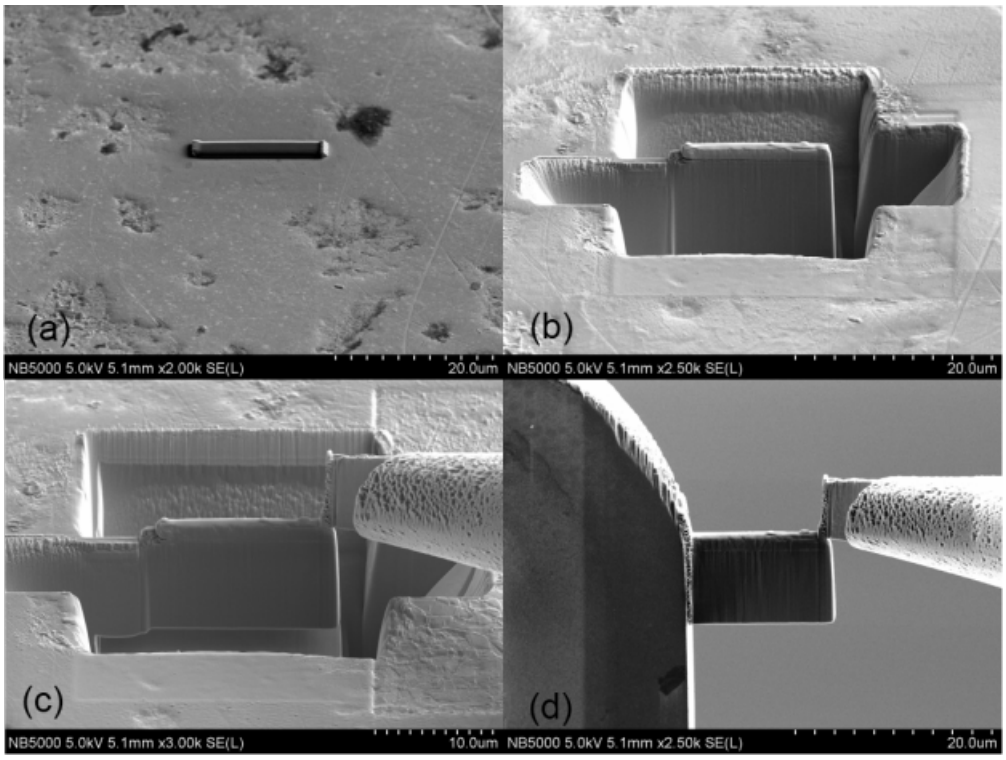

Fig. 3.3. Coating of C and W over the region of interest [a]; troughs carved out around the TEM specimen [b]; needle attached to the specimen before liftout [c]; specimen is attached to a grid with W for final thinning [d].

After mounting to the sample grid the Ga ion beam was used to thin the sample for TEM observation and the specimen was attached to an Aduro®heating chip with tungsten. Several thinning profiles were tested over the course of the work and it was determined a sample with a increased thickness along the bottom, left, and right edges provided increased strength and reduced the occurrence of sample distortion after mounting to the heating chip. Figure 3.4 shows a specimen undergoing the thinning process and one mounted to a heating chip with tungsten. After mounting

to the heating chip the samples were cleaned in an argon plasma to remove any Ga contamination from the surface. This cleaning process varied for each sample depending on the level of gallium present.

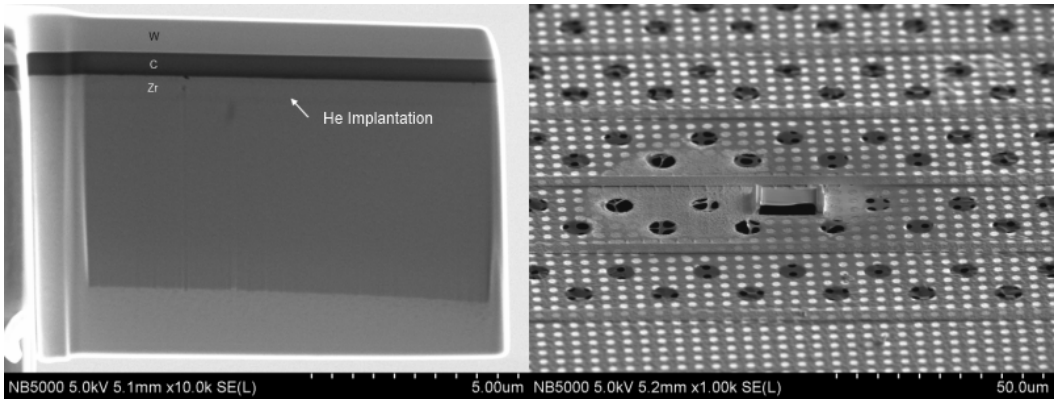

Fig. 3.4. Zircaloy-4 specimen during FIB thinning. Shows the protective W and C layer and the region of He implantation at the top 0.5 µm of the Zr. Image on the right shows a sample mounted to a heating chip.

Multiple methods of mounting the sample to the heating chip were tested. Early samples were bonded on the left and right side of the sample, as shown in Figure 3.4. This caused a large amount of strain in the sample upon heating as the sample tended to bow due to thermal strain, distorting the image. Subsequent samples were bonded on one side and across the bottom in an attempt to reduce strain. Figure 3.5 is a schematic representation of this mounting method. Severe straining and deformation upon heating was not observed in samples mounted in this way.

Sample preparation with the FIB was significantly faster than the mechanical polishing methods. A typical sample prepared via mechanical polishing and ion milling required roughly 50 hours of time including epoxy curing and ion mill bakeout. With the FIB process this time was reduced to around five hours for the final preparation techniques used.

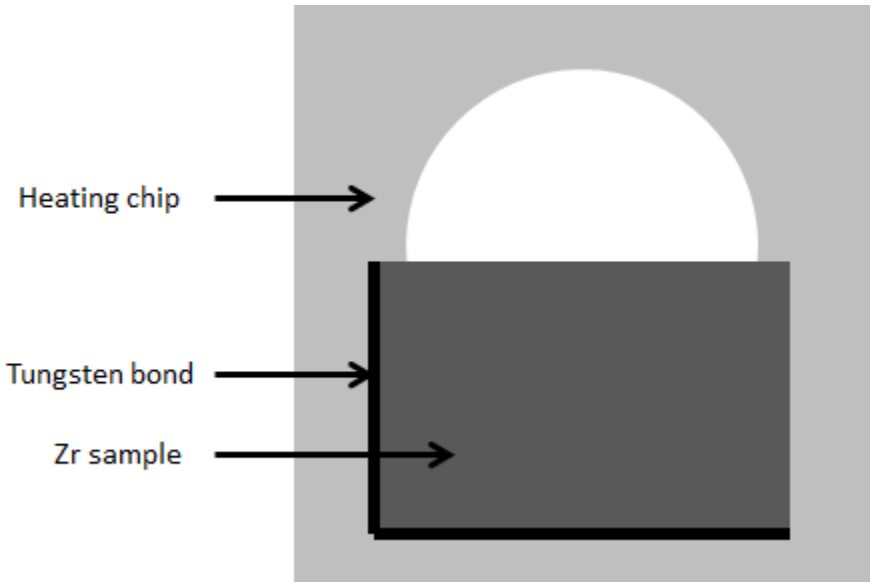

Fig. 3.5. Schematic representation of sample bonded to heating chip on two sides.

4. RESULTS

Prior to the characterization of helium-implanted zirconium samples in the TEM, ion implantation was simulated to determine the helium distribution and zirconium atom displacement. Calculation of the displacements per atom and the effect of electron beam heating and damage production were also performed.

4.1 Calculations

4.1.1 Simulation of He Ions in Zirconium

Simulation of the He^+ ion beam interaction with zirconium was performed with the Stopping and Range of Ions in Matter (SRIM) code package (version SRIM-2011) [71]. Transport Range of Ions in Matter (TRIM), a sub-code to SRIM-2011, was used to simulate 140 keV He^+ ions incident on a zirconium target. The SRIM-2008 stopping power version was used for ion energy loss calculations with full damage cascades to calculate He^+ distribution and zirconium atomic displacement during the implantation. The TRIM code incorporates several assumptions to simplify calculations, such as: target layers are considered to be amorphous (i.e., no crystallinity effects are simulated), interactions between particles are treated as binary events and ignore the influence of neighboring particles. Also, the method used to account for particle locations can lead to minor variances depending on the thickness of the simulated target layer and near layer interfaces. That said, the SRIM code package is a remarkably efficient tool and is widely used for simulations of ion stopping in matter. The damage production model follows the Kinchin & Pease method [83].

As an aside, recent developments in molecular dynamics research suggest the Kinchin & Pease method may not be accurate for calculating the number of freely migrating defects that exist after atomic collisions [84]. The work presented here

utilized the Kinchen & Pease damage model to allow for comparison with related research.

Figure 4.1 shows the results of the TRIM simulation as a function of sample depth. Displacements per atom as a function of depth, dpa(z), were calculated from the TRIM output with equation 4.1.

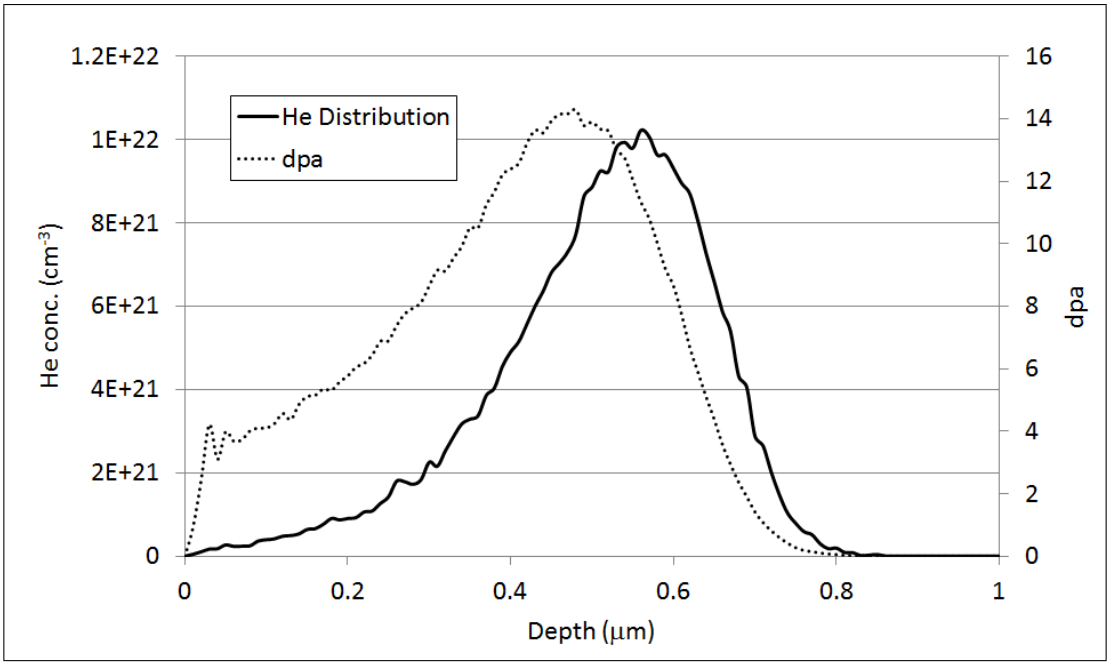

Fig. 4.1. Helium ion distribution and dpa profile after 140 keV implantation in Zr, TRIM output.

The TRIM results shown in figure 4.1 show the peak helium dose of $\sim 1 \times 10^{22}$ cm^{-3} occurs at a depth of approximately 0.55 µm. The peak atomic displacement of $\sim$14 dpa occurs slightly closer to the sample surface at a depth of 0.45 µm.

$$\mathrm{dpa}(z) = N_{\mathrm{displ}}(z) \cdot N_I / N_0 \tag{4.1}$$

where:

N_{displ} = displacements per incident ion per unit length

N_I = ion fluence

N_0 = target material atom density

4.1.2 Electron Beam Heating

Electron beam interactions with materials can lead to material heating under certain conditions. To ascertain whether electron beam heating might occur in this work, evaluation of TEM sample heating was performed. Using the method described by Jenčič, the temperature rise, ΔT due to electron beam interactions for a circular TEM specimen with a perforated hole is calculated by:

$$\Delta T = \frac{I}{\pi \kappa e} \left| \frac{dE}{dx} \right| \ln \frac{b}{r_o} \tag{4.2}$$

where I is the cylindrical electron beam current, κ is the thermal conductivity of the sample, e is the electron charge, $\dfrac{dE}{dx}$ is the electron energy loss in the sample, and b and r are the radius of the sample and the electron beam, respectively. Electron energy loss is calculated following the method employed by Newbury [85]:

$$\frac{dE}{dx} = -7.85 \times 10^4 \frac{Z\rho}{AE} \ln \left(\frac{1.166 \cdot E}{J} \right) \qquad \left[\frac{\text{keV}}{\text{cm}} \right] \tag{4.3}$$

where

$$J = (9.76Z + 58.5Z^{-0.19}) \times 10^{-3} \qquad [\text{keV}] \tag{4.4}$$

Equation 4.2 predicts a temperature rise of approximately one degree for cylindrical, perforated TEM specimens, confirming that electron beam heating has a negligible contribution to TEM sample temperature during the annealing observations as the majority of the annealing work was performed at $T_a > 400\,^{\circ}\text{C}$. This calculation was not repeated for the rectangular samples prepared by FIB as their

larger size would result in a lower temperature rise than calculated with this method, allowing this calculation to provide a bounding estimate of beam heating.

Beam heating during the FIB processing is assumed to have a similarly negligible impact as the gallium beam energy is deposited at a glancing angle to the sample into material that is ablated from the sample.

In summary, this calculation indicates the beam heating of the implanted samples during both sample preparation and observation is negligible for the present work.

4.1.3 Electron Beam Induced Damage

Another consequence of using electron microscopy for this type of work is the creation of atomic displacements by the high energy electrons. A common method of investigating the influence of atomic displacement rate in helium implanted metals is to use a high energy electron beam for TEM imaging, such that the electron beam creates a known damage rate to the specimen and its impact can be observed in real-time [8].

This section evaluates whether or not electron beam interactions with the samples in the TEM would be expected to create additional atomic displacements (dpa) while observing the samples. The Monte Carlo-Assisted Classical Method (MCCM) presented by Piñera [86], yields the number of displaced atoms per electron, N^e_{dpa}, as follows:

$$N^e_{dpa} = \int_{E_c}^{E} N_A \sigma_{dpa}(E') \left(\frac{-1}{\frac{dE}{dx}} \right) dE' \tag{4.5}$$

Equation 4.3 can be used for the electron energy loss, $\frac{dE}{dx}$, and the displacement interaction cross section is:

$$\sigma_{dpa} = \sigma_{PKA}(E) \cdot \nu(T) \tag{4.6}$$

where $\sigma_{PKA}(E)$ is the primary knock-on atom interaction cross section and $\nu(T)$ is the damage function.

This analysis was quite simple for the TEM conditions used in this work as the lower bound in the integral of equation 4.5 is the electron cut-off energy, or the electron energy necessary to displace an atom of the material:

$$E_c = \sqrt{(mc^2)^2 + \frac{Mc^2 \cdot E_d}{2}} - mc^2 \tag{4.7}$$

Assuming 40 eV for the displacement energy, E_d, in α-zirconium [87,88], equation 4.7 gives a minimum electron energy of $\sim$ 889 keV, well above the 300 keV in the TEM used for this work.

For simplicity, the displacement damage cross-section, σ_{dpa}, is calculated assuming the target atoms are static (i.e., no atomic vibration) which results in a value of zero up to some threshold energy and a linear increase at that threshold until reaching a plateau at some higher energy. Recent investigations into electron-beam damage in single-layer graphene made by Meyer et al. demonstrate the consequence of this static lattice assumption [89]. The experimental results of Meyer et al. show carbon atoms being displaced by electron beams with energy as low as 80 keV compared to the generally accepted value of 108 keV for single-layer graphene. This discrepancy has been attributed to the atomic vibration of the primary knock-on atoms. When the atom's vibratory motion is along the path of the incident electron velocity, an electron with energy below the static lattice displacement cross-section threshold may cause displacement. Accounting for atomic vibrations in the calculation of σ_{dpa} results in a smoothing of the function near the threshold energy as the vibration of the primary knock-on atom is not a discrete function. Meyer et al. note the significance of this result to investigations of single-layer graphene and other nano-materials and suggest that consideration of atomic vibration may lead to more accurate displacement cross-sections for other materials as well. While this phenomenon likely does impact σ_{dpa} for bulk materials, the magnitude of the change

in σ_{dpa} reported by Meyer is quite small and its impact is largest within $\sim 25\%$ of the static lattice threshold beam energy. As the beam energy increases beyond this threshold, the contribution of atomic vibrations to σ_{dpa} becomes negligible. A reduction of 25% in the electron beam threshold energy calculated by equation 4.7 would result in a non-zero σ_{dpa} occurring at an electron beam energy of ~ 665 keV, a factor of two higher than the beam energy used in the work presented here.

In summary, atomic displacements of the zirconium matrix are not expected to occur due to electron beam interactions in the work presented here.

4.2 Evaluation of He-Implanted Zirconium Metals

In order to further understand the mechanisms of He bubble formation and growth in zirconium, the zirconium materials described in section 3.1 were irradiated with 140 keV He^+ ions to a fluence of 3 $\times 10^{17}$ cm^{-2} at room temperature. The implanted specimens were observed at room temperature to characterize the as-implanted bubble morphology and subsequently heated *in situ* at various temperatures to observe bubble behavior.

The observations were performed during two separate visits to the SHaRE facility. The trips were separated by 10 months and the implanted materials were stored at room temperature during this time. The samples presented herein are numbered as 1 and 2 with respect to the first and second observation period. Each sample was evaluated at room temperature to determine the as-implanted structure prior to heating the samples to investigate changes with temperature.

All bubble size measurements presented here were made with the open source digital image analysis software Fiji [90]. Image thresholding and automated image segmentation routines available in the Fiji code suite were unable to reliably distinguish individual bubbles in the images. As such, bubble identification was performed manually by identifying individual bubbles as discrete regions of interest for analysis from the digital images captured during TEM observation.

Throughout this document the terms *top* and *bottom*, when referring to implanted specimens, are used to refer to the region of the sample nearest to and further away from the implanted surface, respectively.

Table 4.1 below shows a summary of the observations made during this work, including the specimen name, the diameter of any bubbles identified in the as-implanted condition at room temperature (RT), the maximum annealing temperature for the specimen, and the mean bubble diameter at the maximum annealing temperature.

Table 4.1
Summary of characterization conditions presented.

Specimen	Report Section	$\overline{d_B}$ at RT	Max Annealing Temp. (T_a^{max})	$\overline{d_B}$ at T_a^{max}
XTAL-1	4.3.1	1 nm †	450 °C	20-30 nm
XTAL-2	4.3.3	-	560 °C	-
HX-1	4.4.1	4 nm	450 °C	-
HX-2	4.4.3	5 nm, 17 nm ‡	700 °C	10-40 nm ±
ZR4-1	4.5.1	-	450 °C	21 nm
ZR4-2	4.5.3	4 nm, 10-20 nm ‡	800 °C	50 - 100 nm ±

† Small population of bubbles observed near the transition region to unimplanted crystal.

‡ Multi-modal size distribution observed in samples aged at room temperature for a further 9 months.

± Bubble size recorded after sample cooled back to room temperature.

4.3 Observations of Zirconium Crystal Bar Specimens

Two crystal bar samples were analyzed, labeled Xtal-1 and Xtal-2. Both samples were prepared with the FIB using the methodology described in section 3.3.3. The crystal bar material had the lowest concentration of contaminants of the three zirconium materials investigated (refer to table 3.1).

4.3.1 Xtal-1: As-Implanted

Figure 4.2 is a STEM micrograph of the sample taken immediately after FIB thinning. The figure shows many irregularities in the sample which was subsequently thinned further in the FIB and argon-plasma cleaned to remove any artifacts from the FIB process. Although no well-defined bubble-like features are observed in the image, there is a clearly defined high dose implantation layer within the sample

from approximately 0.3 µm below the implantation surface, extending to a depth of approximately 0.6 µm. This range is in good agreement with the TRIM predictions for high dpa and high helium concentration in the metal after implantation (refer to figure 4.1.

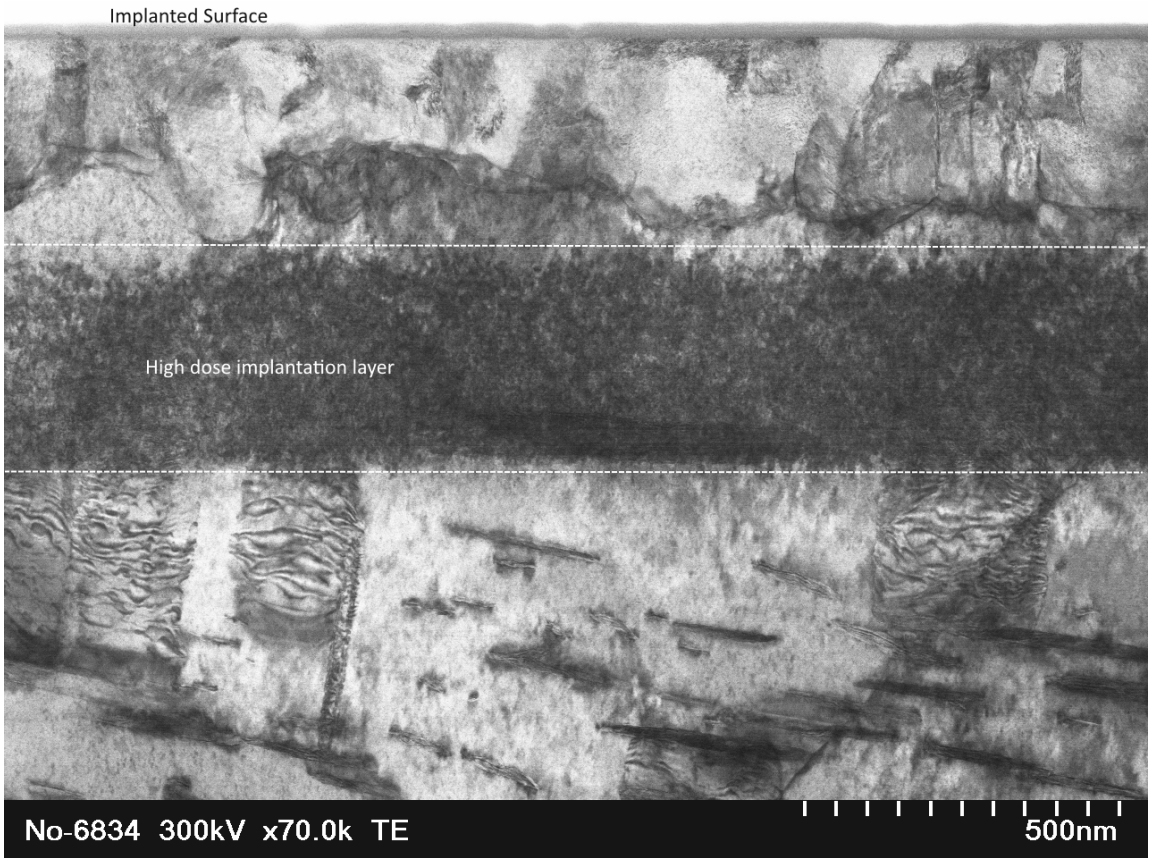

Fig. 4.2. STEM image of specimen XTAL-1 which clearly shows a change in the specimen at the depths predicted to have the highest helium concentration and dpa. The top and bottom dashed lines are approximately 0.3 and 0.6 µm from the implanted surface, respectively. This sample was determined to be too thick and was further thinned in the FIB.

A low magnification, room temperature image of Xtal-1 is shown in figure 4.3. This is the sample after the additional thinning and plasma cleaning that was performed after acquiring figure 4.2. The figure shows a region of the sample where

the tungsten layer and a portion of the carbon layer (added during the FIB sample preparation) were removed during the additional sample thinning treatment (top left of image). The high dose implantation layer is not as well-defined under these imaging conditions but is still visible. The preparation of Xtal-1 for TEM characterization resulted in some residual Ga contamination, primarily concentrated at the Zr-C interface, it is seen in figure 4.3 just below the C layer, above the high dose implantation layer and was confirmed as gallium with energy dispersive x-ray spectroscopy.

Due to the residual gallium contamination, imaging of details in the implantation layer was limited near the top of the sample. Figure 4.4 shows a series of images taken from the interface of the bottom of the implantation layer and the unimplanted region in three focus conditions. Some features that appear "bubble-like" are visible in the focused condition however they are more easily distinguished in the out of focus images. In the underfocus condition small ($\sim$1 nm in diameter) bright spot features are visible and in the overfocus condition there are equivalent dark spots. Crystal structure lattice fringes are visible in the un-implanted material and are less clear in the implanted region. It is possible, considering the high helium concentration in this region of the sample, that a bubble lattice would have formed during implantation, though this generally occurs with implantations performed at elevated temperature. Although the contrast of bubbles and cavities changes from light to dark in over- and under-focus conditions and the metal crystal structure would be expected to change in the presence of a bubble lattice, these small features were not conclusively determined to be bubbles based on this observation as the region available for clear TEM imaging in this sample was relatively small due to the gallium concentration and suspicion that the sample was not thin enough.

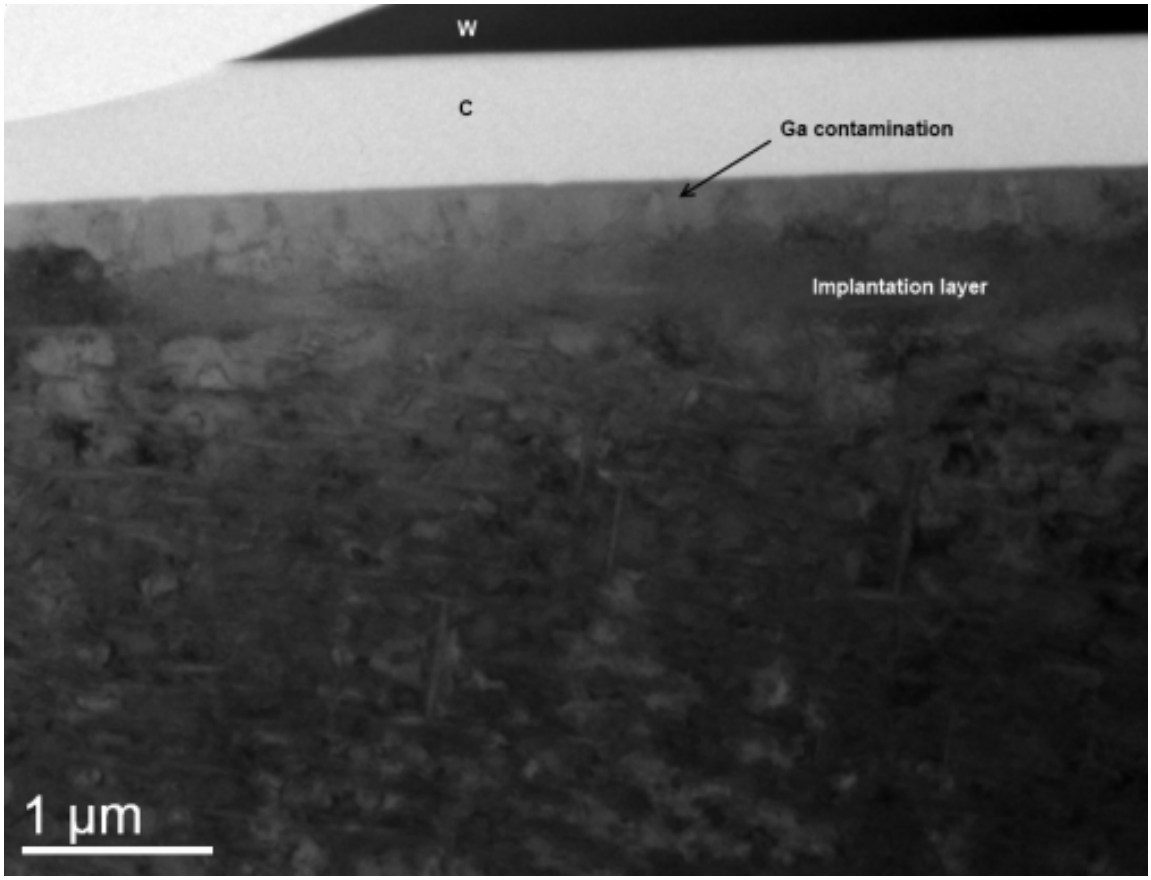

Fig. 4.3. Low magnification TEM image of sample Xtal-1 showing the W and C layers. The region on the left shows all of the W and part of the C protective layers were removed during sample thinning. A large amount of residual Ga contamination exists near the top of the sample, beneath the carbon layer which was confirmed by EDS.

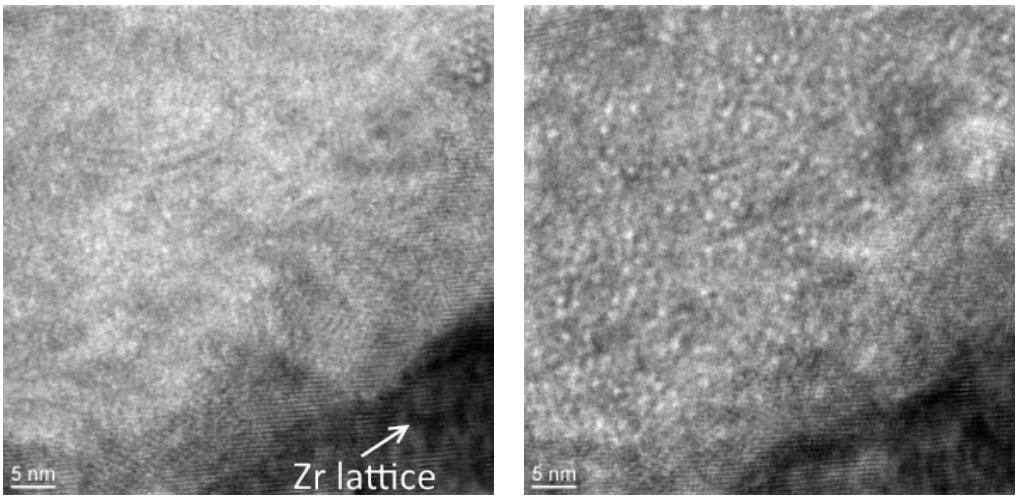

(a) Focused

(b) Underfocus

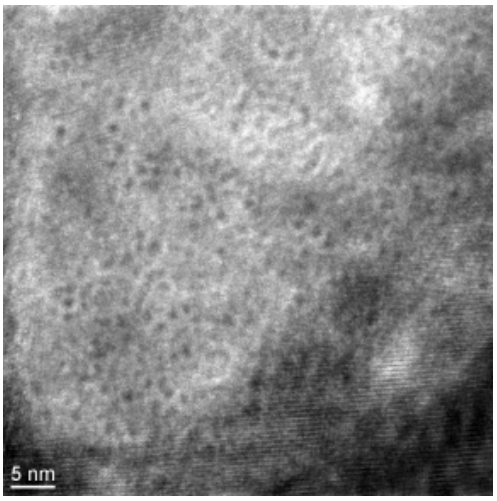

(c) Overfocus

Fig. 4.4. Nano-scale features observed in sample XTAL-1 at the bottom of the implantation layer in three different focus conditions. Dark region at the bottom right is the undamaged and unimplanted crystal. Small ($\sim$ 1nm diameter) features appear in light and dark contrast between the overfocus and underfocus conditions.

4.3.2 XTAL-1: Annealing

Sample XTAL-1 was mounted to a heating chip similar to the method shown in Figure 3.4 and heated to a maximum temperature of 450 °C. Imaging of the sample features was obscured upon heating due to sample bending which caused a high degree of strain contrast, migration of the Ga contamination across the sample surface, and difficulty in maintaining focus as the sample underwent thermal expansion. The sample was first heated to 200 °C for approximately 1 hour, and then increased to 350 °C for 1.5 hours. No significant changes or bubble-like features were observed during annealing at these temperatures and no changes were observed in the region of highest implantation dose shown in the as-implanted sample images.

Significant strain contrast was observed in XTAL-1 during heating due to the method in which it was mounted to the heating chip. Figure 4.5 shows the strain contrast at 350 °C. The strain contrast appears to stop near the high dose implantation layer. This suggests a change in the material properties has occurred in the implantation layer. It is possible, and somewhat expected, that the high helium concentration predicted in the high dose region of the sample (˜ 20 atom percent) would lead to material property changes as the high concentration of helium atoms would *stiffen* the surrounding zirconium matrix. Another possibility is a change in the crystallographic structure of the metal in this region due to the presence of the high density of small helium bubbles, however, Figure 4.4 of the as-implanted structure is inconclusive as to whether this region is a bubble lattice or just a region of randomly arranged bubbles. Neither possibility can be confirmed from the observations available.

The gallium surface contamination, confirmed with EDS, became mobile at approximately 300 °C and migrated away from the implanted surface toward the middle of the specimen. The repositioning to this region could be due to the thermal strain profile within the sample or a consequence of and underlying change in material properties in the high helium dose layer.

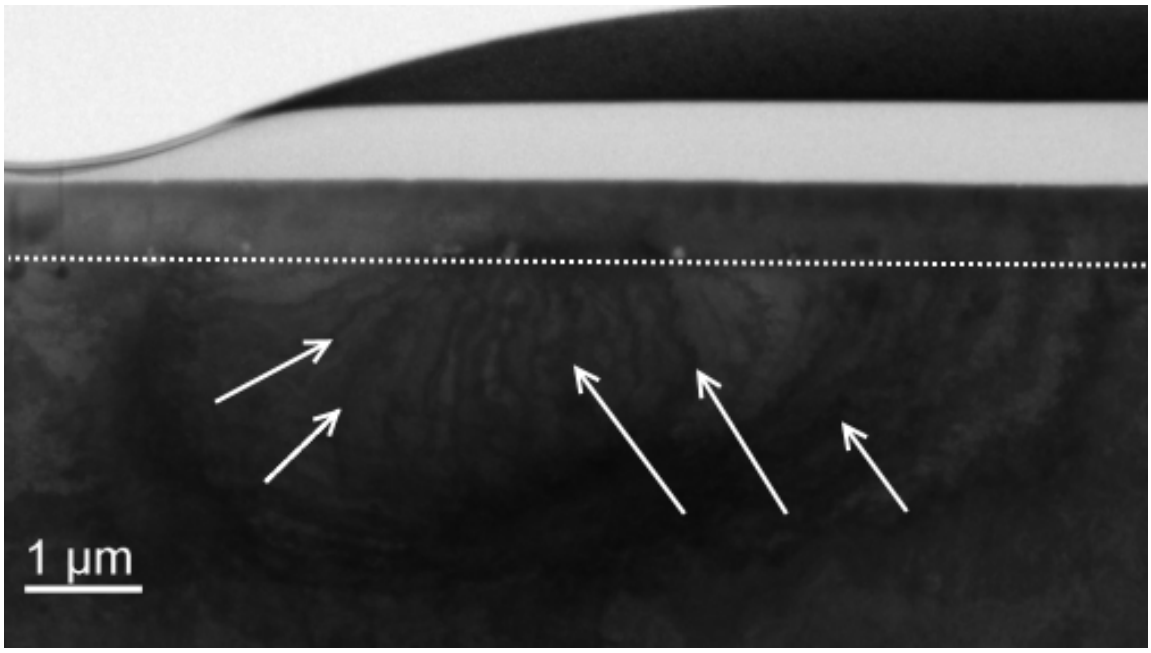

Fig. 4.5. XTAL-1 at 350 °C showing strain contrast in the center of the specimen (marked by arrows). Strain contrast ends at the implantation layer (dashed line), 2 kX.

Figure 4.6 is a comparison image of the bubble population near the implanted surface (top of sample) after the sample had been heated to 400 °C for approximately 120 minutes and after the temperature had been increased to 450 °C for 15 minutes . A few features in subfigure (a) appear bubble-like near the implantation surface, though they are not well-defined in the image, they appear to have a major dimension on the order of 20-30 nm. Shortly after increasing the temperature by 50 degrees the features appear more clearly. A few 30-40 nm diameter features are visible in subfigure (b). Bubble size increases rapidly with temperature and the relatively quick change in size of the feature observed in this sample suggests that they may be bubbles, though at their size scale of tens of nanometers they would be expected to be more clearly defined unless they have a highly irregular shape.

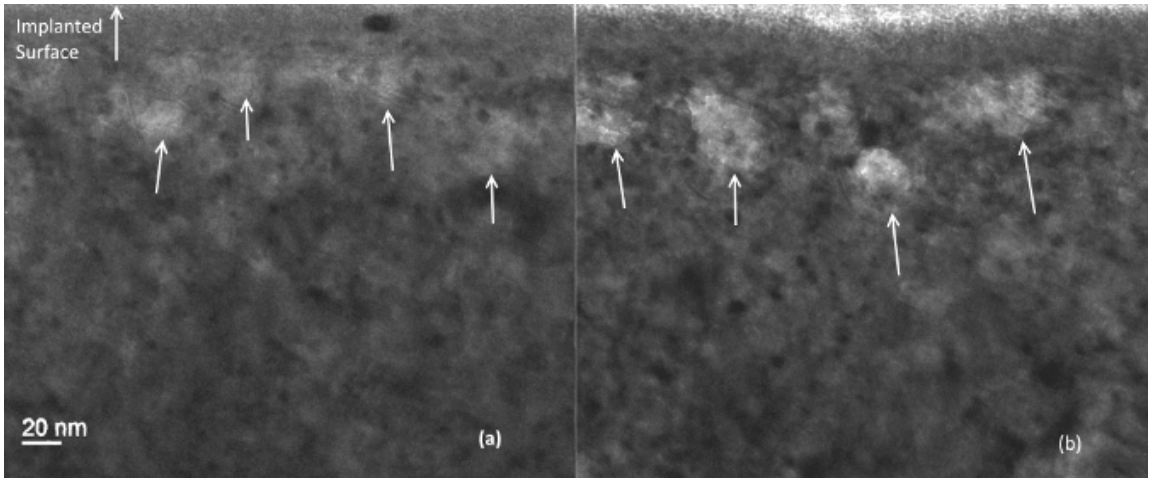

Fig. 4.6. Image of sample XTAL-1 near the implantation surface after annealing at 400 °C for 2 hours in the underfocused condition (a); and after 15 minutes at 450 °C in the focused condition (b). Arrows point to bubble-like features present near the implantation surface that grew in size after the temperature increase.

Figure 4.7 shows a series of images (selected from a digital video recording) taken near the sample surface (the amorphous carbon layer is visible at the top of the images) which show the evolution of several faceted features during heating. The first image, *a* shows the sample immediately after increasing the temperature to 450 °C and the remaining images were taken while holding at temperature over the next 15 minutes. Several regions have been marked on the image (*x,y,z*) to highlight areas with a high concentration of mobile and changing structures. The structures of interest are highly faceted and appear to have a planar shape as significant overlap is visible (see region *x* in subfigure (b) for example).

The images show many irregular-shaped structures of varying size and shape. Region *x* shows three clearly discernible, overlapping structures that coalesce over time; the resulting structure has retains a faceted shape. It is difficult to discern the exact boundaries of the structures in the first few subfigures prior to coalescence. The irregular shapes suggests the structures may be planar in nature as some of them

have dimensions on the order of 40-50 nm and would be expected to be more clearly discernible if their depth dimension was in the same order. Subfigure (f) shows structures that appear more like faceted bubbles and have more easily discernible boundaries. It is likely that the structures shown in this series of images are all gas-filled cavities that have a highly irregular shape at the beginning of the series (when temperature was increased to 450 °C) and as the irregular-shaped cavities migrate and coalesce they take on a shape that is more expected for bubbles.

Similarly, region *y* shows a group of irregular and faceted structures of varying size that undergo coalescence over time. Image (e) in the figure shows the development of strain contrast that appeared momentarily during the observation with a triangular shape (marked by arrow). After the strain contrast has disappeared, many of the smaller structures are no longer observed. This contrast could be due to the development and subsequent relaxation of matrix strain during the migration and coalescence of the faceted structures. Another possible explanation is the the escape of a faceted bubbles from the sample surface. Region *z* shows a large, triangular bubble that is not visible after the appearance of the strain contrast.

Based on these observations, the structures observed to migrate and coalesce are thought to be irregularly shaped helium bubbles within the metal.

No observations were made in the high dose implantation layer of the specimen during the annealing process. The migration and growth observations made were near the implanted surface of the sample where the helium concentration was comparatively lower.

Figure 4.8 is a low magnification image of sample XTAL-1 after the heating process that shows the gallium contamination has migrated away from the implanted surface to just below the implantation layer. A thin line of bubbles near the implanted surface is visible.

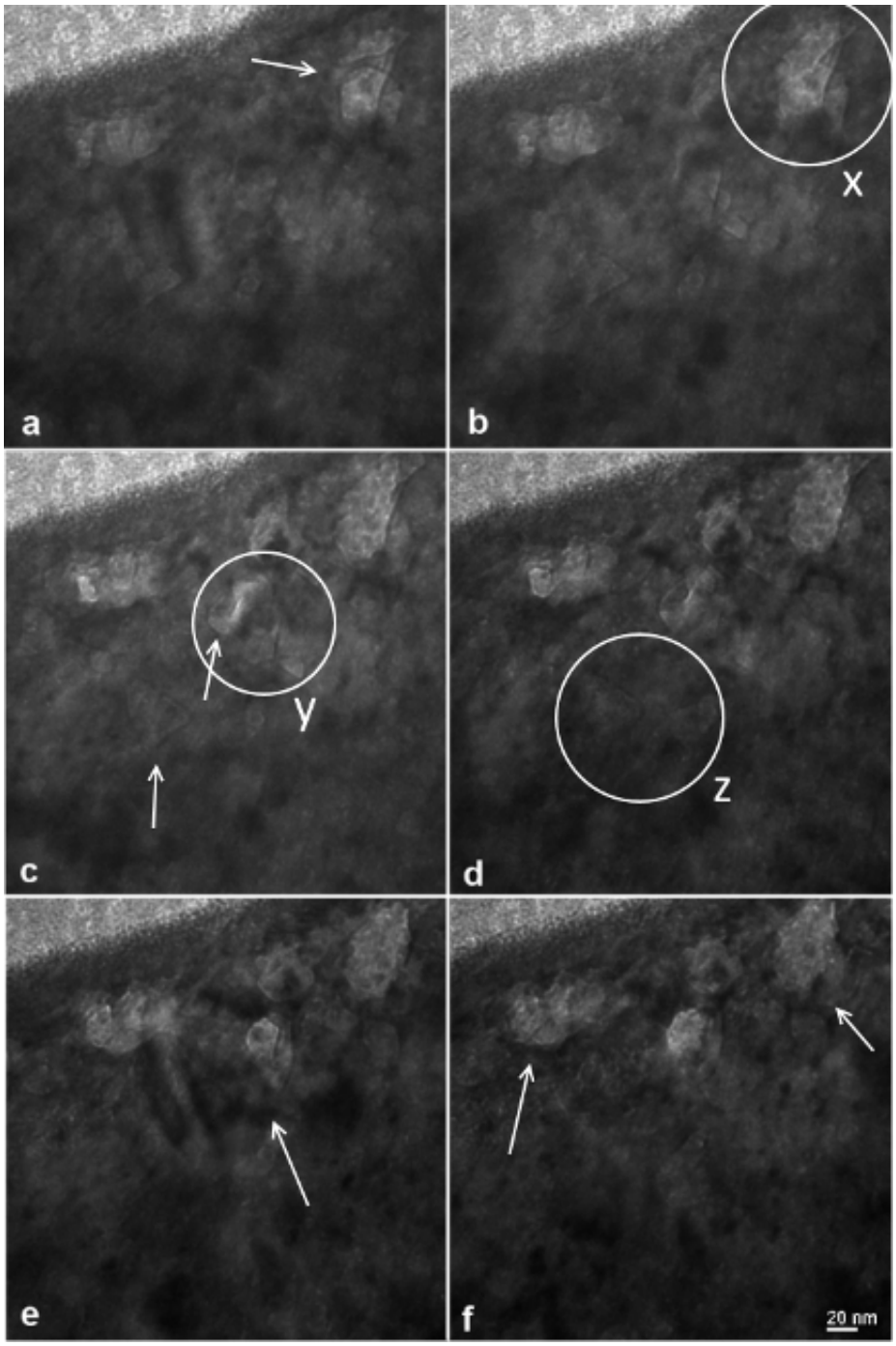

Fig. 4.7. Series of faceted bubbles in XTAL-1 observed to coalesce while the sample was at 450 °C. The time span from image (a) to (f) is approximately 15 minutes. The highlighted regions *x,y* and *z* are discussed in the text. 70 kX.

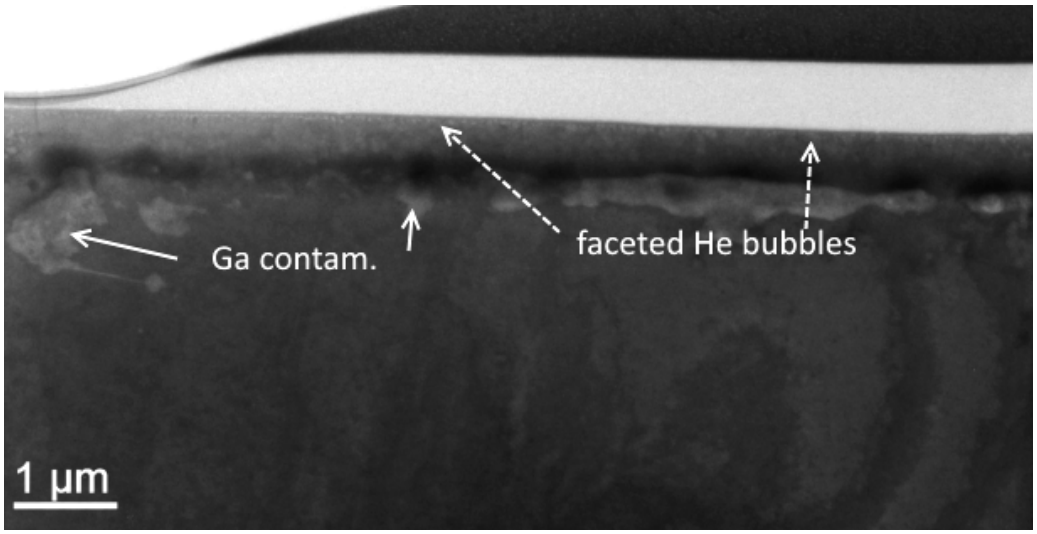

Fig. 4.8. Sample XTAL-1 at room temperature after annealing. The Ga contamination is visible in the high dose implantation region and a number of small bubbles are visible near the implanted surface - at the top of the image.

4.3.3 XTAL-2

Sample XTAL-2 was observed 10 months after XTAL-1. The specimen had large (∼0.2 µm diameter) precipitates present in the sample, shown in figure 4.9(a), at room temperature. The sample was originally too thick for TEM characterization and was further thinned in the FIB. It is likely that the plasma cleaning process after this second thinning operation was insufficient as the precipitates appeared after the second thinning. The number of visible precipitates decreased after the sample was heated to 560 °C, shown in figure 4.9(b), however no migration or growth of the features was observed while the specimen was being heated.

It is unlikely that these features were due to the He implantation as they extend much deeper into the specimen than the He distribution or damage profile and do not appear to have any features consistent with the depth profile. The features were observed during heating and showed no signs of change.

Figure 4.10 shows a series of the circular features during heating from 500 °C to 560 °C. The distortion observed in figures 4.10(b) and 4.10(c) is due to the temperature change in the sample. There was no observable change in the size or proximity of the features during heating.

The unidentified precipitates, which are possibly a contaminant from the sample preparation process, were the main focus of sample characterization during the annealing phase of the work. As such, no evidence of bubble growth as observed in the sample during annealing. After heating, there were features similar to those observed in XTAL-1 near the implanted surface and near the top of the high dose implantation layer, seen in figure 4.9(b). It is expected that helium bubbles grew near the implanted surface in a similar manner as the other XTAL sample and the increased temperature could have led to bubble growth nearer to the high dose implantation layer. These regions were not investigated further.

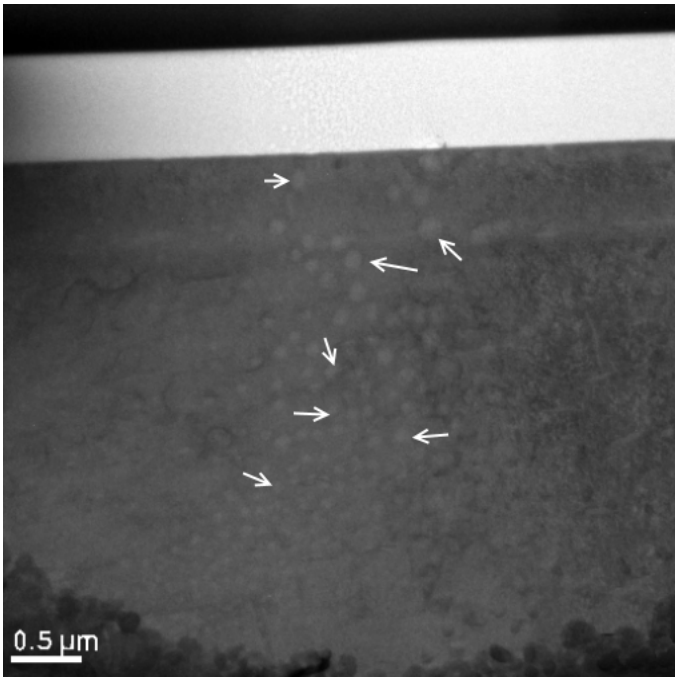

(a) Room Temperature, 4kX

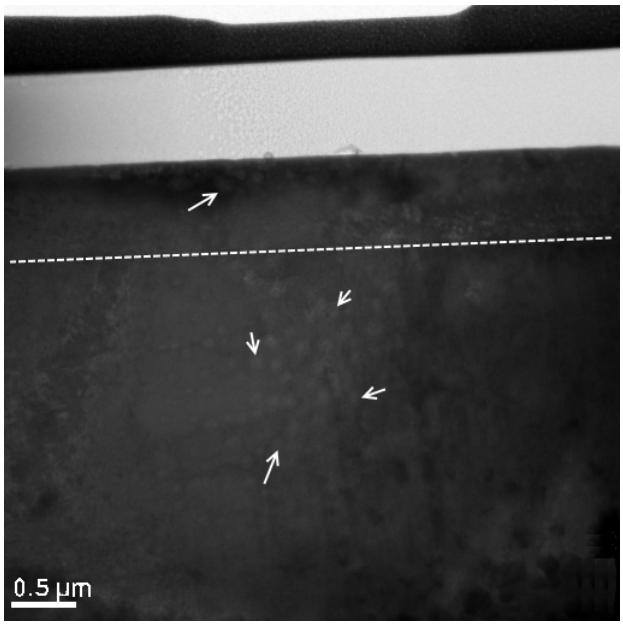

(b) 560 °C, 4kX

Fig. 4.9. Ga contamination in XTAL-2 before (a) and after (b) heating to 560 °C. Dashed line denotes the bottom of the implantation region.

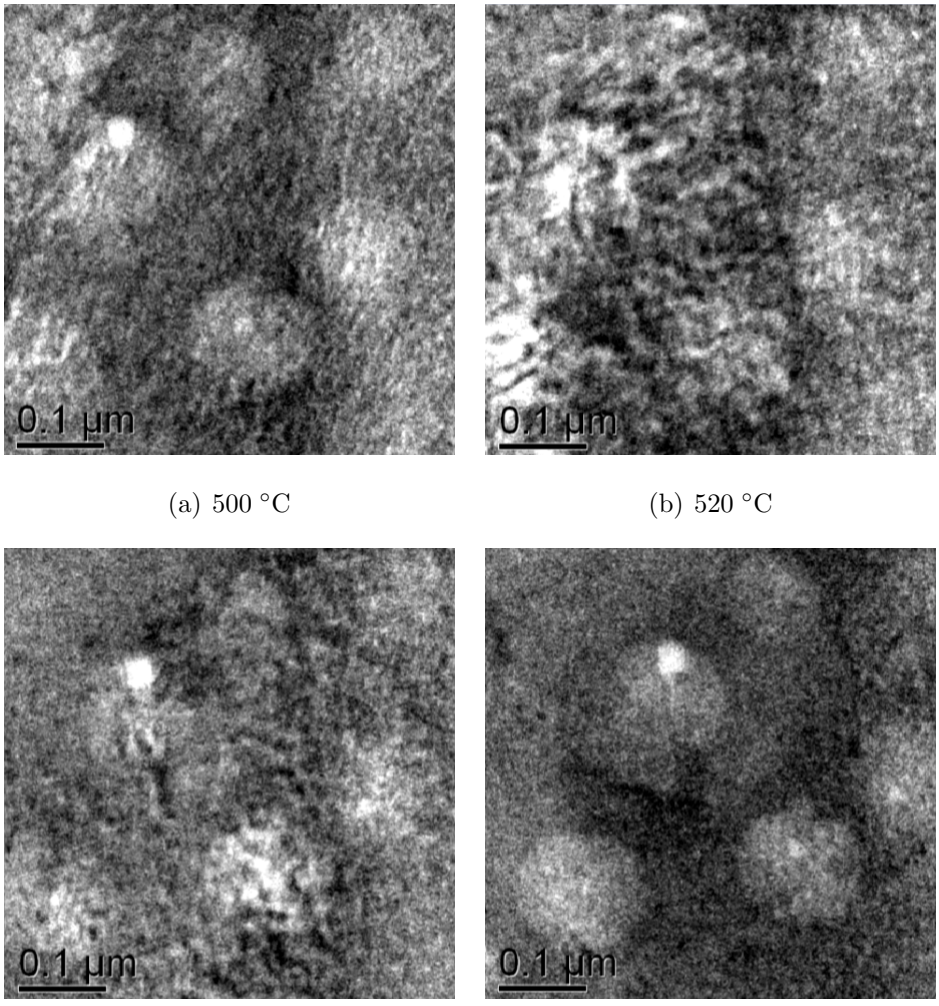

(a) 500 °C (b) 520 °C

(c) 540 °C (d) 560 °C

Fig. 4.10. TEM image of unidentified precipitates in XTAL-2 during a temperature increase from 500 °C to 560 °C.

4.4 Observations of Extruded Zirconium Specimens

The extruded zirconium samples were fabricated by high temperature extrusion of powdered zirconium metal as described in [1]. Prior to extrusion the powders were stored in a water solution and contained a high concentration of oxygen, carbon, and nitrogen relative to the other alloys (refer to table 3.1). Two samples, labeled HX-1 & HX-2 are presented; the observations of HX-2 were made 10 months after HX-1.

4.4.1 HX-1: As-Implanted

The high dose implantation region of HX-1 was located at the depth expected from TRIM calculations and had a markedly similar configuration to the XTAL samples, with a high density of small bubbles. Figure 4.11 is a TEM image at the bottom of the implantation layer showing the bubble structure in the top half of the image and the region below the implantation layer at the bottom of the image. The morphology of the bubbles are quite similar to those described in bubble lattices found in other helium implanted metals, discussed in section 2.2. The bubbles are highly faceted as expected, and have a mean diameter of ∼4 µm, as shown in figure 4.12. Bubble size analysis was performed on several regions within the high density bubble region by manually identifying individual bubbles in the Fiji image analysis software for measurement.

A higher magnification image of the interface between the implanted region and the un-implanted crystal is shown in figure 4.13. The diameter of the bubbles in this interface region appear to be approximately 1 nm though at this scale the out-of-focus imaging condition necessary to resolve the bubbles has a large effect on the observed size; the bubble density in this interface region has decreased significantly from that observed closer to the high dose implantation layer.

Figure 4.14 shows the bubble structure in the implantation layer using STEM imaging mode. In this mode, the bubbles appear as bright spots and have a more spherical (i.e., less faceted) shape, consistent with the discussion in section 2.2.

There does appear to be evidence of short-range bubble ordering in figures 4.11 and 4.14. Due to the limited sample tilt available with the heated sample stage in the TEM it was not possible to locate a viewing angle that allowed for further confirmation of bubble ordering.

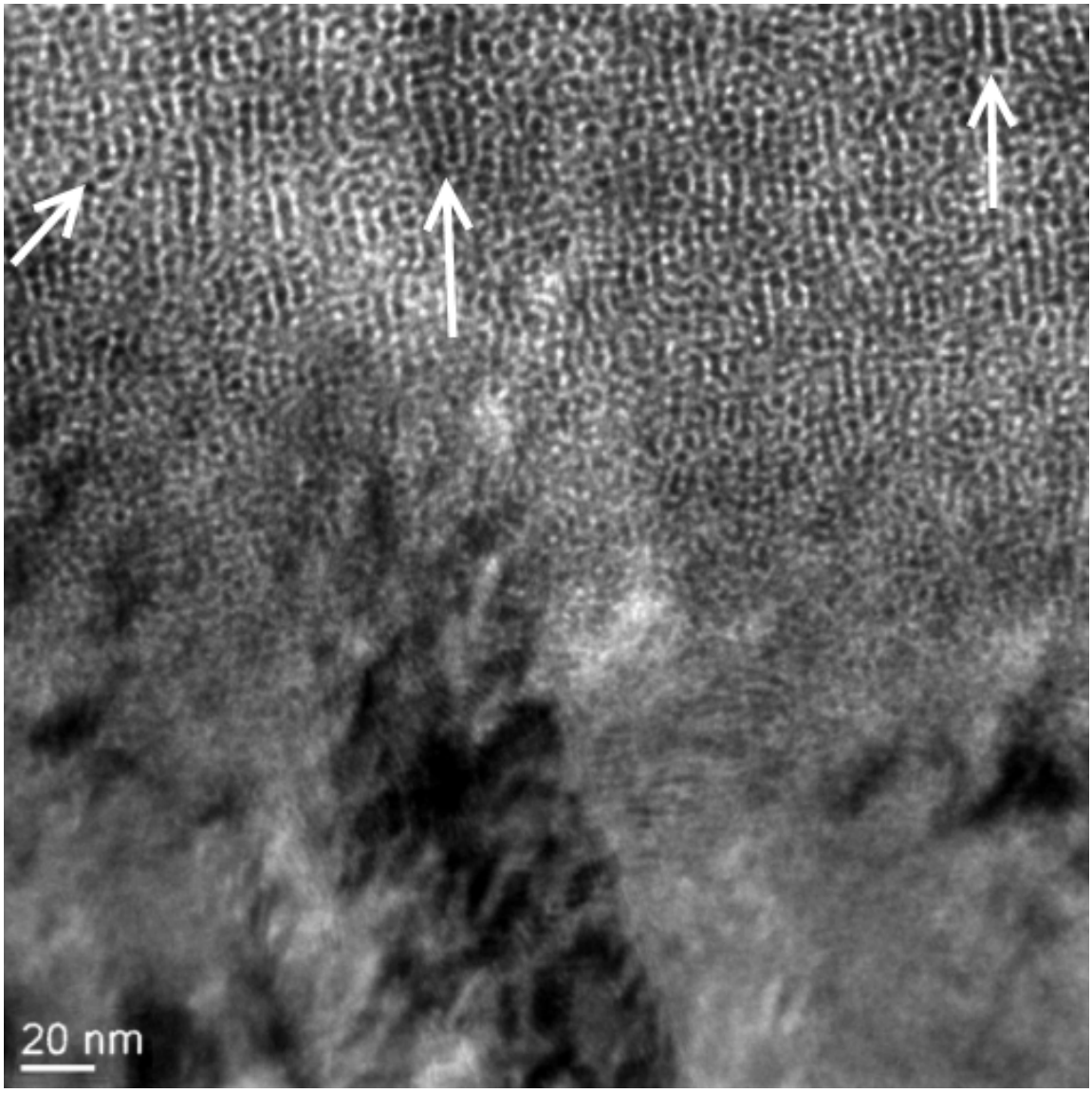

Fig. 4.11. High density bubble region in HX-1 at room temperature, as-implanted. The bottom of the image is the un-implanted region of the sample. The average bubble diameter is ∼4 nm. Arrows point to areas of apparent short-range bubble ordering. Overfocus 3 µm.

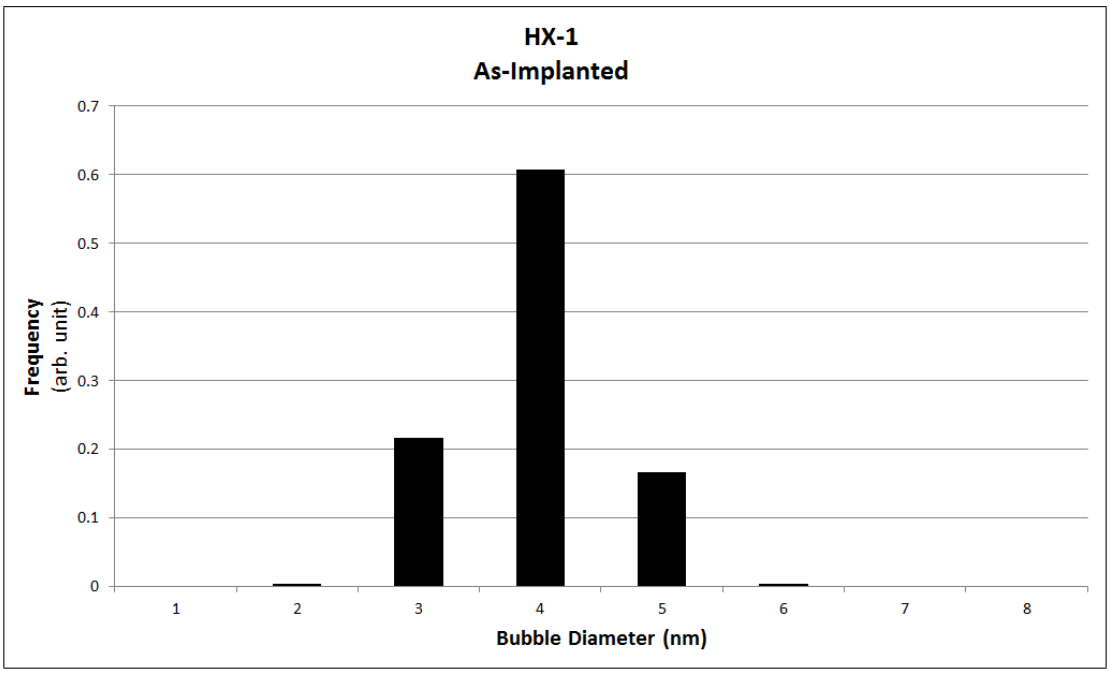

Fig. 4.12. Bubble size distribution in HX-1 in the region of highest dose; i.e. top of Figure 4.11.

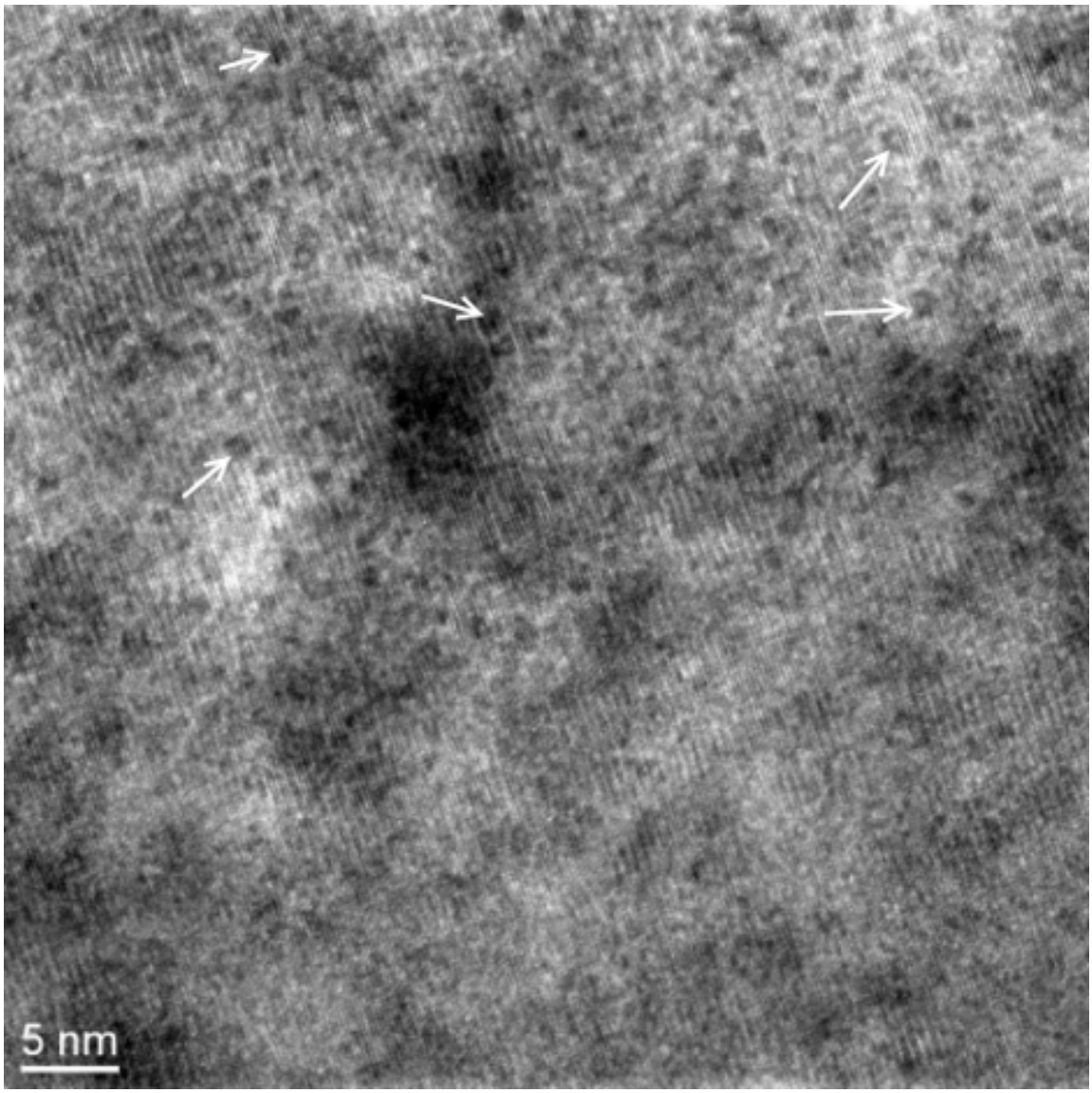

Fig. 4.13. Bubble structure in as-implanted HX-1 showing the interface between the implanted region and the un-implanted specimen. Arrows denote small bubbles. Overfocus 150 nm.

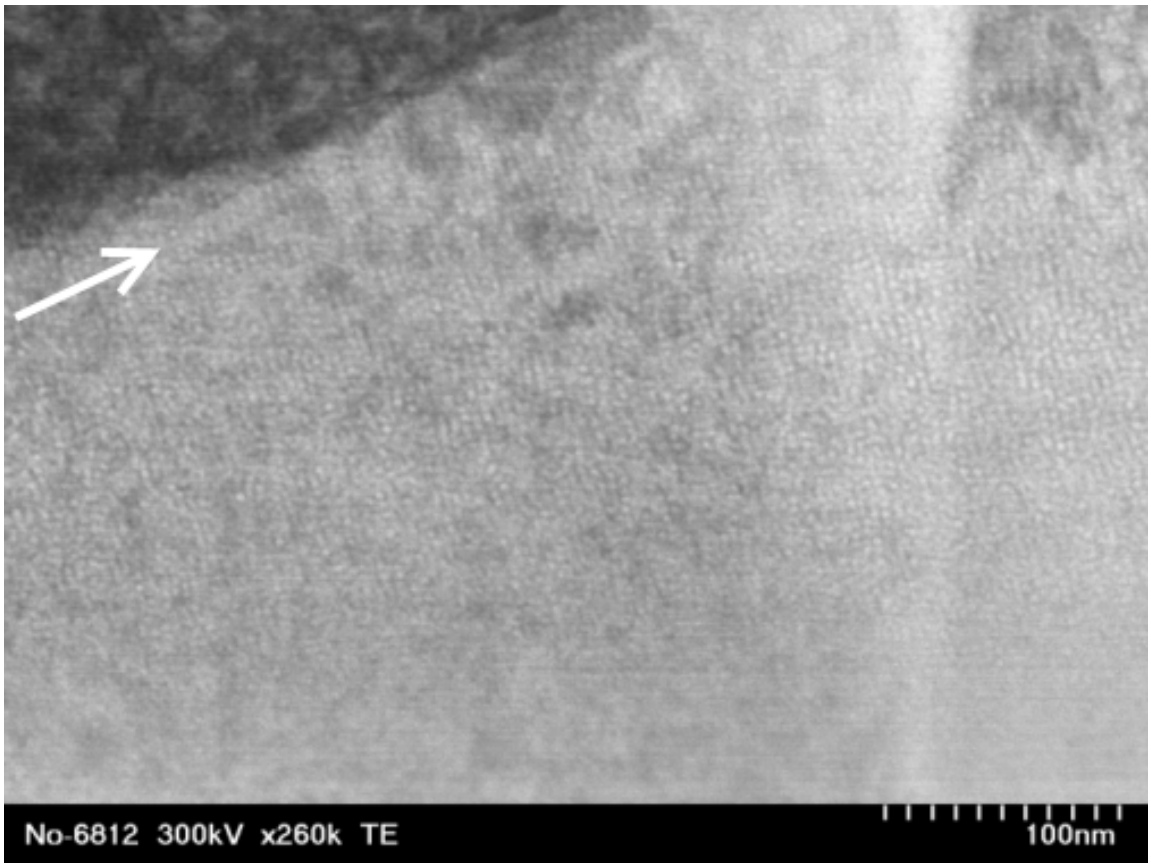

Fig. 4.14. STEM mode image of the high density bubble region in as-implanted HX-1. Bubble ordering is not evident, however the arrow points to a region of apparent short-range bubble ordering.

4.4.2 HX-1: Annealing

Sample HX-1 was heated to 450 °C in several increments over the course of five hours. No changes in bubble size or evidence of bubble migration were observed up to this temperature, and further discussion of this data is not presented.

The high purity crystal bar samples (XTAL series) showed clear evidence of bubble migration and growth at comparable temperatures. It is possible that the resistance to bubble growth at these temperatures in the extruded material is related to the high impurity concentration. Oxygen is known for its ability to trap helium-vacancy complexes in zirconium [81], and higher annealing temperatures may be required to overcome this.

4.4.3 HX-2: As-Implanted

The HX-2 sample was characterized 10 months after the first and was extensively thinned during preparation resulting in nearly all of the W and C layers being removed as seen in figure 4.15. The remaining C layer had rolled over on itself. Some of the Zr material was also removed just below the Zr-C interface on the left side of the image.

Figure 4.16 shows the region of highest helium dose in the implantation layer, approximately 0.6 µm beneath the implantation surface. The as-implanted bubble structure in this sample is noticeably different from the other samples evaluated, containing many large, faceted bubbles, up to ∼20-30 nm in diameter. These larger bubbles are concentrated in the center of the high dose implantation layer. Figure 4.17 is an overfocused image of the same region showing a the high density region of ∼5 nm diameter bubbles, consistent with the previous results. Figure 4.19 shows the large bubbles at closer magnification and reveals that they are quite circular in shape, unlike the bubbles observed during annealing in the XTAL series which grew via migration and coalescence and retained a faceted structure at 450 °C.

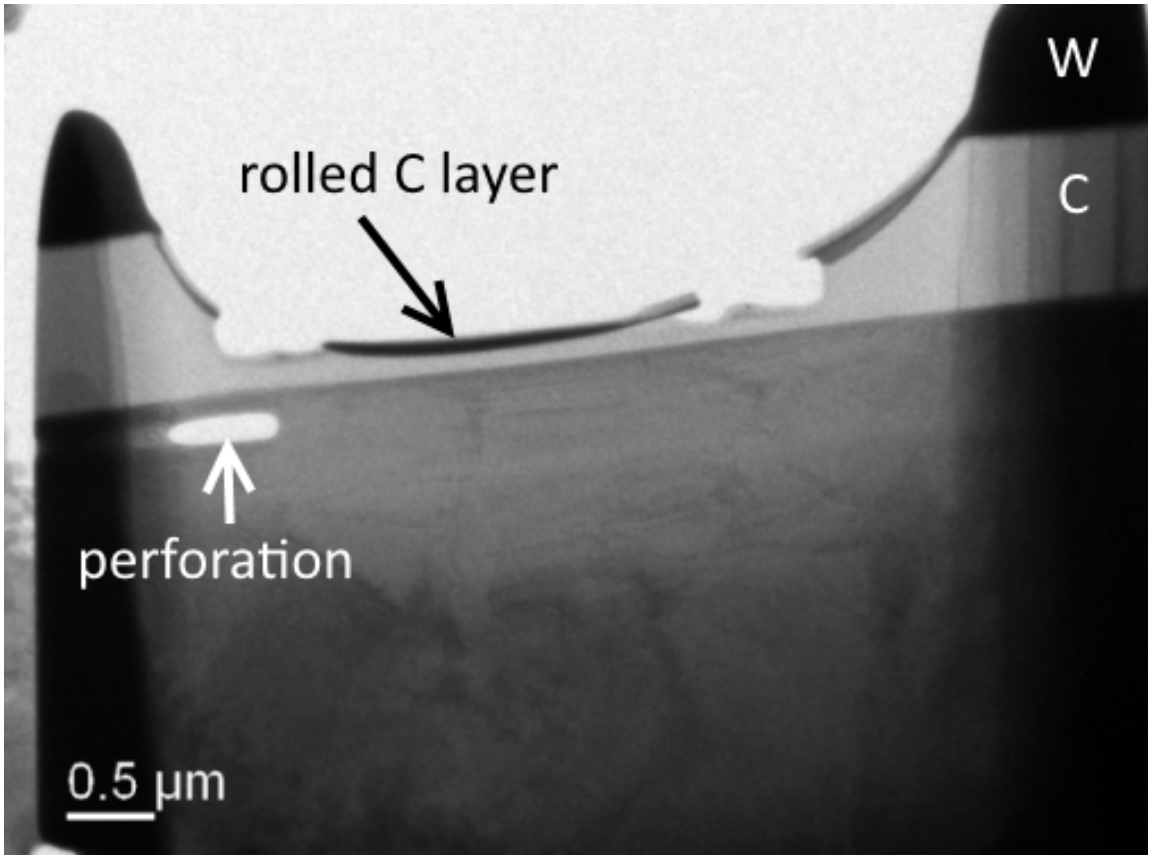

Fig. 4.15. Low magnification of HX-2 at room temperature. Much of he carbon and tungsten layers were removed during thinning of this sample and a perforation of the Zr is visible on the left side of the sample.

The size distribution of *large* and *small* bubble populations were measured using the Fiji image analysis software. Figure 4.18 shows the bimodal size distribution of this sample. The small bubble population has a consistent size of approximately 5 nm, while the diameter of the larger bubbles has a much broader distribution ranging from 10 to 30 nm. This near-bimodal size distribution developed while the sample was maintained at room temperature for 10 months. Under those conditions, thermally-activated bubble growth mechanisms would be inhibited and random-walk processes would be expected to dominate bubble growth.

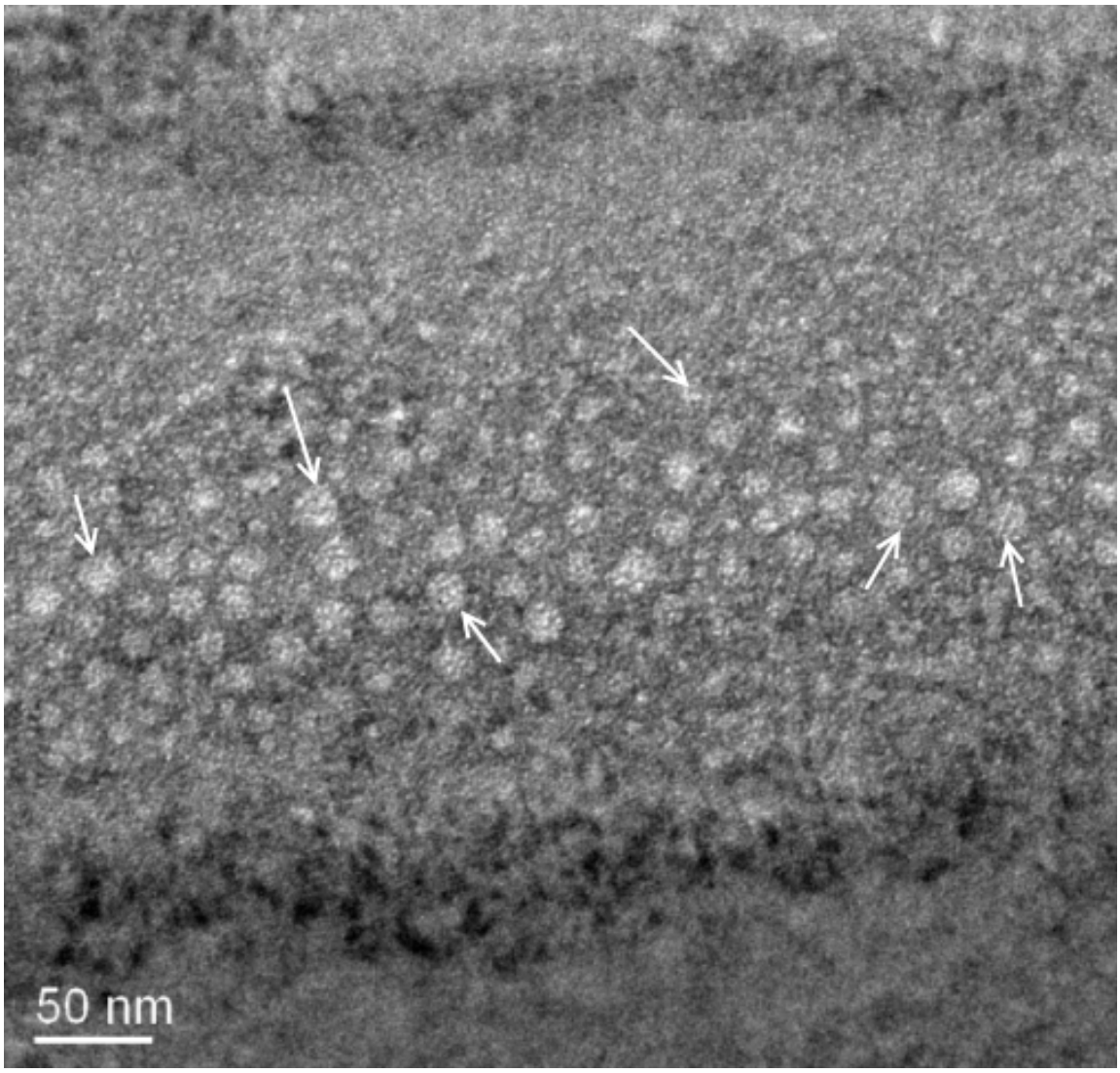

Fig. 4.16. Region of highest implantation dose in HX-2 in the focused condition at room temperature showing relatively large diameter, 20-30 nm, bubbles (marked by arrows). Figure 4.17 shows the same region in the overfocus condition.

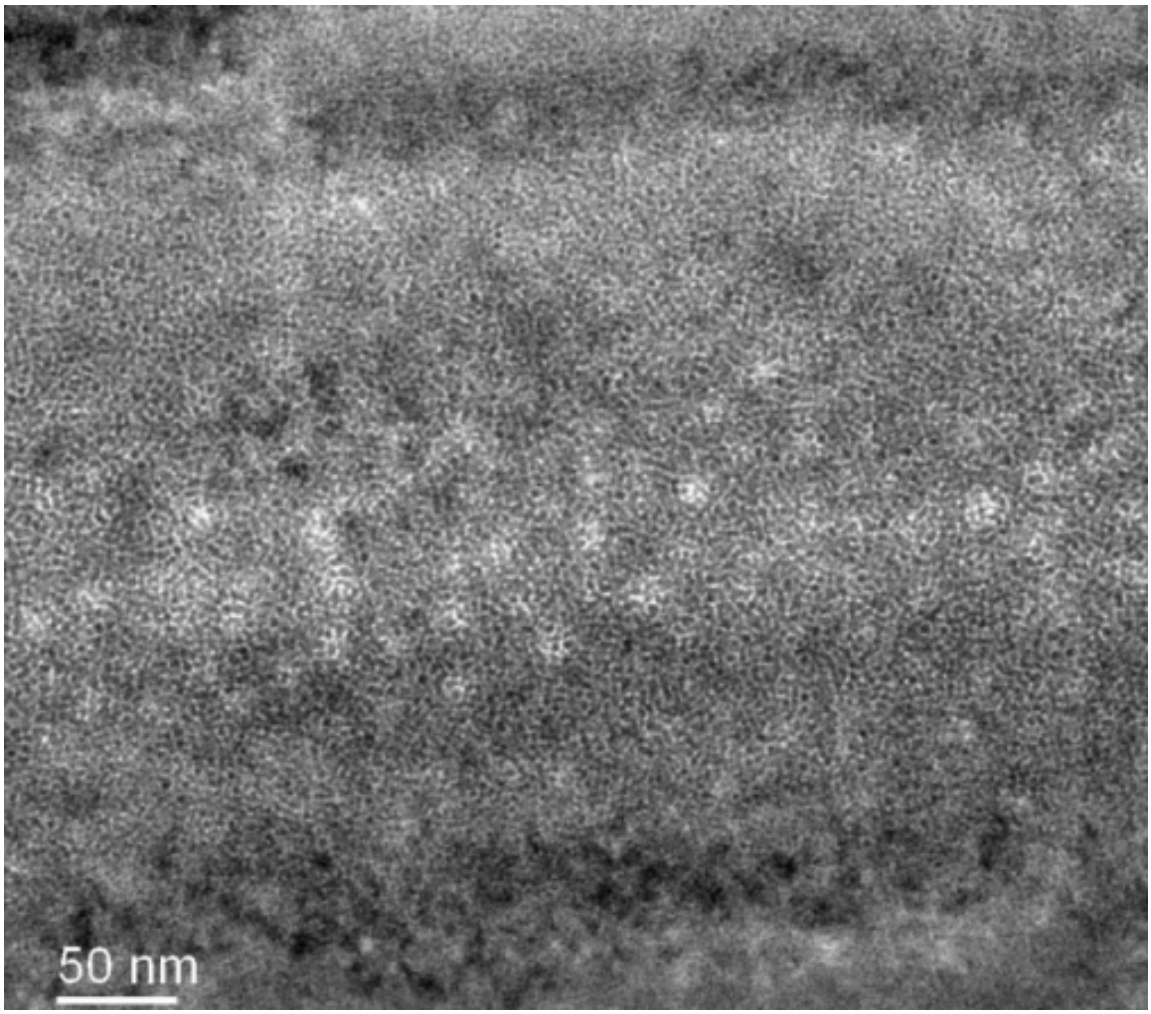

Fig. 4.17. Same region as figure 4.16 in the overfocused condition. Small bubbles visible as dark spots across the image.

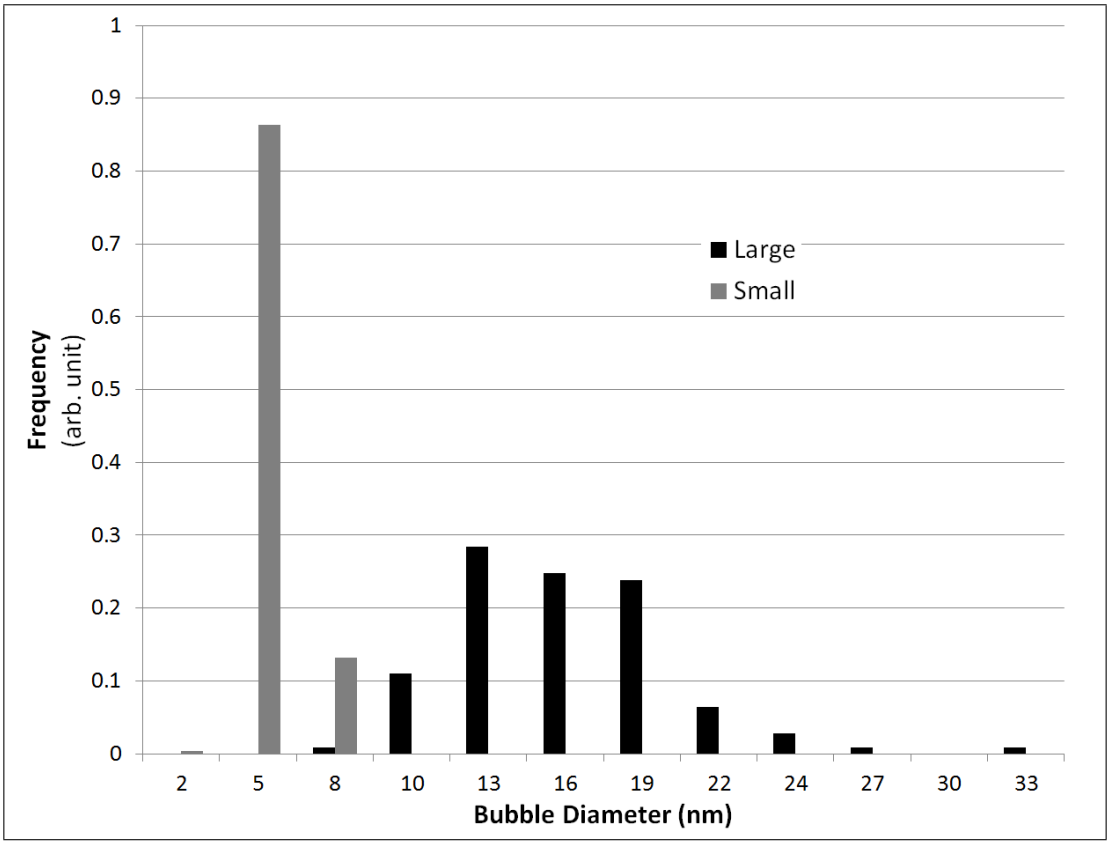

Fig. 4.18. Size distribution of bubbles in the implantation layer of HX-2, as-implanted. *Large* bubbles were visible in the focused condition (Fig. 4.16); *small* bubbles were viewed in out-of-focus condition (Fig. 4.17.

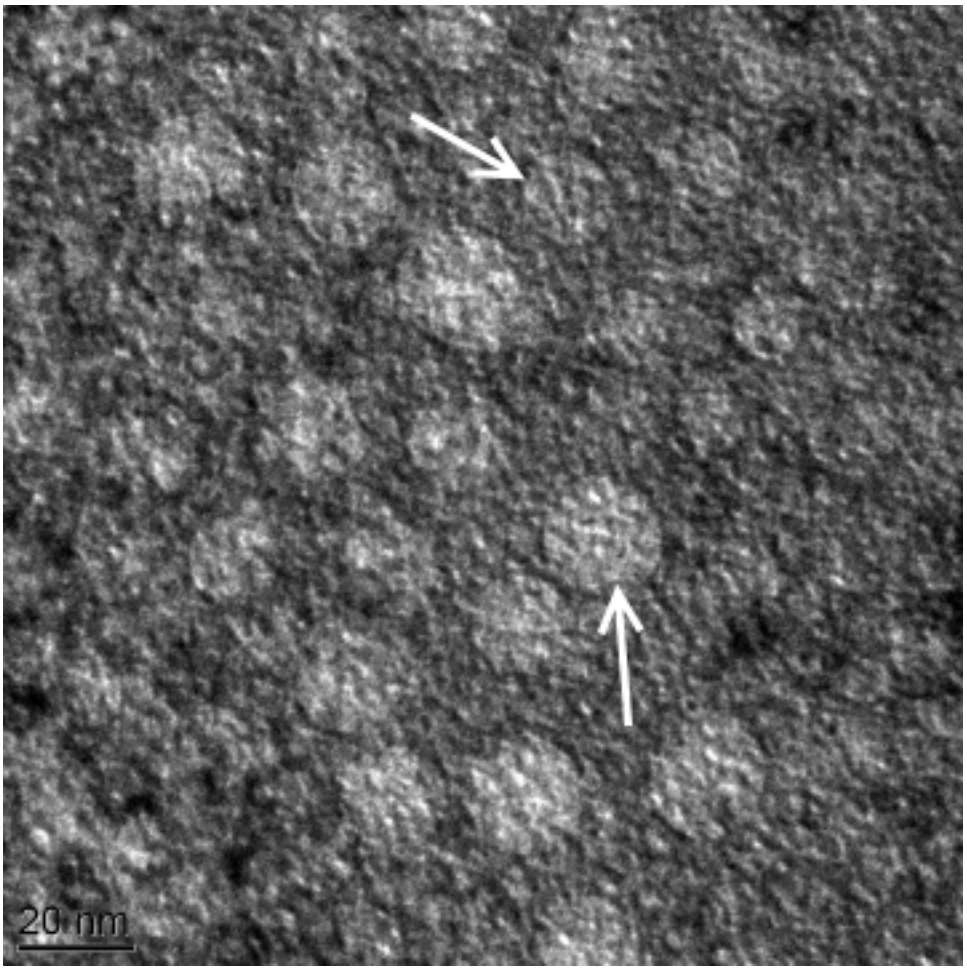

Fig. 4.19. Sample HX-2 at room temperature, showing the circular shape of large bubbles that formed during room temperature storage for 10 months.

4.4.4 HX-2: Annealing

Sample HX-2 was heated to 600 °C for approximately 45 minutes. Migration and coalescence of many faceted bubbles was observed near the implanted surface, similar to the observations made during characterization of sample XTAL-1 (refer to section 4.3.2. Little change was identified in the high dose implantation region high dose implantation region at this temperature. No images are available from this annealing step due to equipment failure during the experiment.

The sample was further heated to 700 °C to evaluate bubble response to temperature change at a higher temperature. Figure 4.20 is a series of images taken of the implantation layer at this temperature during the first few minutes after increasing the temperature. In the images the implanted surface is to the left side and the high dose region and unimplanted metal are to the right. New bubbles appeared within a few seconds of increasing the sample temperature and in the high dose implantation region, which contained a bimodal size distribution of bubbles in the as-implanted state, the large bubble population expanded during heating, marked by dashed lines in the images. In figure 4.20(a), the width of the region containing large bubbles at 650 °C is approximately 0.2 µm. In subfigure (d), taken 6 minutes later, the width of the large bubble population region has expanded by two to three times. The highest population of new large bubbles formed toward the top of the specimen, suggesting that bubbles did not migrate far away from the implantation region.The size of the bubbles has also increased substantially over the relatively short time frame observed.

Figure 4.21 shows the sample after cooling to room temperature in the TEM. The perforation is visible at the top of the sample as well as the carbon layer, which curled during annealing (large black spot at top right). Many large faceted bubbles are visible in the focus condition with a wide range of diameters from 10-40 nm. Due to the data lost by equipment failure, no further information is available regarding the bubble population near the sample surface.

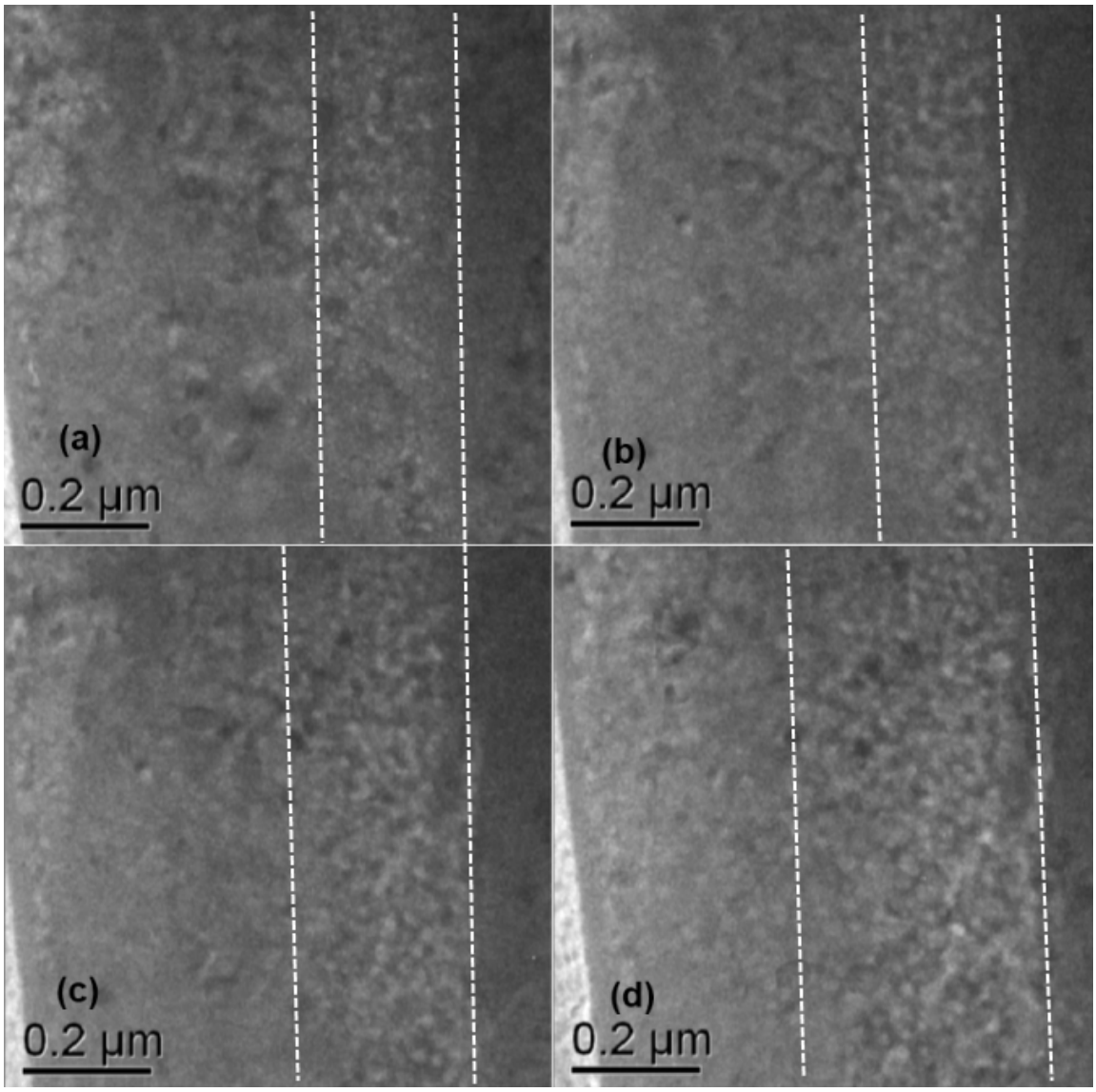

Fig. 4.20. HX-2 at 650 °C (a); series of images taken in the 6 minutes immediately following temperature increase to 700 °C (b-d). Dashed lines denote expansion of the region of the specimen populated by large bubbles.

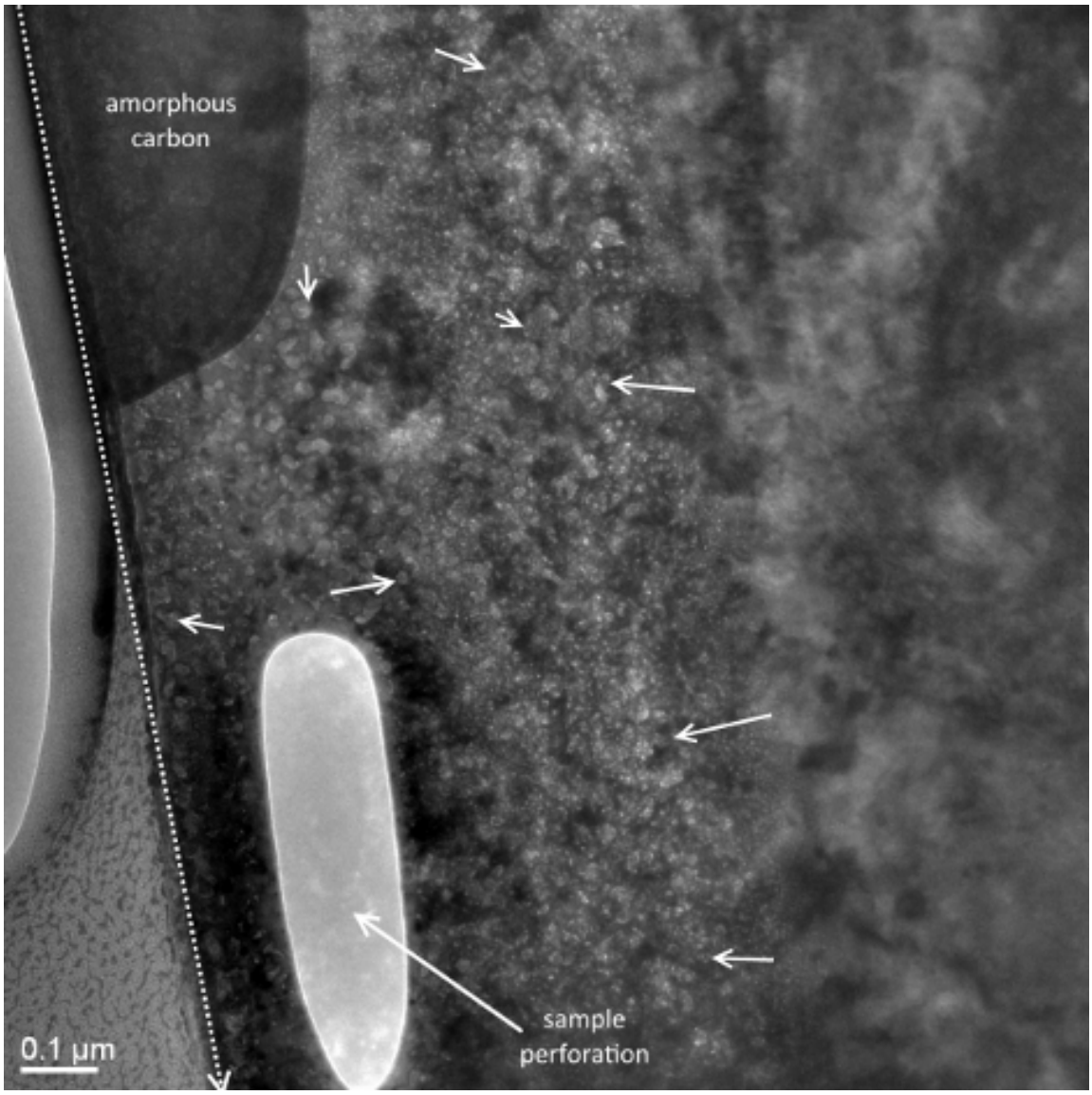

Fig. 4.21. Sample HX-2 after heating (T_{max} = 700 °C) in overfocused condition. The implanted surface is denoted with the dashed line; the amorphous carbon layer curled over during heating and obscures a section of the sample. Arrows denote highly faceted bubble structure within the implantation region.

4.5 Observations of Zircaloy-4 Specimens

Two Zircaloy-4 samples are presented, labeled Zr4-1 and Zr4-2, where sample Zr4-2 was characterized 10 months after Zr4-1. The Zircaloy-4 alloy was chosen to compare any impact the alloying additions may have on inert gas bubble dynamics, refer to 3.1 for alloy composition.

4.5.1 Zr4-1: As-Implanted

This sample had a significant amount of residual Ga contamination from the FIB sample preparation and was too thick to view bubbles in the as-implanted state. Further thinning was not performed because of concerns of destroying the sample.

4.5.2 Zr4-1: Annealing

The specimen was heated to 450 °C for 30 minutes and bubbles grew large enough to become visible in the high dose region of the implantation layer (approximately 0.5 µm deep), as shown in figure 4.22. The mean bubble diameter, measured with Fiji image analysis, is ∼21 nm; a size distribution histogram is shown in figure 4.23.

A direct comparison to the bubble population in the high dose implantation region of sample HX-2 cannot be made due to the different conditions of the samples when the populations were characterized. However, it may be worthwhile to note that the bubble size observed in sample Zr4-1 at 450 °C is similar in magnitude to the *large* bubble population that formed in HX-2 during room temperature storage for 10 months.

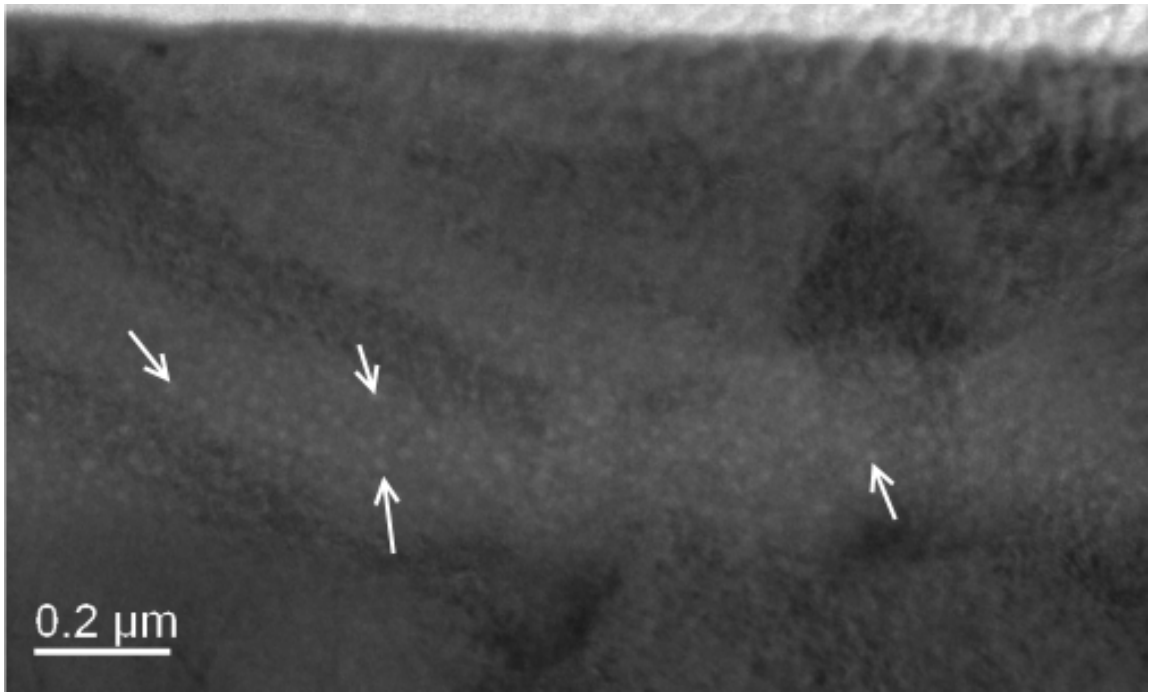

Fig. 4.22. Bubbles in Zr4-1 after annealing at 450 °C for 30 minutes. Arrows denote bubble population.

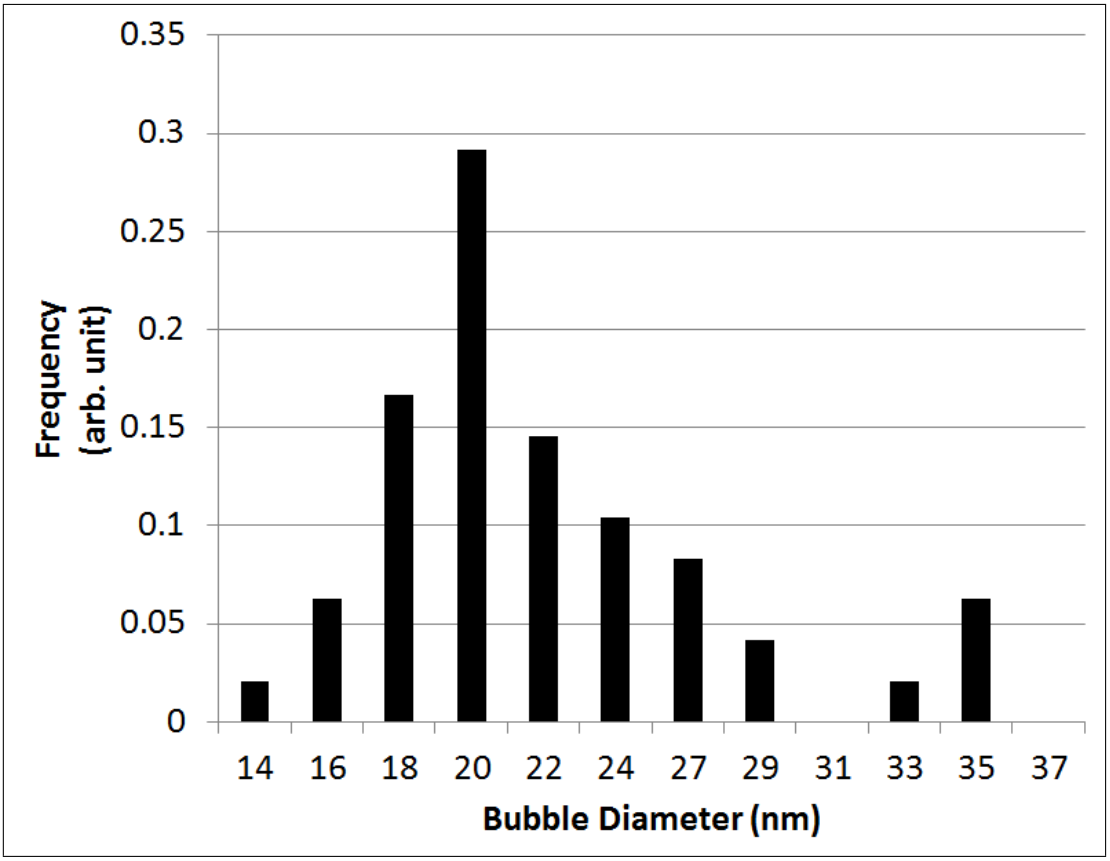

Fig. 4.23. Bubble size distribution in Zr4-1 after heating to 450 °C. Measured from figure 4.22.

4.5.3 Zr4-2: As-Implanted

Figure 4.24 shows the as-implanted sample at low magnification. Though not as easily distinguishable as the *large* diameter bubbles in observed in sample HX-2 (figure 4.16, this sample also had a bimodal bubble size distribution with a population of 10-20 µm diameter bubbles present in the high dose region. There are too few of these bubbles visible to make an accurate measurement of the size distribution. It is likely that the sample was too thick in the implantation layer for adequate observation of the larger bubbles.

Figure 4.25 is an overfocus image of the high dose implantation region showing the high density of small bubbles. The size distribution of these small bubbles is shown in figure 4.26 and the average diameter is $\sim$ 4 nm, consistent with the other zirconium metals evaluated.

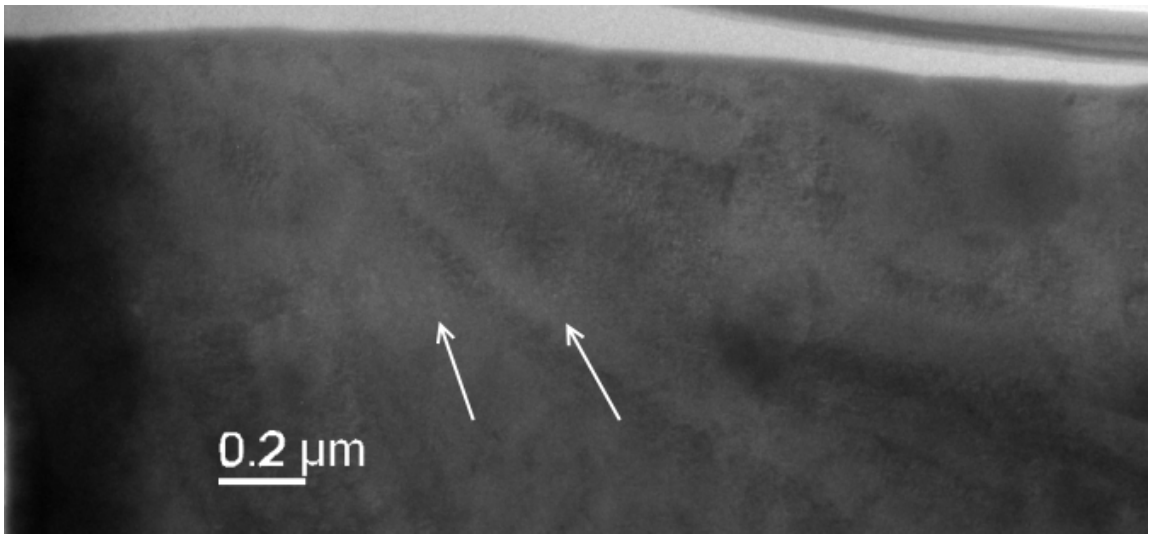

Fig. 4.24. Zr4-2 as-implanted. A population of *large* bubbles is observed in the high dose implantation region, marked by arrows. The small bubbles from this region is shown in figure 4.25.

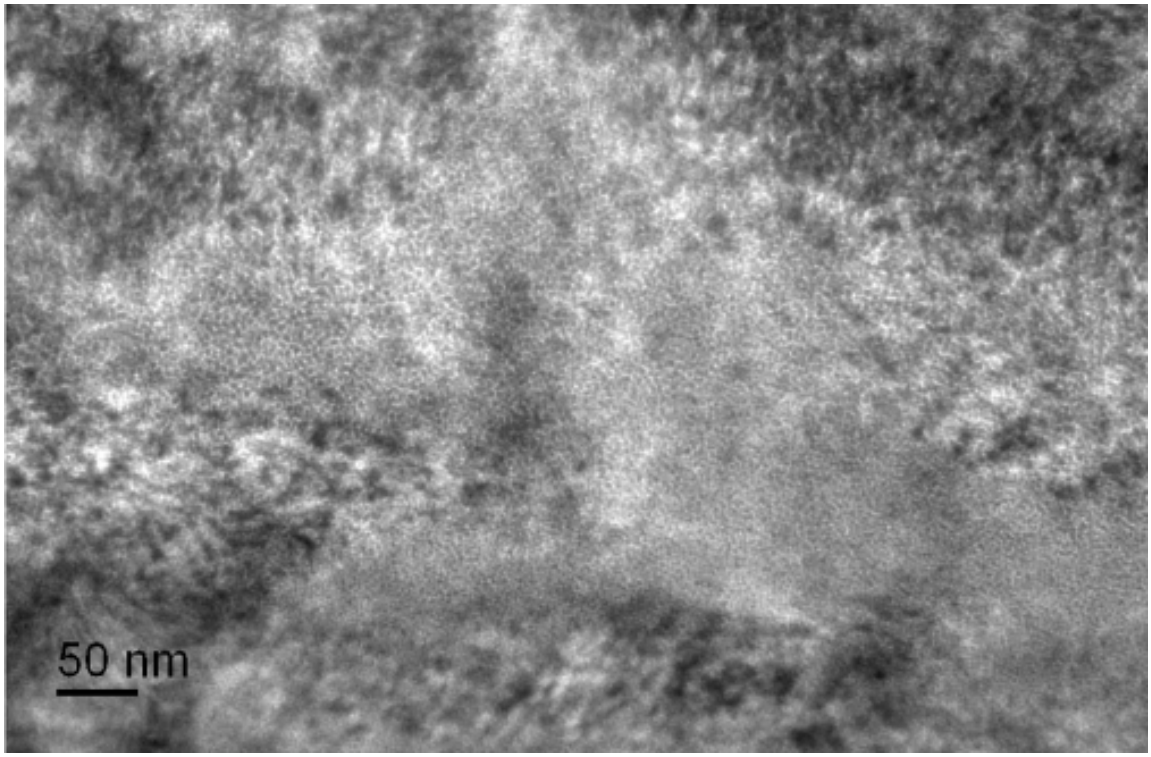

Fig. 4.25. Overfocus image of Zr4-2 showing small bubbles in the high implantation dose region as dark spots.

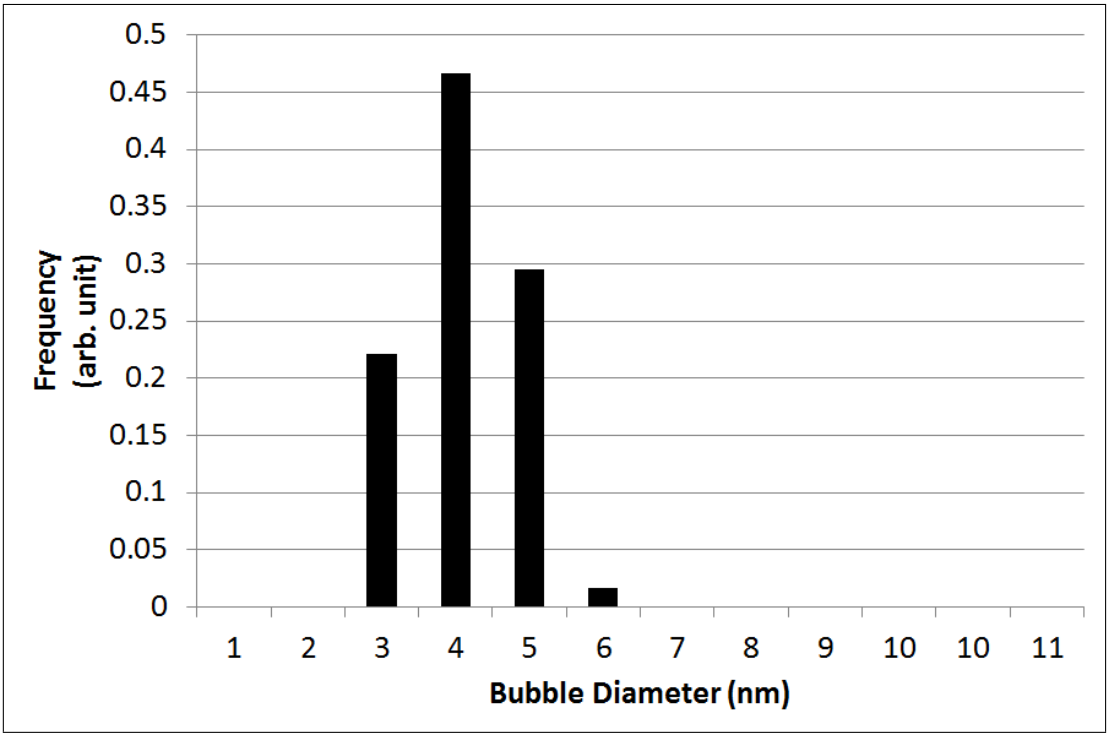

Fig. 4.26. Bubble size distribution of as-implanted Zr4-2; does not include *large* bubble population visible in Figure 4.24.

4.5.4 Zr4-2: Annealing

The sample was heated to 450 °C and the population of 10-20 nm bubbles grew in size and density, becoming easier to distinguish. Figure 4.27 shows a population of $\sim$ 20 nm diameter bubbles in the implantation layer near a possible grain boundary.

After $\sim$ 25 minutes the specimen temperature was increased to 550 °C. Figure 4.28 shows the implantation layer in the focused and underfocused condition at this temperature. The population of *small* bubbles is still present at this temperature.

A comparison of the mean bubble diameter at 450 *a*nd 550 °C shows no significant change in average bubble size for the *large* bubbles. Figure 4.29 shows a comparison of bubble diameters at these two temperatures.

The sample was further heated to 650 °C and held at temperature for 20 minutes. Bubble growth and coalescence was observed throughout the implantation layer resulting in high concentration of *large* diameter bubbles near the implantation surface. Due to equipment failure, images from this heating step are not available.

The sample temperature was increased to 700°C and the bubble morphology underwent a rapid change increasing in both size and bubble density. Figure 4.30 shows the same region of the sample before and after this temperature increase. Obtaining a clear image of bubbles at this elevated temperature proved difficult as image drift was nontrivial and correcting for it in the short time before the bubble behavior changed was not feasible. As the boundaries of the bubbles are not well-focused and they are highly faceted, a size comparison of the bubbles in the two images is difficult. Prior to the temperature increase, subfigure (a), many of the bubbles have a long dimension in the range of $\sim$ 20 nm. Upon increasing the temperature the long dimension in several bubbles appears to increase to $\sim$ 30 nm. The fact that the bubbles grew in size also makes them more easily discernible. At 700 °C bubbles have appeared in regions where none were observed at 650 °C. Bubbles still appear highly faceted at this temperature and likely have a planar shape similar to those observed in the previously discussed samples.

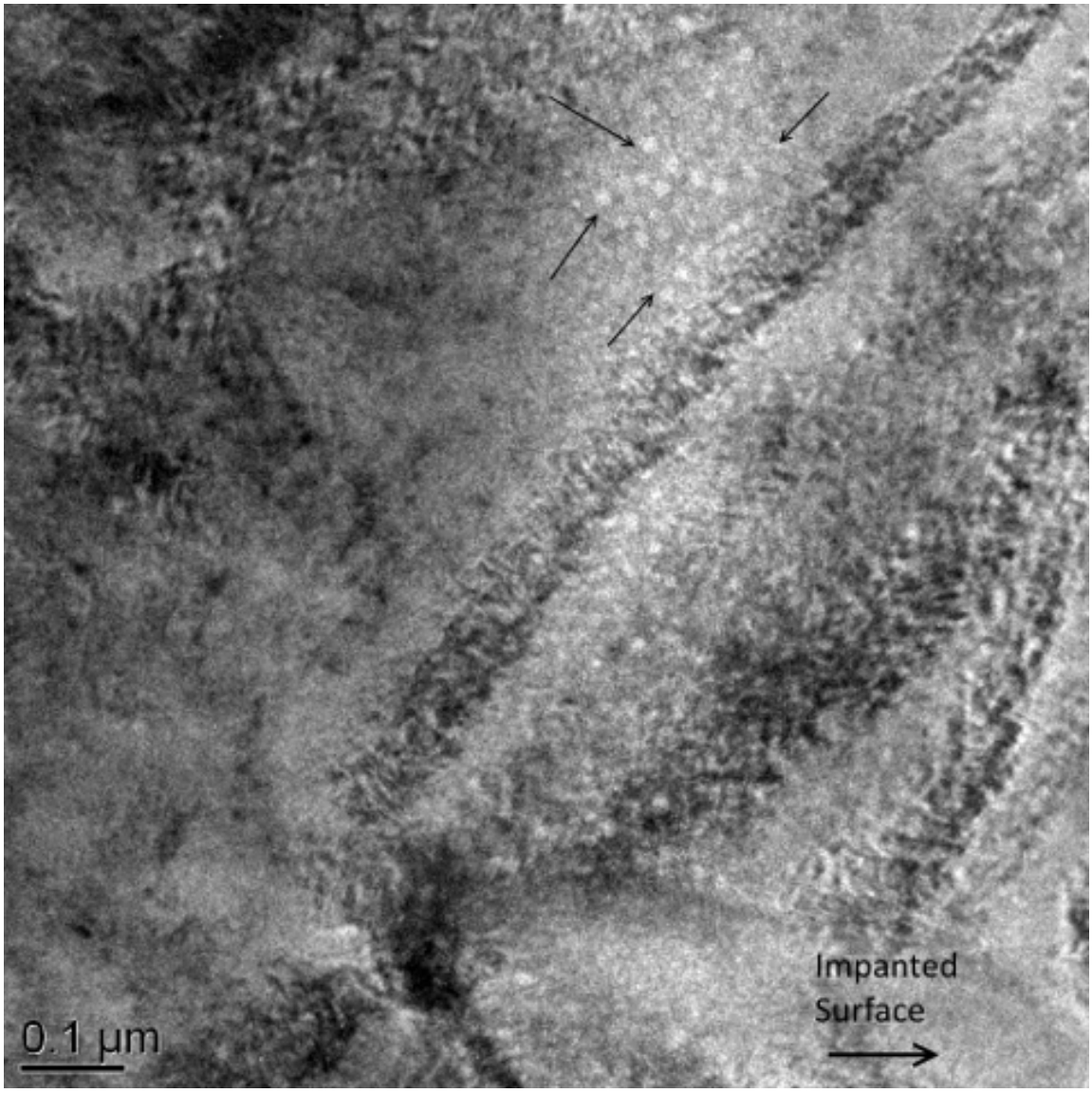

Fig. 4.27. Sample Zr4-2 at 450 °C. Large ($\sim$ 20 nm diameter) bubbles visible near a grain boundary in the highest dose region of the sample, marked by arrows. The direction of the implantation surface is to the right.

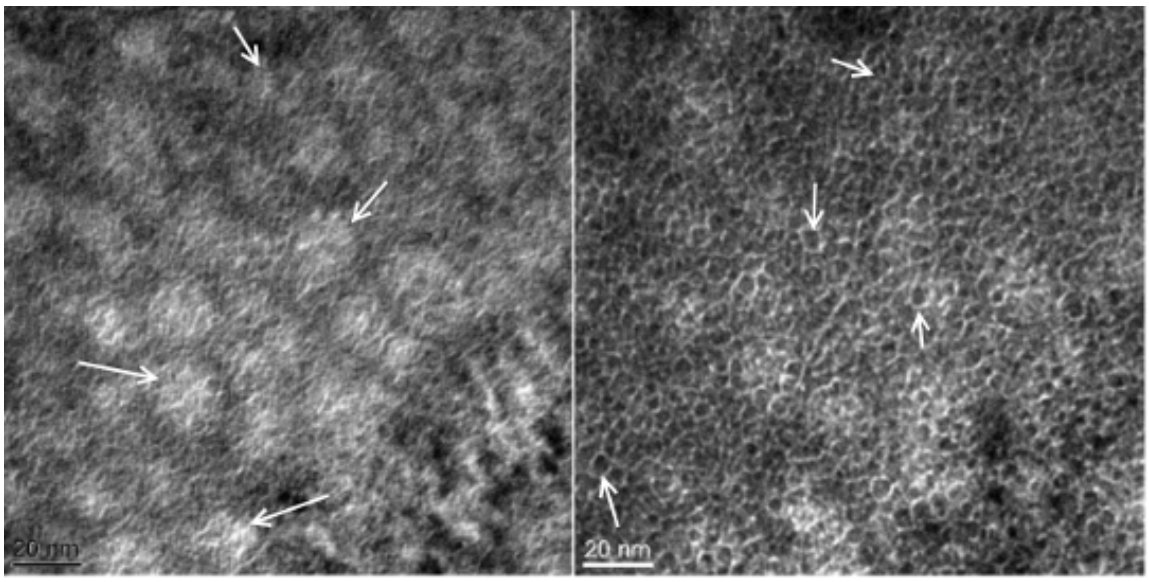

Fig. 4.28. Sample Zr4-2 at 550 °C. The left image is the focused condition showing the *large* bubbles (light contrast shapes marked by arrows). The right image is in the underfocused condition and shows the *small* bubble population as dark contrast shapes.

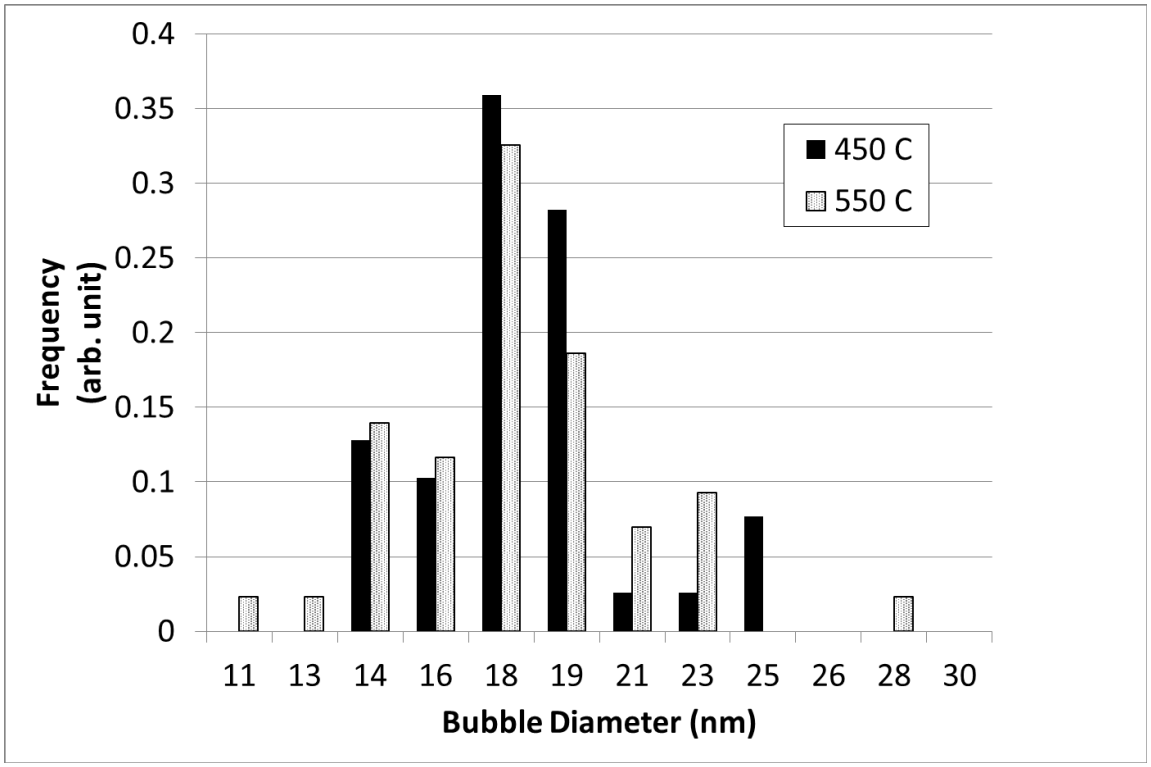

Fig. 4.29. Histogram of *large* bubble diameters in sample Zr4-2 at 450 and 550 °C.

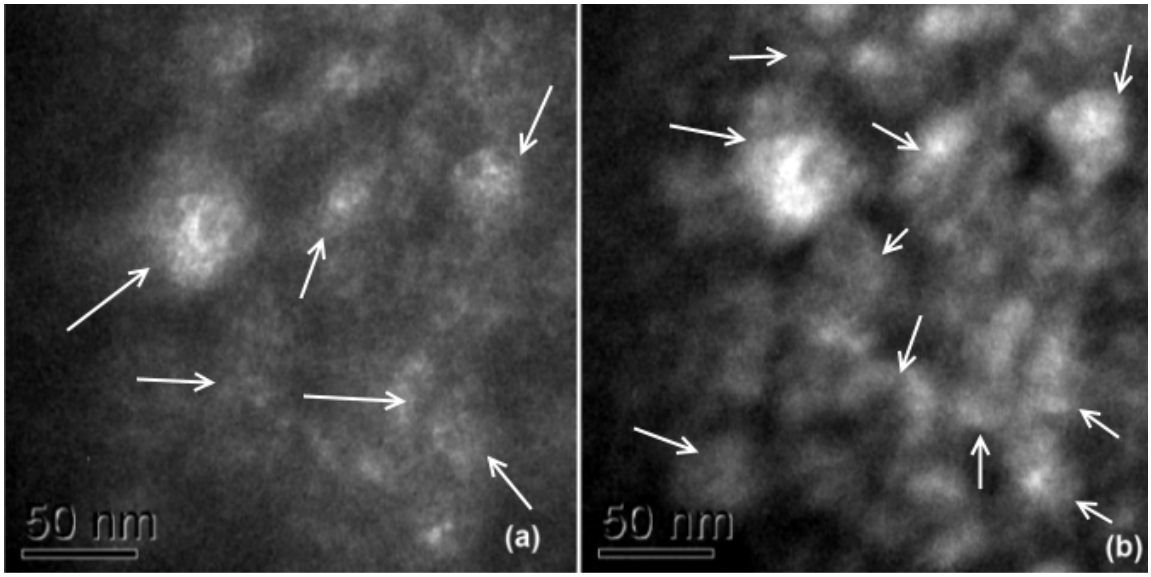

Fig. 4.30. Bubbles near the implanted surface of Zr4-2 after heating to 650 °C for 20 minutes (a); and immediately after increasing the sample temperature to 700 °C.

Figure 4.31 is a series of images (selected from digital video recording in the TEM) that show the migration and coalescence of several bubbles observed in figure 4.30(b). Migration of the smaller bubbles was observed $\sim$ 10 s after increasing the temperature and was completed after approximately 30 seconds. At this time, a few bubbles had grown to approximately 50 nm diameter. These images clearly suggest bubble migration and coalescence is active in the sample in the region near the implantation surface following a temperature increase.

The sample was then heated to 800 °C. Again, immediately after increasing the temperature bubbles grew and coalesced. An equipment failure resulted in a loss of the TEM images from this step and only post-heating images are available. Figure 4.32 shows the sample at room temperature after being heated to 800 °C for approximately 10 minutes. The bubble density is highest in the region of highest

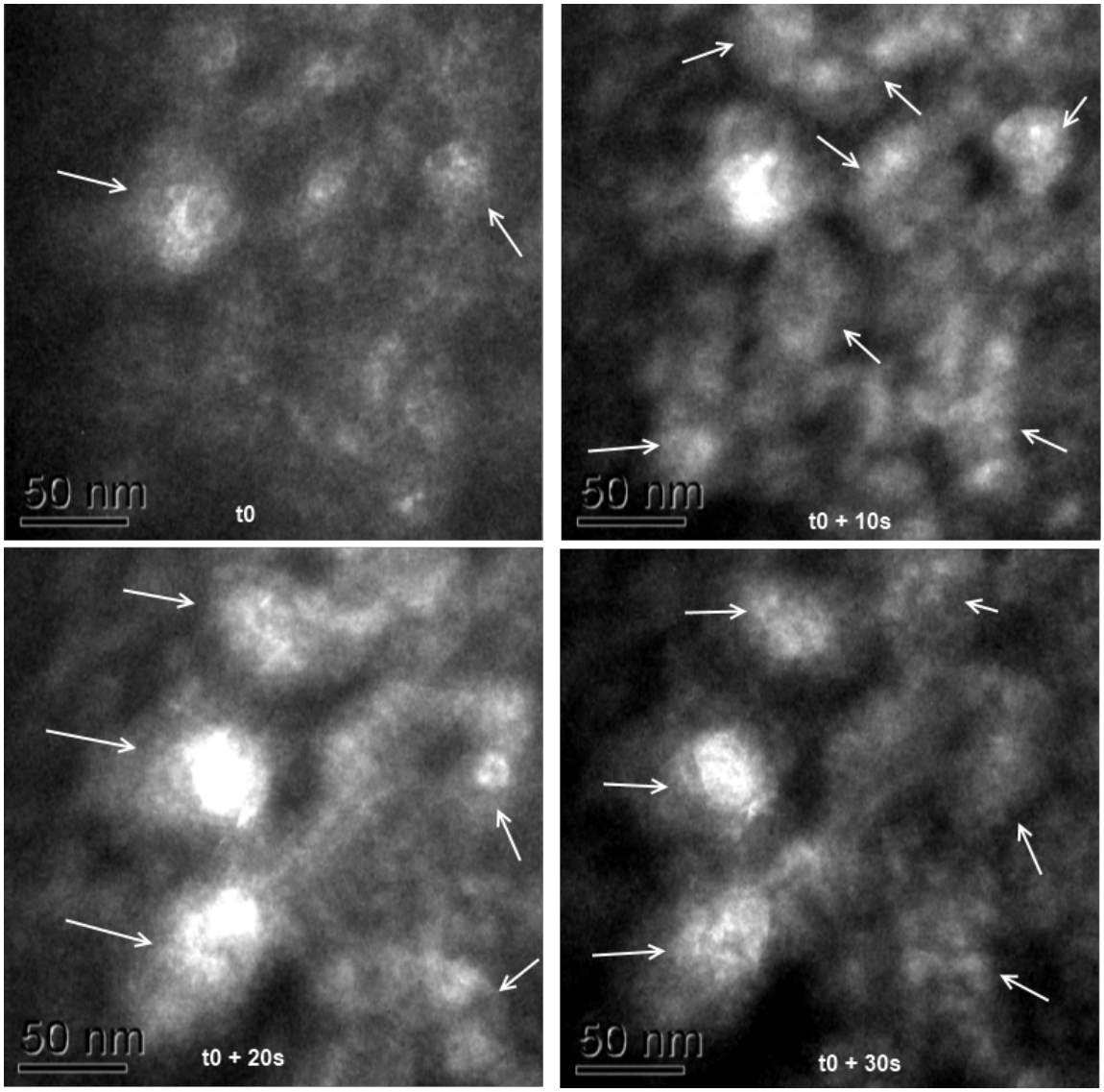

Fig. 4.31. Time lapse of bubble migration and coalescence in Zr4-2 after heating from 650 °C to 700 °C at t0. Arrows denote bubbles that are migrating and coalescing during the series of images. Extracted from digital video recording in the TEM.

dose though relatively large, faceted bubbles are visible throughout the implantation layer with diameters in the range of 50-100 nm .

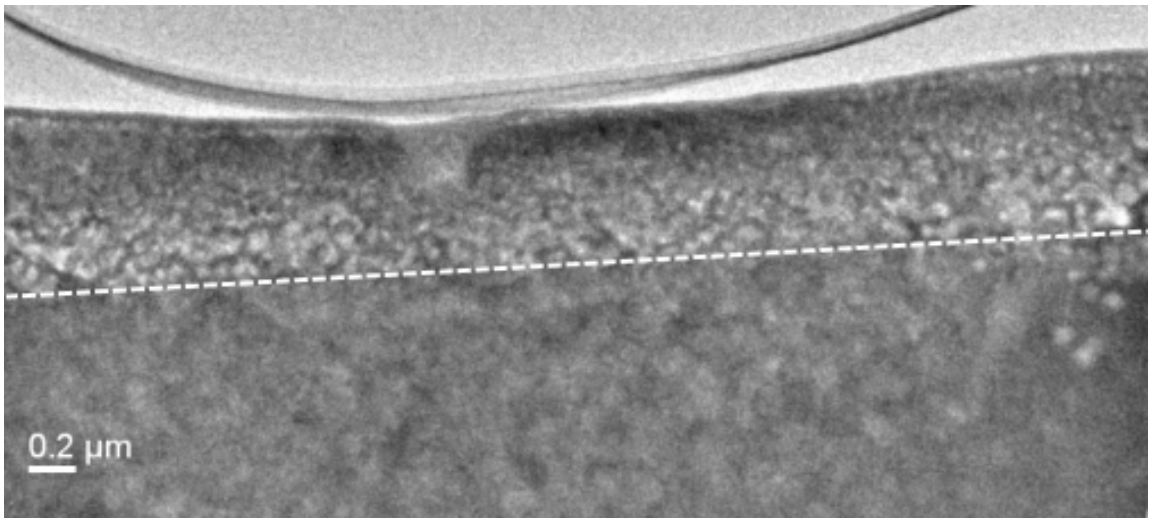

Fig. 4.32. Zr4-2 after heating to 800 °C and cooled to room temperature. A population of large diameter, faceted bubbles is visible throughout the implantaion layer (above the dashed line).

Three variants of zirconium were implanted with 140 keV He^+ ions to a fluence of 3×10^{17} cm^{-2} resulting in a peak helium concentration of $\sim$ 22 atom percent at a depth of 0.55 µm, with an average dpa of 9.5 in the high dose implantation region as estimated from the TRIM simulation predictions shown in Figure 5.1. The samples were prepared for XTEM investigation using a focused ion beam and observed in their as-implanted state as well as during *in situ* heating.

Sample preparation difficulties and equipment failures prohibited the acquisition of a consistent data set and the observations made in this work do not allow for the ability to make a systematic comparison of helium bubble characteristics among the three materials. For example, gallium contamination on some samples contributed to

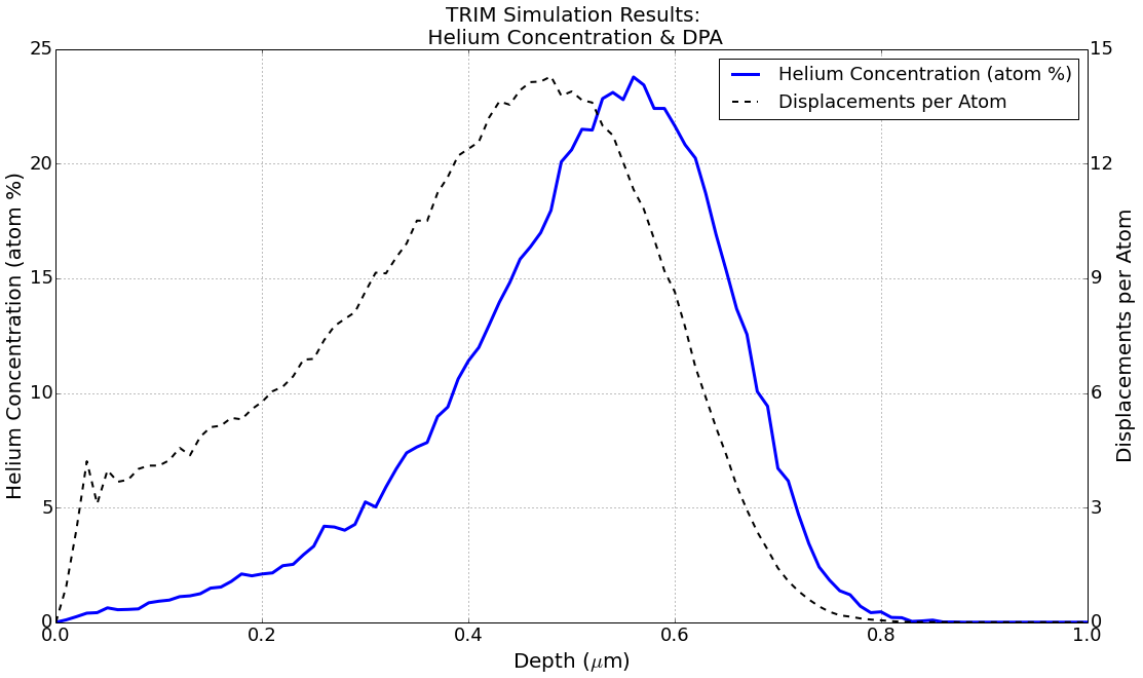

Fig. 5.1. Helium atom concentration and dpa as a function of implanted sample depth.

poor observation of bubble features and several samples were destroyed during sample thinning and/or removal of the residual Ga from the FIB preparation. Ultimately, a repeatable, usable sample preparation process was found but it was not possible to apply it to each alloy for each observation condition.

The observations made in this work provide insight into both the formation and behavior of helium bubbles in thin zirconium samples. This section presents a discussion of the notable features and behaviors of helium gas bubbles in zirconium metal characterized in this work.

Section 5.1 discusses the changes to the zirconium metal that occurred due to the high dose of helium, including an apparent stiffening of the matrix and possibly a change to the underlying crystal structure. Section 5.2 discusses the presence and characteristics of the high density bubble region that was observed in some samples and appears to form at a helium concentration above 10 atom percent. Section 5.3 discusses the proposed mechanism of thermal-vacancy assisted bubble formation and growth for the initial bubbles observed in this work during specimen annealing. Although this mechanism could account for the location of these initial bubbles, their apparent alignment, and the unique planar geometry they appear to have prior to migration and coalescence, further investigation is necessary to confirm their formation mechanism. This unique bubble geometry is compared to a spherical geometry from an energy of formation perspective in Section 5.4 where it is shown, via a simplified theory, that such planar geometry bubbles can be energetically favorable over more three-dimensional bubbles due to surface area energy reduction. It is proposed that this unique bubble geometry is merely a heretofore undescribed step in the formation of bubbles in TEM-thinned specimens. Section 5.5 discusses bubble response to temperature and although equipment failure led to a significant loss of data, it appears that both the maximum bubble size and bubble size distribution in zirconium follow similar behaviors as other metals in terms of their respective dependence on temperature and annealing time. Finally, Section 5.6 provides a brief

note on the occurrence of a multimodal bubble size distribution in samples that were aged at room temperature as bulk material (i.e., not yet thinned for TEM investigation).

5.1 Changes to the Zirconium Metal

The high quantity of helium implanted into the metals was chosen as it was expected to ensure the formation of bubbles for investigation. From the observations made of the as-implanted zirconium specimens it is evident that the high concentration of helium resulted in changes to the structure of the zirconium metal which manifest visually in low magnification TEM images and in the metal's strain response. These changes are due to either the concentration of helium in the metal or the formation of the high density region of small bubbles in the highest dose region of the sample. The observations and measurements made in this work are not sufficient to clearly identify how these two features contribute to the changes, and it is likely that they are closely related as the formation of the high density bubble region likely requires a high concentration of helium. As such, a discussion of the high density bubble region is presented in its own section below.

No bubbles or notable features were identified near the implantation surface in any of the specimens evaluated in the as-implanted state. This is somewhat expected as the room temperature implantation would have a comparably low thermal vacancy concentration which would suppress the formation of bubbles during irradiation, though the low concentration of helium and atomic displacements near the implanted surface would also contribute to the lack of helium bubbles in this region. Any helium atoms present in this region would likely reside in interstitial sites without significantly altering the zirconium matrix or having a high enough concentration to form bubbles.

Although no bubbles were noted near the implantation surface in any of the materials, a clear change in the metal was observed further beneath the implantation

surface. This region will be referred to as the high dose implantation layer to differentiate it from the region nearer to the implantation surface wherein no notable features were identified.

The first observation of a structural change in the metal was observed during FIB thinning of a Zircaloy-4 specimen (shown in Figure 3.4) wherein a dark line was present approximately 0.5-0.7 µm below the implantation layer. The STEM image of sample XTAL-1 (Figure 4.2) provides a more clear view of the high dose implantation layer in contrast to regions with lower helium concentration. The dark band in the figure begins at an implantation depth of about 0.3 µm and extends to a depth of approximately 0.7 µm. These depths are in good agreement with the TRIM predictions for a helium concentration of 5-10 atomic percent, shown in Figure 5.1.

The method by which sample Xtal-1 was mounted to its heating chip resulted in significant sample bending upon heating due to thermal expansion and a large amount of strain contrast was observed (shown in Figure 4.5). The bands of strain contrast became more pronounced as the specimen temperature was increased and appear to end at the bottom of the implantation layer. This suggests a reduction in the magnitude of sample strain (i.e. sample bending) at the high dose implantation region and is likely attributable to either a stiffening of the zirconium matrix (embrittlement) or a possibly a rearrangement of the crystal structure in the region.

As the implantation was performed at room temperature, the equilibrium vacancy concentration would likely have been insufficient to accommodate all of the implanted helium in the high dose implantation region without distorting the zirconium matrix [32]. Although a small number of freely migrating defects would be present from the incident helium ions, their concentration would be insufficient to accommodate all of the helium atoms. As such, a large portion of the helium atoms would occupy interstitial sites within the zirconium matrix. This high concentration of interstitial helium could significantly alter the behavior of the metal atoms. Helium embrittlement in metals is a well-known phenomenon and is likely responsible

for the stiffening observed in the XTAL-1 sample shown as a cessation in the bands of strain contrast. High helium atom concentrations have been shown to cause the hcp crystal structure to take on a random orientation or change to a more accommodating cubic structure in titanium [91]. In that work, Wan et al. measured the helium concentration required to cause titanium to transition from an hcp structure to a cubic one as 6%. For comparison, the high dose implantation region of the zirconium samples evaluated here corresponds to a helium concentration greater than 5% based on the depth of the region and the TRIM simulation results.

Due to the limited tilt capability of the heated sample stage holder in the TEM, it was not possible to identify a known atomic orientation within the samples. Figure 5.2 below shows three regions of the Zr4-2 sample and their respective fast Fourier transforms (FFTs). The regions investigated were the top of the sample near the implanted surface with low helium concentration, the high density small bubble region, and beneath the implantation layer beyond the predicted helium ion range. From the FFT insets it is clear that the material has a different dominant structure in each of the three regions. Near the implantation surface, there is some degree of order within the material but it does not appear to be hexagonal in nature. Within the high density small bubble region there is an ordered structure present (more clearly defined than near the implantation surface), which may be due to the bubbles. Beneath the implantation layer a hexagonally-aligned pattern is dominant.

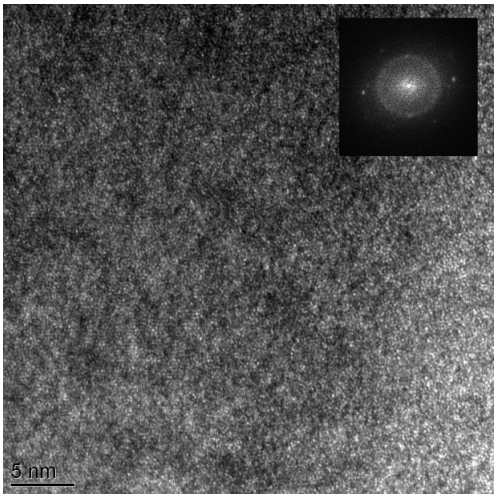

(a) Near the implanted surface.

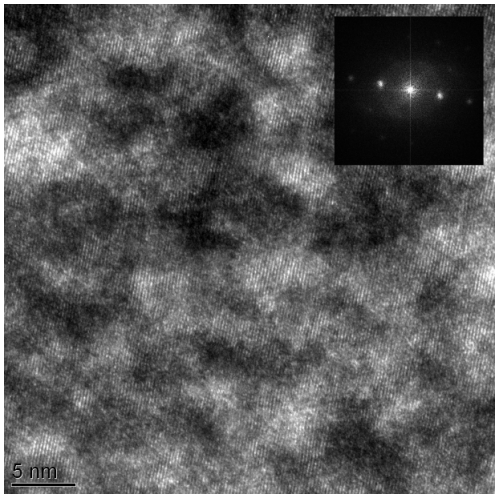

(b) High density bubble region.

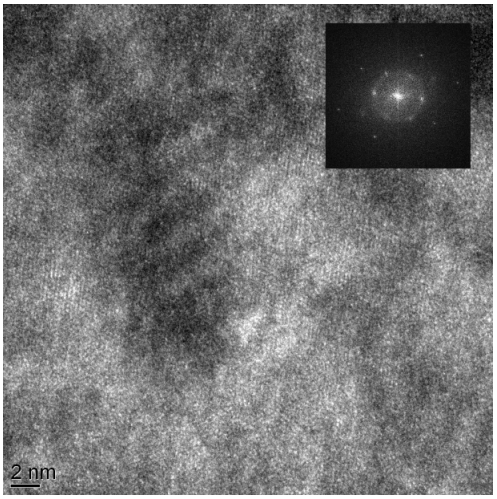

(c) Below the implantation layer.

Fig. 5.2. Three regions of sample Zr4-2 as-implanted with associated FFTs. The crystal structure of the implanted region could not be identified.

5.2 High Density Region of Small Bubbles

A high density region of small (∼4 nm) diameter bubbles was observed in the high dose implantation region of several specimens. The observations and measurements

made here suggest the bubble size distribution within this region is uniform across the depth of the sample and a helium concentration of greater than 10 atom percent is required to form it. It is possible that this region is similar to a bubble lattice which can form during inert gas implantations in metals at elevated temperature. Equipment limitations precluded identification of the basal plane within the samples and therefore investigation of any possible bubble alignment was not possible in this work. Krypton implantation in zirconium has shown the formation of a bubble lattice aligned with the basal plane of the metal [66].

It is expected that sample thickness and uniformity were key factors in the observation of this high density bubble structure and it is anticipated that each of the samples had such a structure present, regardless of whether they were prepared well enough for it to be observed. Evaluation of variation in the high density bubble region with respect to sample depth was measured for specimen HX-2 which allowed for observation across the depth of the region.

The high density bubble region of specimen HX-2, discussed in Section 4.4.3, was evaluated to determine if any variation existed within the region with respect to sample depth. As-implanted, no bubbles were visible within the top 0.4 µm of the sample, or below 0.7 µm, again, in good agreement with the TRIM results of peak helium at 0.5 µm. The high density bubble region was segregated into thirds to determine if the bubble morphology varied with depth from the implantation surface. This characterization corresponds to the small bubble population (∼4 nm diameter) (observed in Figure 4.17) and does not include the large bubbles observed in this specimen as those bubbles formed during sample aging under a different mechanism, discussed below. Figure 5.3 shows the relative bubble size density in the top (nearest the implanted surface), middle, and bottom third of the high density bubble region. The density of the small, 4 nm diameter, bubbles in this region was $\sim 5 \times 10^{17}$ cm^{-3}. No notable difference was observed in the size distribution or bubble density across the sample depth. Though the middle region shows a slightly higher density of

5 nm diameter bubbles, the difference is small enough as to be within the error of the measurement technique employed as each bubble was manually identified in the image analysis software. Similar results were obtained for sample Zr4-2 (refer to Figure 4.25) though a chart is not presented because the images were not suitable for accurate measurement of the entire depth of the region and the sample population was significantly lower than for the HX-2 specimen.

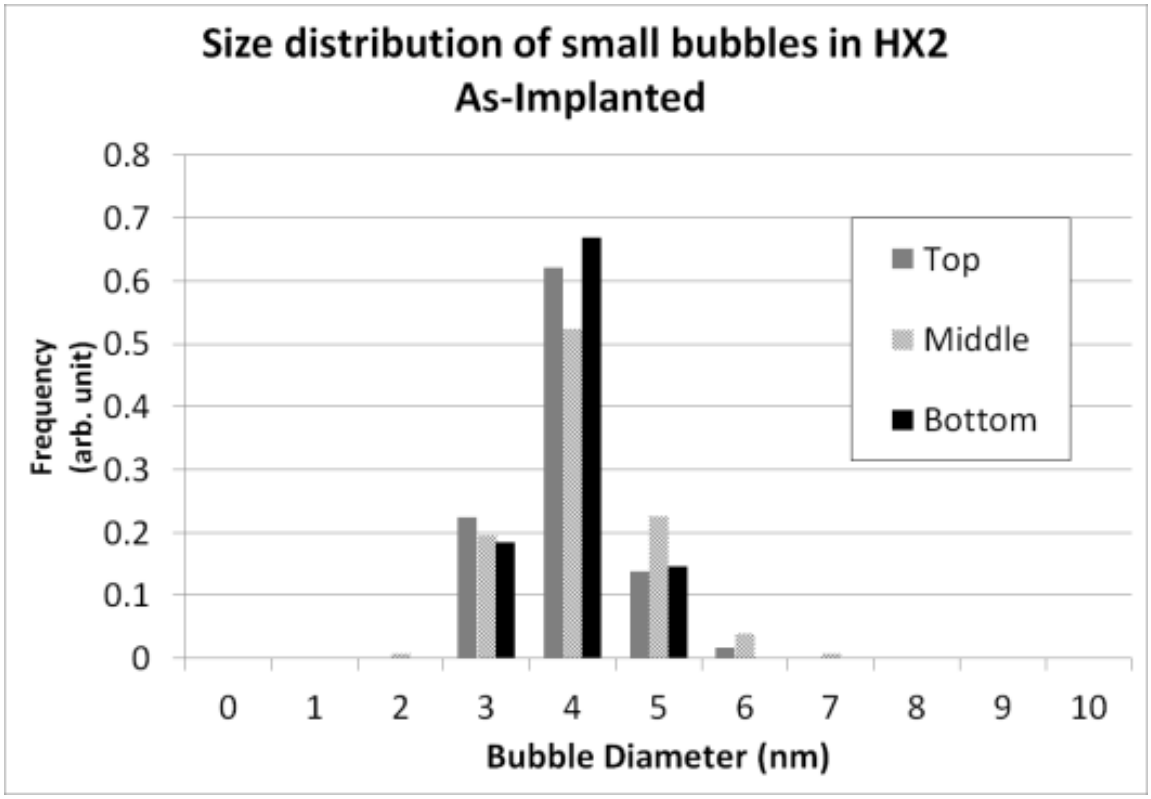

Fig. 5.3. Size distribution of bubbles in the as-implanted high density bubble region of sample HX-2, corresponding to image 4.17. *Top* refers to the segment of the region nearest to the implanted surface.

The structure of the high density bubble region is quite consistent across the sample depth as both the size and concentration of the bubbles remain constant until $\sim$ 60 nm of the bottom of the region. This is shown in the high magnification image

taken at the interface of the bottom of the implantation layer and the unimplanted region of sample HX-1, shown in figure 4.11. The bubble concentration decreases within a few tens of nanometers of the unimplanted region.

The thickness (i.e., depth) of the high density bubble region appeared consistent across the specimens in which it was visible at ∼0.3 µm. The mean bubble diameter was also consistent at 4-5 nm. This consistency suggests that the structure (i.e., bubble size and density) of the region does not closely depend on the impurities of the metal and may be more closely related to the total implanted helium concentration. The absence of any variation with respect to sample depth (on the order expected from the TRIM results) suggests that, beyond some threshold dose required to form the high density bubble region, additional helium causes the region to expand. Based on the TRIM simulation results, the helium concentration at the bottom of the implantation layer decreases from its maximum value to zero over a distance of ∼0.2 µm, in contrast to the observations made here of a few tens of nanometers.

Investigation of the threshold helium concentration required to form the high density bubble region could be of interest to the field of nano-porous materials manufacturing.

5.3 Possible Bubble Formation and Growth by Thermal Vacancy Absorption

In the TEM-thinned zirconium specimens evaluated here bubble formation at elevated temperature was first observed near the implantation surfaces at a temperature between 400 and 450 °C. These initial bubbles had highly irregular geometries and appeared planar in nature until sufficient coalescence occurred resulting in more three-dimensional but still highly faceted bubbles. The formation and growth of these initial bubbles is possibly due to an increase in both thermal-vacancy diffusivity and helium mobility in zirconium at these temperatures. Although conclusive evidence for this bubble formation mechanism is not presented here, the mechanism, if it is responsible, could account for the unique geometry of the bubbles, and the

location of their formation, in the region of lowest implanted helium concentration. The observations made here cannot preclude the formation of these bubbles due to surface effects during the ion implantation process or the presence of carbon in this region from the FIB sample preparation process. Though it is not evident how these other mechanisms could explain the alignment of the major axes of the planar bubbles.

None of the samples investigated showed observable change in bubble morphology at temperatures below 350 °C, and very limited changes after being held at 400 °C for over an hour. Sample XTAL-1 was held at 400 °C for approximately 2 hours after an hour of observations at lower temperatures and the bubbles observed were not easily identifiable until further heating led to their coalescence, which resulted in highly faceted bubbles that appeared planar in geometry. Figure 4.6 shows that 20-30 nm diameter bubbles formed quickly upon increasing the temperature to 450 °C. Similarly, bubble growth in the high dose region of sample Zr4-1 was observed at a temperature of 450 °C, though the residual gallium contamination and high sample thickness obscured the viewing of any bubbles that may have been present near the implanted surface.

In zirconium, 450 °C corresponds to a homologous temperature of 0.35 T_m, which is near the typically quoted transition from athermal to thermal bubble growth mechanisms of 0.3 T_m discussed in Section 2.1.2.

The series of images shown in figure 4.7 confirm that migration and coalescence of the irregular-shaped bubbles is occurring near the implanted surface. The TEM utilized did not have electron-energy loss measurement capability, thus it was not possible to obtain an accurate measurement of the helium concentration in these bubbles. As discussed below, it is expected that the irregularly shaped bubbles have a planar structure with major axis perpendicular to the image plane as no evidence of thin and bright bubbles appear in the images which would suggest the planar bubble was being viewed edge-on.

As the samples investigated in TEM are quite thin, the observations on bubble growth do not necessarily represent the behavior of helium bubbles in bulk materials, which is always the case with *in situ* TEM investigations. The influence of the high surface area to volume ratio of TEM-thinned samples cannot be ignored when evaluating such samples as the surface provides a continuous supply of vacancies to the metal, especially as temperature is increased. This work did not include an investigation of bulk samples and a direct comparison cannot be made for zirconium. However, a comparison of bulk and TEM-thinned samples of helium-implanted nickel showed a significant increase in mean bubble radius (by an order of magnitude) in the annealed TEM-thinned samples [74]. Similarly, Glam et al. observed helium bubble growth in implanted aluminum and found that bubble formation occurred in TEM-thinned samples at significantly lower temperatures than observed in bulk specimens [57].

Further evidence supporting vacancy-influenced growth in this work can be gained from evaluating the location where bubbles first appear. During the FIB thinning process used in this work, the implanted surface of the metals was nearest to the gallium ion cutting beam and was intentionally thinned the most compared to the rest of the sample (imagine a wedge-shaped specimen with the thinnest region at the implanted surface). Evidence of this is seen in figure 4.15 wherein much of the protective tungsten and carbon layers had been removed and some of the zirconium metal near the implanted surface was penetrated during thinning. In many of the samples investigated, bubble formation outside of the high density bubble region was first observed near the implanted surface, even though the concentration of helium in this region was much lower in the as-implanted state than the regions deeper within the sample.

It is considered unlikely that helium from deeper within the specimen migrated to the implantation surface during annealing as the only driving force for helium migration would be the concentration gradient as the temperature distribution would

be relatively consistent. The observation of bubble formation was independent of the annealing history, suggesting that migration of gas atoms from deeper within the specimen was not precursor to bubble formation near the implantation surface.

Another characteristic of the observed planar bubbles was that they appeared to be aligned with their major axis in the plane of the sample. Although the crystal structure alignment was not identified in the samples, it is unlikely that each specimen investigated was aligned in the same manner, though the majority of the bubbles appear flat with respect to the image plane. If the bubbles were aligned with a major axis normal to the image plane they would be expected to be brighter than the other bubbles in the population and little evidence of this was observed.

A mechanism of thermal vacancy assisted bubble formation and growth can account for several of the characteristics of the initially observed, planar bubbles. The region closes to the implantation surface was typically the thinnest region of the specimen and would be expected to respond to an increased vacancy flux from the free surfaces before the thicker regions. The seemingly planar geometry of the initial bubbles (prior to coalescence) and their alignment within the plane of the specimen can both be explained by a flux of vacancies arriving from the top and bottom free surface of the sample, resulting in a preference for bubble formation perpendicular to the fluxes.

It is easy to envision a region of the TEM sample wherein the vacancy flux from the top and bottom sample surfaces are equal in magnitude and opposite in direction. In such a region, a cavity of helium atoms would not experience preferential growth toward either the top or bottom surface, rather they would form a platelet, normal to the two vacancy fluxes. By contrast, if the vacancy flux from one surface was significantly higher or lower than the other, the cluster of helium atoms would form a cavity that would grow preferentially towards the stronger flux.

This thermal vacancy assisted bubble formation mechanism cannot completely account for the similarities in bubble formation temperature observed in this work

as helium mobility is known to increase in zirconium at a similar temperature. A comparison with bubble formation in other TEM-thinned metals does suggest a notable similarity between the increase in vacancy diffusivity however.

The increase in vacancy diffusivity from room temperature to the temperature at which bubbles are observed to form, T_b, is compared for the observations presented here and the work reported by Glam et al. for aluminum [57]. The activation energies for vacancy diffusion, E_A^v, in zirconium and aluminum are 0.93 eV [92] and 1.44 eV [93], respectively. A comparison of $\frac{D_v(T_b)}{D_v(RT)}$ of the two materials is shown in table 5.1.

Table 5.1
Comparison of increase in vacancy diffusion diffusivity at temperatures for reported bubble growth, T_b, in TEM-thinned specimens.

Material	T_b(K)	$\frac{D_v(T_b)}{D_v(RT)}$
Zr	723	5×10^{10}
Al	473	17×10^{10}
	460	6×10^{10}

The ratios obtained for the reported temperatures of the onset of bubble growth are in relatively close agreement. However, if the value reported by Glam was over-estimated by as little as 3% they are in excellent order of magnitude agreement, shown as 460 K in the table. This suggests that a thermal-vacancy assisted bubble formation mechanism could be occurring in the *in situ* TEM conditions evaluated. Differences in sample preparation methods and experimental conditions between the work performed here and reported by Glam must also be considered. For example, it is quite likely that the electron beam conditions utilized in the work presented by Glam had an impact on the bubble behavior as several larger bubbles were observed to split and reform, indicating beam-bubble interactions. Similarly, the vacancy diffusion activation energy utilized in this analysis assumes pure metals and may need

to be corrected due to the presence of the inert gas and impurity concentrations. This comparison also ignores the mobility of helium atoms within the materials, which at least for zirconium, becomes highly mobile at a temperature of $\sim$ 430 °C [29].

Although further investigation is needed to confirm the thermal-vacancy formation mechanism is active and/or dominant, it is considered the only mechanism that reasonably accounts for the observations in this work regarding the location of first bubble formation, the unique planar shape of the initial bubbles, and the consistency of the temperature of bubble onset.

Of special note, the extruded zirconium material did not show signs of bubble growth when heated to 450 °C, as was observed in the other two metals. The onset temperature for bubble growth was never observed in this material though bubbles were visible in sample HX-2 at a temperature of 600 °C. It is possible that the high oxygen concentration resulting from the powder metallurgical fabrication process of the extruded zirconium material played a role in the delayed onset of bubble growth as it is known that impurity concentrations in zirconium can impact the behavior of point defects within the metal and oxygen specifically is known to retard helium mobility [81].

5.4 Formation of Planar Bubble Structures

It is necessary to address the faceted, platelet-like geometry observed in the bubbles near the implanted surface of the samples (refer to Figure 4.7) and whether they are indeed helium-filled cavities or some other structure or artifact. Evidence of the migration and coalescence of these faceted and irregular-shaped bubbles into more regular (i.e. three-dimensional) bubbles is provided in the series of images shown in Figure 4.7 as the small highly faceted bubbles coalesce into structures with more depth. Measurement of the depth (with respect to the electron beam) or helium concentration of these planar-shaped bubbles was not possible during this work.

Though it is possible that the features identified as faceted bubbles are an artifact of the TEM imaging system or some other phenomenon in the metal, their overall behavior of migration and coalescence, observed in the time-series images shown in Figure 4.7 and to a lesser extent Figure 4.31, suggest that they are indeed helium-filled cavities, perhaps being viewed in an early stage of bubble development between nucleation and a more expected three-dimensional geometry.

Although not specifically addressed in reports, evidence of similarly irregular-shaped bubble structures has been presented. Glam et al. observed similar irregular-shapedbubbles in helium implanted aluminum samples investigated with *in situ* annealing in a TEM [57]. In their work, the small faceted bubbles appear in a high density of overlapping bubbles, similar to the observations made here. As the small bubbles coalesced and grew in size, they took on a more regular bubble structure, that is, more curved and spherical.Similar irregular shaped structures have also been observed in helium-implanted titanium thin films by Sun, though they were not directly discussed by the author [94]. It is possible that the *open* nature of the zirconium lattice, i.e., large interatomic spacing and relatively small ion core, allows for the formation of these irregular-shaped cavities under certain conditions. Wan, et al. investigated the impact of helium atoms on the crystal structure of titanium, also an open metal, and found that a large amount of helium could be accommodated within the matrix prior to a rearrangement of the titanium atoms [91].

A simple theoretical treatment is provided here to determine whether such planar-bubbles can exist. The following discussion is based on the theory of bubble energetics and formation kinetics presented by Trinkaus [35] and modified as appropriate to suit the conditions in this work. It is noted that a more rigorous theoretical treatment of the process would include the impact of zirconium's unique anisotropic properties, for example Young's modulus.

In order for such a planar-bubble to exist, its formation energy, F_{pb}, would have to be less than or equal to the formation energy of a three-dimensional bubble, F_B,

assuming a spherical bubble for this derivation as it has the lowest surface energy. Defining the bubble formation energy, F, as [35]:

$$F = F_S + F_D + F_{Me-He^n} \tag{5.1}$$

where F_S is the surface energy, F_D is the matrix distortion energy required to accommodate the bubble, and F_{Me-He^n} is the helium-metal interaction energy. Requiring the formation energy of the planar-bubble, F_{pb}, to be less than the formation energy of the spherical bubble, F_B, gives:

$$\Delta F = F_{pb} - F_B \leq 0 \tag{5.2}$$

The three terms in equation 5.1 will be discussed separately, beginning with the surface energy. The surface energy term is defined with the surface free energy of the metal, γ, and the surface area of the structure, S:

$$F_S = \gamma \cdot S$$

Defining the surface energy of the planar-bubble as:

$$F_S^{pb} = \gamma \cdot S^{pb} = \gamma \cdot 2A^{pb} \tag{5.3}$$

where A^{pb} is the observed area of the planar-bubble from the TEM observations. This definition ignores the height of the planar-bubble, thereby assuming its contribution is negligible in terms of the major and minor axis of the planar-bubble (i.e., the observable dimensions in the TEM). The surface energy term for the spherical bubble, with radius r_B, is:

$$F_S^B = \gamma \cdot S^B = \gamma \cdot 4\pi r_B^2 \tag{5.4}$$

The matrix distortion energy accounts for the energy required to elastically distort the zirconium matrix to accommodate the helium-filled cavity. This term can

be considered as the distortion of the zirconium atoms immediately surrounding the bubble compared to their position if the bubble were a cavity rather than helium-filled. For the planar-bubble this distortion energy depends on whether the helium atoms have caused elastic distortion in the matrix. As the proposed bubble formation mechanism for the planar-bubbles is thermal-vacancy flux driven, it is assumed that no atomic displacements exist around the planar-bubble. The zirconium atoms surrounding the planar bubble are only allowed to be compressed or relaxed relative to the next layer of zirconium atoms such that their interplanar spacing is somewhat shorter or longer than in the unperturbed crystal structure. The matrix distortion energy, F_D^{pb}, is defined as the elastic energy of the matrix based on linear isotropic continuum theory which must be positive, and is a very small term compared to the surface energy (see section 2.1.3 and [35]. As such, the matrix distortion energy is assumed to be negligible compared to the other terms.

$$F_D^{pb} = F_{el} = \frac{2}{3}\mu\Delta V/V_o \approx 0 \tag{5.5}$$

For the case of the three-dimensional bubble the matrix distortion term is replaced by the matrix relaxation energy term utilized by Trinkaus, F_{rel}^B [35]. Trinkaus provides a derivation of this term and concludes that for bubbles near thermal equilibrium it is *small*, though it can reduce the formation energy for highly overpressurized bubbles. In the region where the planar-bubbles were observed, no evidence of highly overpressurized bubbles exists. For the treatment provided here, the value of the relaxation energy is again neglected, due to its small magnitude.

$$F_{rel}^B = -\frac{3}{8}\frac{V}{\mu}(p - 2\gamma/r)^2 \approx 0 \tag{5.6}$$

The final term in equation 5.1 is the metal-helium interaction energy. This term accounts for the helium bulk free energy, helium-helium interaction energy, and helium-metal interaction energy. In order for these terms to impact equation 5.2, there must be a difference in them between the platelet-bubble and spherical

one. Here it is assumed that the number of helium atoms in the bubbles as well as their temperature and pressure are equal. This results in the helium bulk free energy term, the energy required to put the helium atoms into the arrangement, being equal for each bubble. The geometry of the bubbles could result in a difference in the helium-helium interaction energies as the number of nearest-neighbor helium atoms would likely differ between the structures, however any such difference would be negligible compared to the contribution from the total number of helium atoms [35]. The helium-metal interaction energy is primarily a function of the area available for helium-metal interactions in the structure, S. With these assumptions regarding the number and state of the helium atoms the difference in this term would be:

$$\Delta F_{Me-He^n} = \gamma \cdot \left(S^{pb} - S^{B}\right) \tag{5.7}$$

Evaluating equation 5.2 with these terms results in:

$$\Delta F = \left(\gamma S^{pb} - \gamma S^{B}\right) + \left(\gamma S^{pb} - \gamma S^{B}\right) \leq 0 \tag{5.8}$$

which, upon simplification, yields:

$$\Delta F = \left(S^{p} - S^{b}\right) \leq 0 \tag{5.9}$$

Based on these assumptions, the criteria for a helium bubble to exist in a planar geometry rather than a spherical bubble can be written as:

$$2\gamma A^{pb} \leq 4\pi\gamma r_B^2 \tag{5.10}$$

or:

$$A^{pb} \leq 2\pi r_B^2 \tag{5.11}$$

which results in the condition that if the measured (i.e. observed) area of the planar-bubble is less than twice the measured area of the spherical bubble, the planar bubble

will have a lower formation energy.A plot of the planar bubble observed area criterion versus spherical bubble radius (equation 5.11) is shown in figure 5.4.

From equation 5.11, for a spherical bubble with a radius of 25 nm, a planar bubble with the same number of helium atoms at the same temperature and pressure would have a lower formation energy if its observed area were less than ~ 3900 nm^2.

For comparison, the derivation of the bubble formation energy provided by Trinkaus defines all terms as a function of bubble geometry and helium bulk free energy [35]. As the assumptions made here result in the bulk free energy of the two bubbles being equal, it is expected that the final form of equation 5.2 would only contain geometric terms and similar to the analysis of the coalescence process provided in section 2.1.3, reduction in surface energy is the driving force for the bubble's shape.

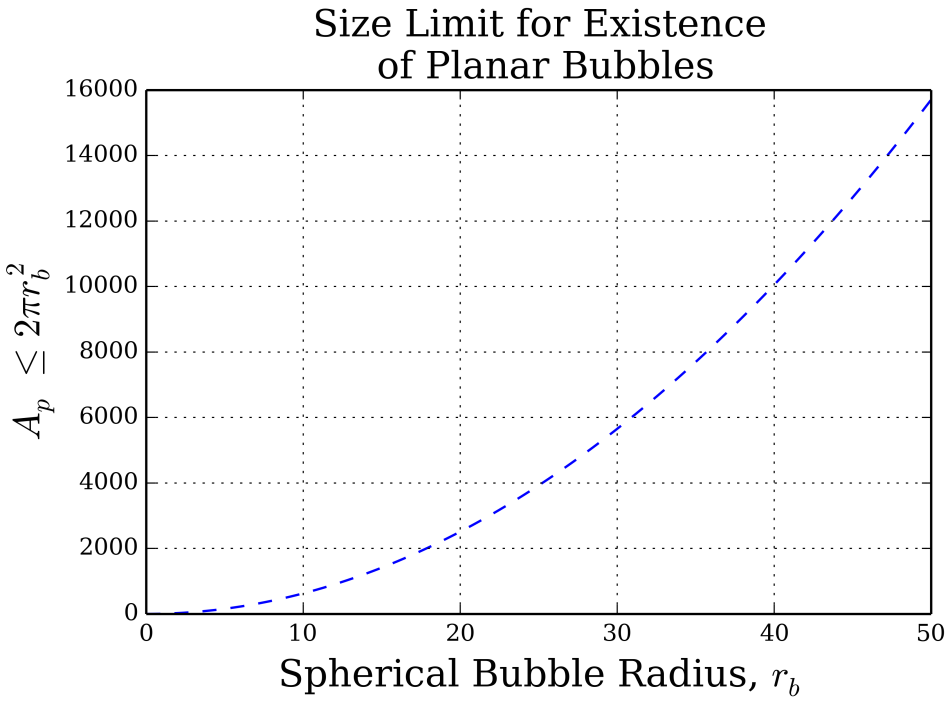

Fig. 5.4. Plot of $2\pi r_b^2$ versus r_b in nm. The measured area of the planar-bubble, A_{pb} must be less than or equal to $2\pi r_B^2$, where r_B is the radius of a spherical bubble.

Although it is difficult to isolate any individual bubbles from a single image in the series in Figure fig:xtal1-series, an estimate of the size of some of the planar-bubbles shown in Region X of the figure was made with the Fiji image analysis software [90] shown in Figure 5.5 below. Three planar-bubbles are highlighted in the below figure and their measured areas vary from 3500 to 6500 nm^2. Based on the formulation presented here, these planar geometries are energetically favorable compared to a spherical bubble with a radius in the range of 23 to 32 nm.

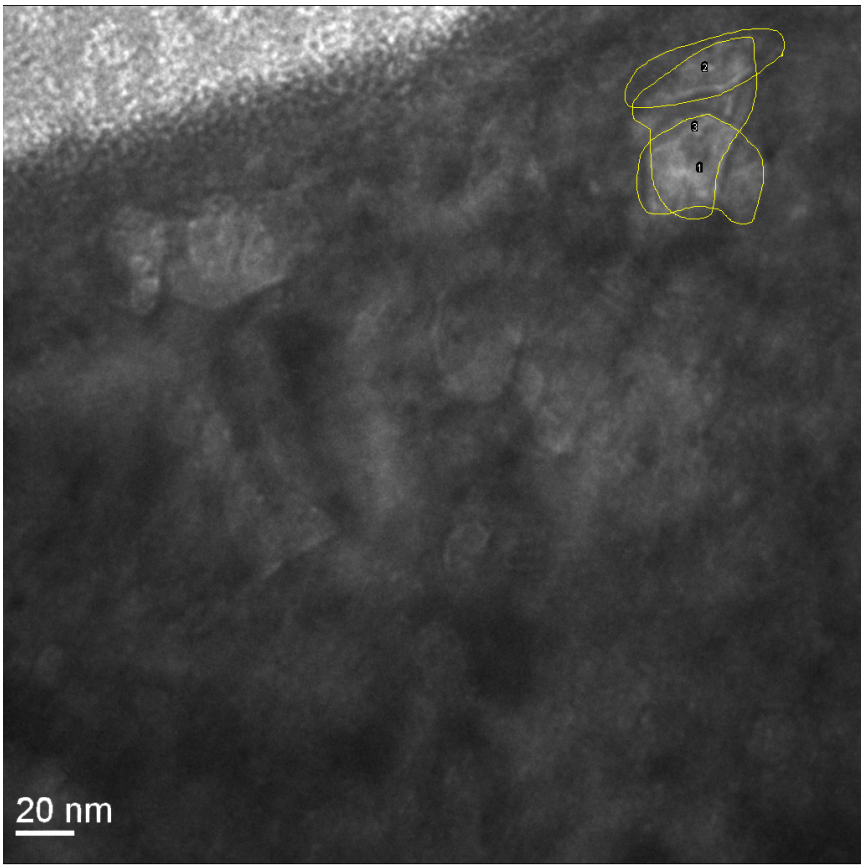

Fig. 5.5. Select planar-bubbles from sample XTAL-1 prior to coalescing into a more three dimensional structure. Refer to the series of images in Figure 4.7.

5.5 Bubble Response to Temperature

Based on the limited data available, it appears that helium bubbles in zirconium metal respond to changes in temperature similarly to other metals in that the maximum bubble size is strongly dependent on temperature, T_a, while the bubble size distribution is dependent on annealing time, t_a. The images below (Figures 5.6, 5.7, and 5.8 provide a comparison of the as-implanted state and the post-annealing state from one sample of each material evaluated and are provided as low-magnification, unedited images for comparative purposes. The annotated versions of each image as well as a description of the annealing history are included in the body of the work as referred to in the captions.

In the specimens observed, the size of the bubbles quickly increased as the temperature was increased and prolonged time at the increased temperature did not result in a noticeable change in maximum bubble size. Coarsening of the bubble population progressed with time, but the maximum bubble size remained relatively constant. The series of images of sample HX-2 being heated from 650 to 700 °C show this well in Figure 4.20 as do the images of sample XTAL-1 reported in Section 4.3.2. Similar dependence of bubble size on T_a and t_a have been observed in copper [74].

Unfortunately, equipment failure at the ORNL facility led to a loss of much of the data that would have enabled a quantitative analysis of bubble size distribution and concentration as a function of annealing time in the zirconium metals characterized. The observations of sample Zr4-2 (refer to Figure 4.31)show the first 30 seconds after increasing the temperature from 650 °C to 700 °C and although a rapid response in bubble migration and growth is observed, this time frame is too short to compare to other works which suggest that in aluminum, at these temperatures, mean bubble size stabilizes after annealing for 10^1-10^2 hours [57]. Similarly, only the first 15 minutes after increasing the temperature from 650 °C to 700 °C are available from sample HX-2 (refer to Figure 4.20), though a similar result is observed.

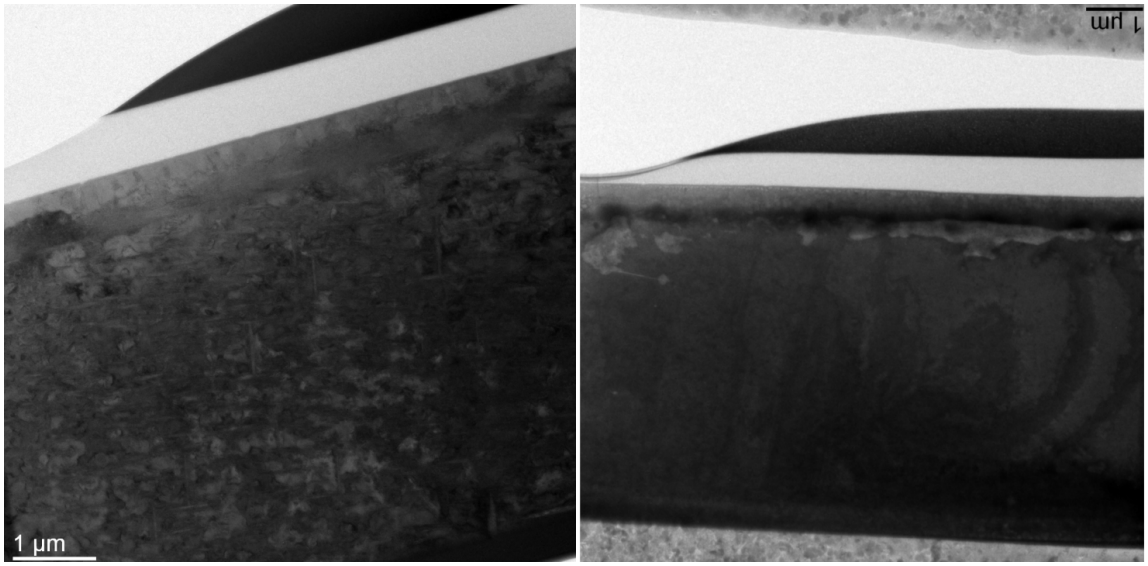

Fig. 5.6. Sample XTAL-1 as-implanted (left) and after heating to 450 °C (right). This sample is discussed in Section 4.3.1 of the report.

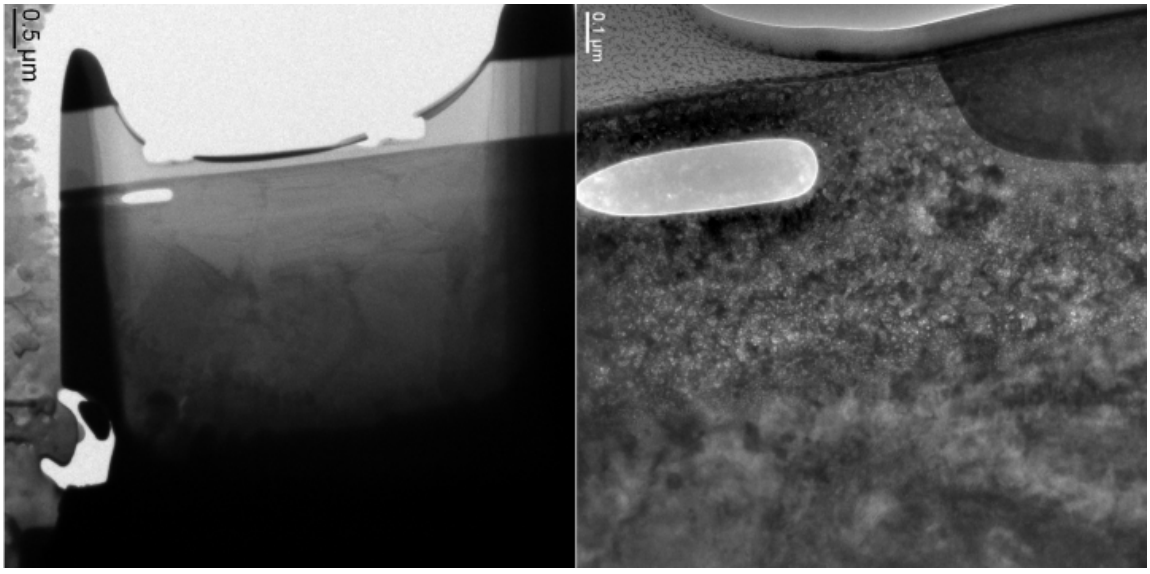

Fig. 5.7. Sample HX-2 as-implanted (left) and after heating to 700 °C (right). This sample is discussed in Section 4.4.3 of the report.

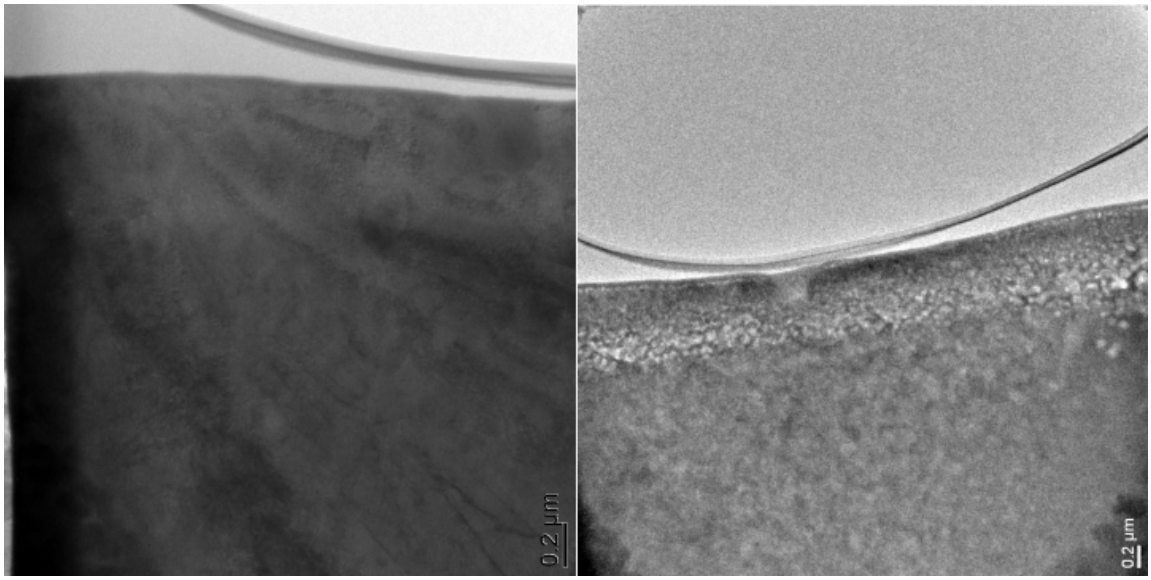

Fig. 5.8. Sample Zr4-2 as-implanted (left) and after heating to 800 °C (right). This sample is discussed in Section 4.5.3 of the report.

From the available data, the mean bubble radius, $\bar{r}_b$, as a function of temperature is plotted in Figure 5.9. The data is a combination of measurements from all samples where bubble size analysis was available. Several regions of each sample were chosen and the bubble sizes were determined with image analysis software by manual identification of the bubble boundaries. The conditions under which the data were recorded are not consistent, as the images used for temperatures above 650 °C were taken at room temperature after the sample had cooled. As discussed in section 2.1.4, in order to determine controlling bubble growth mechanism, the bubble size with respect to helium concentration as a function of annealing temperature would be required, as discussed in Section 2.1.4. As such, no determination can be made from the data presented in figure 5.9.

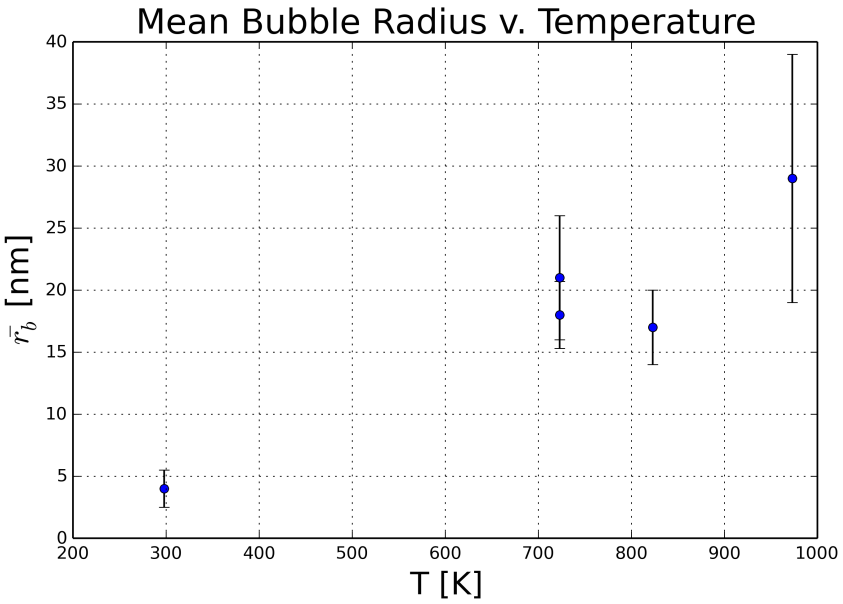

Fig. 5.9. Mean bubble radius versus temperature for the samples observed. The error bars are the standard deviation of the bubble populations measured. Note, the time at temperature differs for each sample.

It is clear that, under the conditions observed at the onset of bubble formation (i.e. around 450 °C) migration and coalescence of the planar-bubbles is occurring. However, the data required to evaluate the growth mechanisms at higher temperatures and longer time scales is not available. A similar ivestigation could be carried out to determine which bubble growth mechanism is dominant under different conditions in zirconium though the influence of thermal vacancy-assisted bubble growth in TEM-thinned samples cannot be excluded and would certainly result in a different behavior than what would occur in bulk material.

5.6 Multi-Modal Bubble Size Distribution

The as-implanted bubble structure of sample HX-2 showed a multi-modal size distribution in the high dose implantation region (figure 4.16 is repeated below). A similar bubble size distribution was noted in sample Zr4-2 though it was not as easily distinguished in the image. These samples were aged for approximately 9 months at room temperature compared to the HX-1 and ZR4-1 samples. Multi-modal size distributions have been attributed to Ostwald ripening [95] which, as an athermal process, could be expected to be dominant in the conditions experienced by the material. In the room temperature conditions the samples were stored at, bubble migration and coalescence would be limited, and the samples were stored as bulk material so the influence of surface vacancies would not have been large. The larger bubbles had a mean diameter of $\sim$ 16 nm while the small bubble population maintained its mean diameter of 4 nm, similar to the other samples. The larger bubbles appear to be concentrated in the middle of the high dose region, consistent with a helium concentration of $\sim$ 20 atom percent based on the TRIM simulation results. These larger bubbles also had a much more rounded shape, some of them appearing nearly circular compared to the bubbles formed during annealing and those comprising the high density bubble region, also suggesting a different formation mechanism.

Little data is available about the change of these larger bubbles with temperature as few changes were observed until temperatures of $\sim$ 700 °C whereupon their population grew rapidly, as shown in the series of images in Figure 4.20. Unfortunately, the majority of the data from the high temperature observations was lost due to equipment failure and no notable observations are provided here. It would be interesting to measure the concentration of the small bubble population and compare it to the earlier specimens that lack the large bubble population in an effort to determine if helium from the high density bubble region contributed to the formation of the large bubbles or helium that resided outside of those small bubbles in the high density bubble region, within the zirconium matrix. However, the images obtained aren't suitable for measurement of the concentration of bubbles in the high density bubble region.

Any immediate importance to this phenomenon is unclear at this time as no known applications of zirconium would involve such a high helium concentration present in the material for a length of time required to form these larger bubbles. However, the field of nanoporous materials is relatively nascent and there may be relevant observations from this finding for the manufacture of such materials, especially in terms of time limitations for storing metals after implantation.

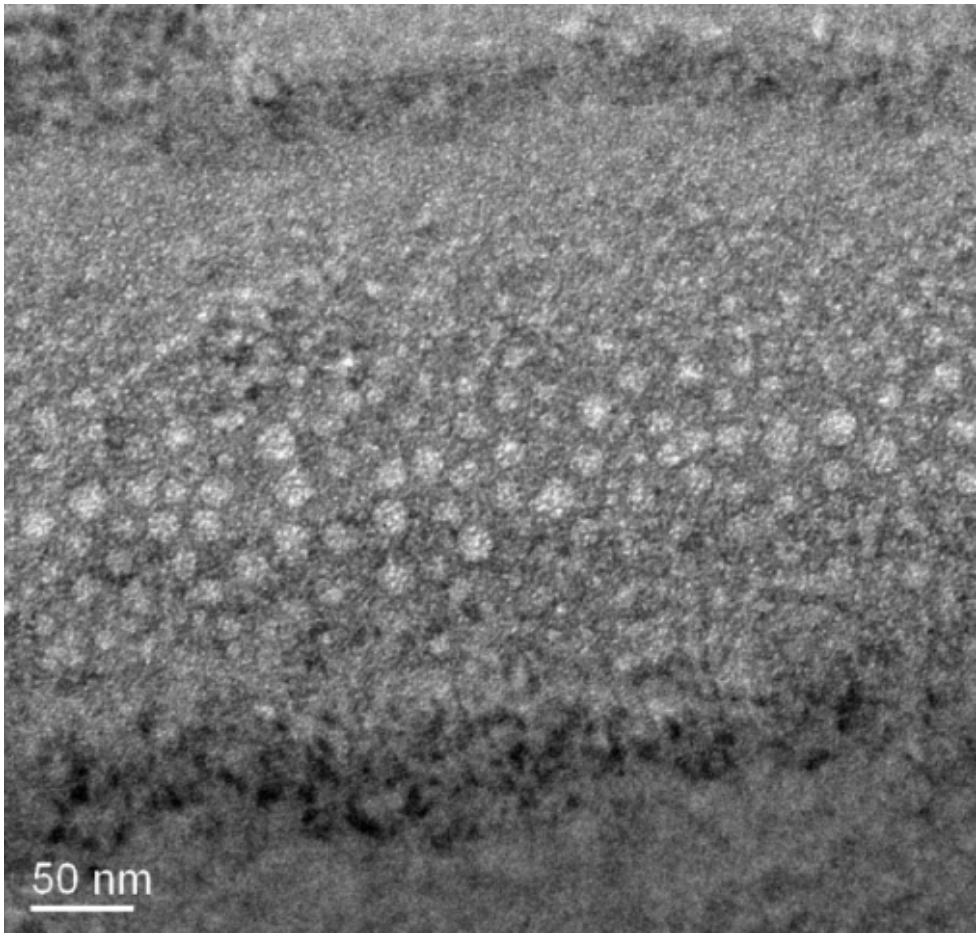

Fig. 5.10. Figure 4.16 repeated. Region of highest implantation dose in HX-2 in the focused condition at room temperature showing relatively large diameter, >10 nm, bubbles. Figure 4.17 shows the same region in the overfocus condition.

6. SUMMARY AND CONCLUSIONS

An investigation into the formation and growth of helium bubbles in zirconium metal was performed utilizing the three zirconium materials described in Table 6.1 below. The materials were selected to provide a variety of both impurity concentration and forming process, as discussed in Section 3.1.

Table 6.1
Zirconium materials investigated in this work with impurity concentration in ppm by weight.

Material	Label	C	Cr	Fe	Hf	N	Ni	O	Sn
Zircaloy-4	Zr4	60	1150	2140	67	25	<35	720	15700
Extruded	HX	300	<50	135	175	770	<35	3500	<25
Crystal bar	XTAL	20	<50	<50	165	<20	<35	60	<25

Each of the materials underwent 140 keV He^+ ion implantation to a fluence of $3 \times 10^{17} cm^{-2}$ and was prepared via focused ion beam for cross-section TEM observation with *in situ* heating as described in Section 3.3 of this document. The high helium concentration used in this work was chosen as it was expected to guarantee the formation of bubbles.

Evaluation of the as-implanted metals revealed a structural change had occurred in the metal at a depth that was in excellent agreement with the TRIM simulation predictions for high atomic displacement and high helium dose. This high dose implantation region was visible with low magnification in some samples and, upon closer inspection, contained a high density of small (∼4 nm diameter) bubbles. Within this region, the bubble concentration was measured to be $\sim 5 \times 10^{17}$ $cm^{-3}$and the bubble population and size was consistent. Some evidence of short-range bubble ordering was observed in the region but no observations of the long-range ordering associated

with so-called bubble lattices was observed. The underlying metal crystal structure was modified within this region of high density bubbles compared to the unimplanted metal though the degree of modification was not quantifiable under the conditions evaluated. The observations and measurements made here suggest a helium concentration greater than 10 atom percent is required to form this high density region of small bubbles.

Samples were heated in the TEM to various temperatures and times in an effort to capture the onset of bubble formation outside of the lattice region. Bubble formation was observed in both the crystal bar (XTAL) and Zircaloy-4 (Zr4) materials at a temperature between 400-450°C regardless of the previous annealing history of the samples. These initial bubbles were unexpected due to the location that they formed and their irregular geometry as they formed in the region of the sample with the lowest concentration of both helium and atomic damage and appeared to have a planar geometry with major axes aligned parallel to the specimen surfaces. It is proposed that a thermal vacancy assisted bubble formation and growth mechanism is likely responsible for these initially observed bubbles as this accounts for their location, geometry, and alignment, and a comparison with the temperature at bubble formation onset from other TEM investigations results in excellent agreement between the increase in thermal vacancy diffusivity. These planar-bubbles are observed to migrate and coalesce into bubbles with more regular (i.e., three-dimensional) geometries though they remain faceted. The work performed here cannot be used to conclusively determine the thermal-vacancy assisted bubble growth mechanism and further investigation should investigate the presence of any surface effects from the ion implantation and the possible diffusion of carbon introduced into the system during FIB sample preparation.

A simple comparison of the energy of formation of such planar-bubbles to spherical bubbles was derived and it was shown that under the conditions of this work, small planar bubbles could have a lower formation energy than spherical bubbles and

the appearance of these planar-bubbles is possibly a previously unreported stage in the formation of bubbles in TEM-thinned specimens. This derivation did not consider the unique anisotropic properties of zirconium.

A notable observation from the characterization of the as-implanted specimens was the presence of a multi-modal bubble size distribution in two of the samples that had aged at room temperature for approximately 9 months longer than the others prior to TEM preparation. This population of large diameter bubbles existed within the high density population of small bubbles but was not characterized in a manner that would confirm whether the small bubble population had decreased because of it's appearance or if the larger bubbles formed from helium within the zirconium matrix.

Data from observations of bubble growth and response at higher temperatures was lost due to equipment failure and, as such, the dominant helium bubble growth mechanism (migration & coalescence or Ostwald Ripening) in TEM-thinned zirconium specimens cannot be determined from this work. Section 5.5 discusses the observations made on this topic in more detail with the primary result that inert gas bubbles in zirconium appear to behave similarly to other metals with regard to time and temperature response.

The work described herein provides an improved understanding of the formation of helium bubbles in TEM-thinned zirconium metal and identifies several areas where further investigation could reveal useful information. From this work the following items are suggested as potential follow-up investigations:

- Investigation of the mean bubble size as a function of annealing time for varying helium concentrations could be used to confirm the dominant bubble growth mechanism active at different temperatures in zirconium.

- Identification of the threshold helium concentration required to form the high density region of small bubbles in in zirconium may provide useful information

to the nanoporous materials industry. The measurements made herein suggest an atomic concentration of approximately 10% or greater is required.

- Further confirmation of the impact of thermal vacancy population on the appearance and formation of bubbles in TEM-thinned specimens could be investigated by comparing metals with different helium mobility and vacancy diffusivity characteristics and evaluating the initial formation of bubbles.

- A TEM with electron energy loss spectroscopy capability could be used to measure the helium atom concentration in the planar-bubbles observed in this work. This information could be used to further develop the theoretical treatment of the bubble formation for comparison with an investigation into helium-vacancy complex formation and behavior to identify if the phenomenon is unique to zirconium, open hcp metals, or is merely a previously unobserved part of the bubble formation process in TEM-thinned metals.

- An investigation into the long term behavior of the high density region of small bubbles during room temperature aging and the formation of a multimodal bubble size distribution could provide information of relevance to the nanoporous materials fabrication industry as well as the commercial nuclear industry should it pursue certain advanced fuel and waste form storage concepts incorporating the metal.

REFERENCES

[1] A. R. Totemeier. *Evaluation of a Zirconium-Matrix Cermet for the Storage and Transmutation of Transuranic Isotopes.* Thesis, 2006.

[2] A.R. Totemeier and S.M. McDeavitt. Powder Metallurgical Fabrication of Zirconium Matrix Cermet Nuclear Fuels. *Journal of Materials Science*, 44(20):5494–5500, 2009.

[3] S.M. McDeavitt, A. Parkison, A.R. Totemeier, et al. Fabrication of Cermet Nuclear Fuels Designed for the Transmutation of Transuranic Isotopes. *Materials Science Forum*, 561-565:1733–1736, 2007.

[4] S.M. McDeavitt, A. Parkison, A.R. Totemeier, et al. Fabrication of Cermet Nuclear Fuels Designed for the Transmutation of Transuranic Isotopes. In *6th Pacific Rim International Conference on Advanced Materials and Processing (PRICM-6).*

[5] M. B. Chadwick, M. Herman, P. Obloinsk, et al. ENDF/B-VII.1 Nuclear Data for Science and Technology: Cross Sections, Covariances, Fission Product Yields and Decay Data. *Nuclear Data Sheets*, 112(12):2887–2996, 2011.

[6] D.O. Northwood. Irradiation Damage in Zirconium and its Alloys. *Atomic Energy Review*, 15(4):547–610, 1977.

[7] M. Griffiths. Evolution of microstructure in hcp metals during irradiation. *Journal of Nuclear Materials*, 205:225–241, 1993.

[8] G.J.C. Carpenter. Void Formation in Zirconium Under Irradiation in the High-Voltage Electron Microscope. *Radiation Effects*, 19:189–190, 1973.

[9] D. O. Northwood and R. W. Gilbert. Neutron radiation damage in zirconium and its alloys. *Radiation Effects*, 22(2):139–140, 1974.

[10] A. Rogerson. Irradiation growth in zirconium and its alloys. *Journal of Nuclear Materials*, 159:43–61, 1988.

[11] R. H. Zee, G. J. C. Carpenter, A. Rogerson, et al. Irradiation growth in deformed zirconium. *Journal of Nuclear Materials*, 150(3):319–330, 1987.

[12] G. J. C. Carpenter, R. H. Zee, and A. Rogerson. Irradiation growth of zirconium single crystals: A review. *Journal of Nuclear Materials*, 159:86–100, 1988.

[13] A. Rogerson and R. H. Zee. High fluence irradiation growth in single crystal zirconium at 553 K. *Journal of Nuclear Materials*, 151(1):81–83, 1987.

[14] R. W. Gilbert, K. Farrell, and C. E. Coleman. Damage structure in zirconium alloys neutron irradiated at 573 to 923 k. *Journal of Nuclear Materials*, 84(1-2):137–148, 1979.

[15] M. S. Anand, W. Mansel, G. Wallner, et al. Effect of alloying elements on recovery and damage rates in zirconium. *Journal of Nuclear Materials*, 126(2):144–151, 1984.

[16] S. N. Buckley and S. A. Manthorpe. Dislocation loop nucleation and growth in zirconium-2.5 wtalloy during 1 MeV electron irradiation. *Journal of Nuclear Materials*, 90(1-3):169–174, 1980.

[17] S. N. Buckley, R. Bullough, and M. R. Hayns. The direct observation of irradiation damage in zirconium and its alloys. *Journal of Nuclear Materials*, 89(2-3):283–295, 1980.

[18] H. Ullmaier. Helium in Metals. *Radiation Effects*, 78:1–10, 1983.

[19] N. Marochov and P. J. Goodhew. A comparison of the growth of helium and neon bubbles in nickel. *Journal of Nuclear Materials*, 158(0):81–86, 1988.

[20] B. N. Singh and H. Trinkaus. *Parameters and Processes Controlling Helium Bubble Formation in Metals at Elevated Temperatures.* Plenum Press, New York, 1991.

[21] B. N. Singh and H. Trinkaus. An analysis of the bubble formation behaviour under different experimental conditions. *Journal of Nuclear Materials*, 186(2):153–165, 1992.

[22] R.V. Nandedkar. The Behaviour of Helium in Metals. *Transactions of the Indian Institute of Metals*, 38(1):64–75, 1985.

[23] C. Templier. *Inert Gas Bubbles in Metals: A Review.* Plenum Press, New York, 1991.

[24] G.J. Thomas. Experimental Studies of Helium in Metals. *Radiation Effects*, 78:37–51, 1983.

[25] J. H. Evans. Void and bubble lattice formation in molybdenum: A mechanism based on two-dimensional self-interstitial diffusion. *Journal of Nuclear Materials*, 119(23):180–188, 1983.

[26] J.H. Evans, A. Van Veen, and L.M. Caspers. The application of TEM to the study of helium cluster nucleation and growth in molybdenum at 300 K. *Radiation Effects*, 78:105–120, 1983.

[27] D.J. Mazey, B.L. Eyre, and J.H. Evans. A Transmission Eleectron Microscopy Study of Molybdenum Irradiated with Helium Ions. *Journal of Nuclear Materials*, 64:145–156, 1977.

[28] H. Trinkaus and B.N. Singh. Helium Accumulation in Metals During Irradiation - Where Do We Stand? *Journal of Nuclear Materials*, 323:229–242, 2003.

[29] M. B. Lewis and K. Farrell. Migration behavior of helium under displacive irradiation in stainless steel, nickel, iron and zirconium. *Nuclear Instruments and Methods in Physics Research Section B: Beam Interactions with Materials and Atoms*, 16(2-3):163–170, 1986.

[30] W. D. Wilson. Theory of Small Clusters of Helium in Metals. *Radiation Effects*, 78:11–24, 1983.

[31] J.Th.M. De Hosson, L. Caspers, and A. Van Veen. Atomistic Studies of Helium Trapping in Metals. *Radiation Effects*, 78:25–36, 1983.

[32] B. B. Glasgow and W. G. Wolfer. Comparison of mechanisms for cavity growth by athermal and thermal processes. *Journal of Nuclear Materials*, 122(1-3):503–508, 1984.

[33] W. G. Wolfer. Advances in void swelling and helium bubble physics. *Journal of Nuclear Materials*, 122(1-3):367–378, 1984.

[34] A. van Veen. *Helium Defect Interactions in Metals and Silicon*, pages 41–57. Plenum Press, New York, 1991.

[35] H. Trinkaus. Energetics and Formation Kinetics of Helium Bubbles in Metals. *Radiation Effects*, 78:189–211, 1983.

[36] J.H. Evans and D.J. Mazey. Evidence for solid krypton bubbles in copper, nickel, and gold at 293K. *Journal of Physics F: Metal Physics*, 15(1):L1–L6, 1985.

[37] J. H. Evans and D. J. Mazey. Solid bubble formation in titanium injected with krypton ions. *Journal of Nuclear Materials*, 138(23):176–184, 1986.

[38] R.S. Barnes and D.J. Mazey. The Migration and Coalescence of Inert Gas Bubbles in Metals. *Proceedings of the Royal Society of London A*, 275:47–57, 1963.

[39] M.E. Gulden. Migration of gas bubbles in irradiated uranium dioxide. *Journal of Nuclear Materials*, 23(1):30–36, 1967.

[40] P. J. Goodhew and S. K. Tyler. Helium bubble behaviour in b.c.c. metals below $0.65\,T_m$. *Proceedings of the Royal Society of London A*, 377:151–184, 1981.

[41] D. Kaletta. The growth of gas bubbles in solids under irradiation at elevated temperatures around 0.5 T_m. *Radiation Effects*, 78:245–259, 1983.

[42] Dale E. Alexander and R. C. Birtcher. The effect of ion irradiation on inert gas bubble mobility. *Journal of Nuclear Materials*, 191194, Part B(0):1289–1294, 1992.

[43] F. A. Nichols. Kinetics of Diffusional Motion of Pores in Solids. *Journal of Nuclear Materials*, 30:143–165, 1969.

[44] P.W. Voorhees. The Theory of Ostwald Ripening. *Journal of Statistical Physics*, 38(1/2):231–252, 1985.

[45] G. W. Greenwood, A. J. E. Foreman, and D. E. Rimmer. The role of vacancies and dislocations in the nucleation and growth of gas bubbles in irradiated fissile material. *Journal of Nuclear Materials*, 1(4):305–324, 1959.

[46] J.H. Evans, A. Van Veen, and L.M. Caspers. Direct Evidence for helium bubble growth in molybdenum by the mechanism of loop punching. *Scripta Metallurgica*, 15:323–326, 1981.

[47] H. Van Swygenhoven and L.M. Stals. The Greenwood-Forman-Rimmer Loop Punching Mechanism as Applied to helium Bubble Growth in Nickel Implanted with 5 keV He^+ Ions at 273 K. *Radiation Effects*, 78:157–163, 1983.

[48] H. Trinkaus and W. G. Wolfer. Conditions for dislocation loop punching by helium bubbles. *Journal of Nuclear Materials*, 122(1-3):552–557, 1984.

[49] H. Trinkaus. *Possible Mechanisms Limiting the Pressure in Inert Gas Bubbles in Metals*. Plenum Press, New York, 1991.

[50] S.E. Donnelly, D.R.G. Mitchell, and A. Van Veen. *Loop-Punching as a Mechanism for Inert Gas Bubble Growth in Ion-Implanted Metals*. Plenum Press, New York, 1991.

[51] Herbert Schroeder and Paulo F. P. Fichtner. On the coarsening mechanisms of helium bubbles Ostwald ripening versus migration and coalescence. *Journal of Nuclear Materials*, 179181, Part 2(0):1007–1010, 1991.

[52] J.H. Evans and A. van Veen. A description of bubble growth and gas release during thermal annealing of helium implanted copper. *Journal of Nuclear Materials*, 217:276–280, 2004.

[53] J.H. Evans and A. van Veen. Breakaway bubble growth during the annealing of helium bubbles in metals. *Journal of Nuclear Materials*, 334:40–46, 2004.

[54] I. R. Brearley and D. A. MacInnes. An improved equation of state for inert gases at high pressures. *Journal of Nuclear Materials*, 95(3):239–252, 1980.

[55] C. Ronchi. Extrapolated Equation of State for Rare Gases at High Temperatures and Densities. *Journal of Nuclear Materials*, 96:314–328, 1981.

[56] W.G. Wolfer, B.B. Glasgow, M.F. Wehner, et al. Helium Equation of State for Small Cavities: Recent Developments. *Journal of Nuclear Materials*, 122:565–570, 1984.

[57] Benny Glam, Shalom Eliezer, Daniel Moreno, et al. Helium bubbles formation in aluminum: Bulk diffusion and near-surface diffusion using TEM observations. *Journal of Nuclear Materials*, 392(3):413–419, 2009.

[58] P. B. Johnson and D. J. Mazey. Gas-bubble superlattice formation in bcc metals. *Journal of Nuclear Materials*, 218(3):273–288, 1995.

[59] F. E. Lawson and P. B. Johnson. A temperature threshold for gas-bubble superlattice formation in molybdenum. *Journal of Nuclear Materials*, 252(12):34–42, 1998.

[60] P. B. Johnson and D. J. Mazey. A helium gas-bubble superlattice in vanadium with bubble concentrations unprecedented for metals. *Journal of Nuclear Materials*, 170(3):290–293, 1990.

[61] P.B. Johnson. Bubble Structures in He^+ Irradiated Metals. *Radiation Effects*, 78:147–156, 1983.

[62] P. B. Johnson and D. J. Mazey. The gas-bubble superlattice and the development of surface structure in He+ and H irradiated metals at 300 K. *Journal of Nuclear Materials*, 93-94(Part 2):721–727, 1980.

[63] D. J. Mazey and J. H. Evans. Bubble lattice formation in titanium injected with krypton ions. *Journal of Nuclear Materials*, 138(1):16–18, 1986.

[64] R. C. Birtcher and A. S. Liu. Temperature dependence of Kr precipitation in Ni. *Journal of Nuclear Materials*, 165(2):101–109, 1989.

[65] J. H. Evans. A computer simulation of the two-dimensional SIA diffusion model for void lattice formation. *Journal of Nuclear Materials*, 132(2):147–155, 1985.

[66] J. H. Evans, A. J. E. Foreman, and R. J. McElroy. Anisotropic diffusion of self-interstitials in zirconium. *Journal of Nuclear Materials*, 168(3):340–342, 1989.

[67] A. Wolfenden and K. Farrell. On The question of void formation in neutron irradiated zirconium. *Scripta Metallurgica*, 6:127–130, 1972.

[68] D. Faulkner and C.H. Woo. Void Swelling in Zirconium. *Journal of Nuclear Materials*, 90:307–316, 1980.

[69] L. Pagano, A.T. Motta, and R.C. Birtcher. Bubble Formation in Zr Alloys Under Heavy ion implantation. In *Proceedings of the Materials Research Society Symposium*, pages 201–206.

[70] L. Pagano, A. T. Motta, and R. C. Birtcher. The formation of bubbles in Zr alloys under Kr ion irradiation. *Journal of Nuclear Materials*, 244(3):295–304, 1997.

[71] James F. Ziegler, M. D. Ziegler, and J. P. Biersack. SRIM - The stopping and range of ions in matter (2010). *Nuclear Instruments and Methods in Physics Research Section B: Beam Interactions with Materials and Atoms*, 268(11-12):1818–1823, 2010.

[72] M. R. Rühle. *Transmission Electron Microscopy of Radiation-Induced Defects*, volume 26. U.S. Atomic Energy Comission, 1971.

[73] G.P. Tiwari and J. Singh. Effect of the Proximity of the External Surface on the Growth Characteristics of Inert Gas Bubbles. *Journal of Nuclear Materials*, 185:224–230, 1991.

[74] V. N. Chernikov, H. Trinkaus, P. Jung, et al. The formation of helium bubbles near the surface and in the bulk in nickel during post-implantation annealing. *Journal of Nuclear Materials*, 170(1):31–38, 1990.

[75] N. Marochov, L. J. Perryman, and P. J. Goodhew. Growth of inert gas bubbles after implantation. *Journal of Nuclear Materials*, 149(3):296–301, 1987.

[76] J. H. Evans. Inert gas release from metals and UO2 during high temperature annealing: the role of thermal vacancies. *Journal of Nuclear Materials*, 225(0):302–307, 1995.

[77] J. H. Evans and A. van Veen. Gas release processes for high concentrations of helium bubbles in metals. *Journal of Nuclear Materials*, 233237, Part 2(0):1179–1183, 1996.

[78] G. P. Tiwari. Behaviour of inert gas bubbles under chemical concentration gradients. *Journal of Nuclear Materials*, 232(23):119–124, 1996.

[79] J. H. Evans and A. van Veen. Comments on Behaviour of inert gas bubbles under chemical concentration gradients by G.P. Tiwari. *Journal of Nuclear Materials*, 252(12):156–161, 1998.

[80] G. P. Tiwari. Reply to Comments on Behaviour of inert gas bubbles under chemical concentration gradients. *Journal of Nuclear Materials*, 252(12):162–167, 1998.

[81] M. B. Lewis. The importance of oxygen to helium-defect trapping in zirconium. *Journal of Nuclear Materials*, 148(2):175–184, 1987.

[82] G.J.C. Carpenter, J.A. Jackman, J.P. McCaffrey, et al. *In Situ* Hydride Formation in Zirconium and Titanium during Ion Milling. *Journal of the Microscopy Society of America*, 1(4):175–184, 1995.

[83] G.H. Kinchin and R.S. Pease. The Displacement of Atoms in Solids by Radiation. *Reports on Progress in Physics*, 18, 1955.

[84] D. J. Bacon, A. F. Calder, F. Gao, et al. Computer simulation of defect production by displacement cascades in metals. *Nuclear Instruments and Methods in Physics Research Section B: Beam Interactions with Materials and Atoms*, 102(1-4):37–46, 1995.

[85] Dale E. Newbury and Robert L. Myklebust. Simulation of electron-excited X-ray spectra with NISTNIH Desktop Spectrum Analyzer (DTSA). *Surface and Interface Analysis*, 37(11):1045–1053, 2005.

[86] I. Piñera, C.M. Cruz, Y. Abreu, et al. Monte Carlo Assisted Classical Method for the Calculation of *dpa* Distributions in Solid Materials, 2008.

[87] S.J. Wooding, L.M. Howe, F. Gao, et al. A molecular dynamics study of high-energy displacements cascades in α-zirconium. *Journal of Nuclear Materials*, 254:191–204, 1998.

[88] ASTM International. Standard Practice for Neutron Radiation Damage Simulation by Charged-Particle Irradiation, 2009.

[89] Jannik C. Meyer, Franz Eder, Simon kurasch, et al. Accurate Measurement of Electron Beam Induced Displacement Cross Sections for Single Layer Graphene. *Physical Review Letters*, 108(196102):1–6, 2012.

[90] J. Schindelin, I. Arganda-Carreras, and E. et al. Frise. Fiji: an open-source platform for biological image analysis. *Nature methods*, 9(7):676–682, 2012.

[91] Chubin Wan, Xiaosong Zhou, Yuting Wang, et al. Structural investigations in helium charged titanium films using grazing incidence XRD and EXAFS spectroscopy. *Journal of Nuclear Materials*, 444(13):142–146, 2014.

[92] F. Christien and A. Barbu. Effect of self-interstitial diffusion anisotropy in electron-irradiated zirconium: A cluster dynamics modeling. *Journal of Nuclear Materials*, 346(23):272–281, 2005.

[93] Warren Desorbo and David Turnbull. Kinetics of vacancy motion in high-purity aluminum. *Physical Review*, 115(3):560–563, 1959.

[94] Guangai Sun, Erdong Wu, Chaoqiang Huang, et al. Evolution and change of He bubbles in He-containing Ti films upon thermal treatment studied by small-angle X-ray scattering and transmission electron microscopy. *Thin Solid Films*, 558(0):125–133, 2014.

[95] Xin Zheng. Simulation of bimodal size distributions for coarsening. *Zeitschrift fr Physik B Condensed Matter*, 93(4):501–507, 1994.